

## GNGTS 2024

# APPLIED GEOPHYSICS FOR ENERGY, ENVIRONMENT AND NEW TECHNOLOGIES

## Session 3.3

### Theoretical and methodological development in geophysics

Convenors of the session:

*Andrea Tognarelli* – [andrea.tognarelli@unipi.it](mailto:andrea.tognarelli@unipi.it)

*Luca Masnaghetti* – [LMasnaghetti@slb.com](mailto:LMasnaghetti@slb.com)

*Gianluca Gola* – [gianluca.gola@igg.cnr.it](mailto:gianluca.gola@igg.cnr.it)

Contributions recommended for this session:

- Theoretical Developments in Applied Geophysics
- New Technologies and Methods
- Geophysical Data Modelling and Inversion
- Novel Geophysical Acquisition and Processing Techniques
- Non Standard Applications in Geophysics
- Geophysical Data Integration and Interpretation
- Development and Application of Machine Learning Techniques and Data Analytics for Geophysical Data
- Geophysics for Sustainable Energy Development

The session is focused on the theoretical and methodological development in geophysics. Novel approaches and new techniques related to digital data (seismic, electromagnetic, potential field) processing as well as the results of their application to specific case studies fit this session. Contributions that present innovative acquisition procedures (remote, superficial and in-situ), treatment, inversion and integration of geophysical data and multiphysics numerical modeling are accepted in this session. The session promotes multidisciplinary and encourages the dissemination, comparison and technological transfer of innovative methods and technologies in the entire geophysical community.

# Wavelet transform spectral analysis to estimate the depth of gravity and magnetic sources

**M.A. Abbas<sup>1,2</sup>, M. Milano<sup>1</sup>, D.F. Barbolla<sup>3</sup>, M. Fedi<sup>1</sup>**

*<sup>1</sup> University of Naples Federico II, Naples, Italy*

*<sup>2</sup> South Valley University, Qena, Egypt*

*<sup>3</sup> Institute of heritage Science - National Research Council, Lecce, Italy*

Spectral analysis, which is based on the Fourier Transform, allows high-resolution analysis in the frequency domain but not in the space domain. Due to this lack of spatial resolution, well-known approaches such as Spector and Grant's method cannot provide information on the source positions. We propose to address these concerns by employing a scalogram analysis, which is achieved by study potential fields throughout the continuous wavelet transform. It allows detection and location of source contributions in the scalogram, with good resolution at both spatial and wavenumber level. As a new tool, we study here the depths to the top and bottom of the potential field sources locally on the 3D scalogram, along delimited sub-volumes, subareas, and scale-profiles. When such local spectral analysis is applied to synthetic data, the results are in good agreement with the information of the causative sources. We also apply the method to real aeromagnetic data of the Monte Vulture, Southern Italy.

Corresponding author: [mahmoud.abbas@unina.it](mailto:mahmoud.abbas@unina.it)

# PROBABILISTIC APPROACH TO FULL-WAVEFORM INVERSION OF SURFACE WAVES: A REAL DATA APPLICATION

S. Berti<sup>1,2</sup>, M. Aleardi<sup>1</sup>, E. Stucchi<sup>1</sup>

<sup>1</sup> *Department of Earth Sciences (University of Pisa, Italy)*

<sup>2</sup> *Department of Earth Sciences (University of Florence, Italy)*

## Introduction

Surface waves play a crucial role in near-surface geophysics, offering a non-invasive way to determine the elastic properties of near-surface sediments: this turns out to be of fundamental importance, for example, for geotechnical site characterization. This analysis started with the spectral analysis of surface waves (SASW) and became increasingly popular after the introduction of the multichannel analysis of surface waves (MASW). The main limitation of these approaches is the reliance on a 1D layered model assumption, making them less effective in the presence of substantial lateral heterogeneity or when dealing with multimodal dispersion patterns in the context of low-velocity layers and strong velocity contrasts.

The advent of increased computational power in recent decades has made it possible the application of the full-waveform inversion (FWI) approach, which exploits the full information content of the recorded seismogram to infer high-resolution estimations of subsurface acoustic or elastic parameters. While acoustic FWI is commonly employed for imaging complex subsurface structures, it falls short in near-surface seismic studies due to the prevalence of surface waves. In this work, our focus shifts to multiparameter elastic FWI, aiming to construct P-wave and S-wave velocity models for near surface sediments. The inclusion of surface waves in the wavefields increases the nonlinearity of FWI, elevating the risk of the local approach getting stuck in some local minima of the usual L2 norm error function. In this context, the inversion outcomes become strongly dependent on the starting model. Although global optimization methods can mitigate this issue, they come at the cost of significantly increased computational demands (Lamuraglia et al. 2022).

Trying to overcome these issues, we propose a Bayesian inference framework for elastic FWI. Differently from the local approach, the proposed method provides a comprehensive evaluation of the uncertainty affecting the retrieved solution through the so-called posterior probability density function (PPD) in the model space. Based on the Bayes theorem, the PPD incorporates the information coming from both the prior knowledge on the model parameters and the recorded seismic data but, in case of nonlinear forward modelling, a sampling technique needs to be adopted to approximate this density function. In our case a Markov Chain Monte Carlo (MCMC) sampling strategy is used to numerically evaluate the statistical properties of the PPD. However, challenges arise in the form of the convergence rate dependency on the proposal distribution and the diminished sampling ability in high dimensional spaces, known as the curse of dimensionality. To tackle these issues, we introduce a gradient-based Markov Chain Monte Carlo (GB-MCMC) method where the proposal distribution is constructed by the local gradient and the Hessian of the negative log posterior, and we also reduce the dimensionality of the problems making use of the

Discrete Cosine Transform (DCT) reparameterization. This approach is applied to a real dataset, acquired in the framework of the InterPACIFIC project at the test site of Grenoble (France, Garofalo et al. 2016).

### Method

The method we employed is the same described in Berti et al. (2023) and applied to solve the acoustic FWI, but in the present study the method has been extended to the elastic case and validated on real data. For the sake of brevity, the theoretical description of the method is not included here, and we refer the reader to Berti et al. (2023) for more details. In essence, our implemented MCMC method defines the proposal distribution as a localized approximation of the PPD by leveraging information derived from the local gradient and Hessian of the negative log posterior computed around the current state of the chain. This significantly reduces the time requested by the algorithm to reach the steady state. The drawback of this procedure is that derivatives need to be evaluated for each sampled model, posing computational challenges when dealing with extensive model and data spaces. Therefore, a convenient strategy to reduce the computational complexity of this inverse problem is to compress the model and data spaces through appropriate reparameterization techniques, such as the DCT. The DCT of a signal reveals the energy distribution of the signal in the frequency domain spectrum. Typically, the majority of the signal's energy is expressed by low-order DCT coefficients and consequently, this mathematical transformation serves as a tool for model and data compression, achieved by setting the coefficients of the base function terms beyond a certain threshold equal to zero. The estimation of the optimal number of DCT coefficients needed to approximate the model and data spaces is a critical step of our inversion framework. For the seismic data, we have analyzed how the relative percentage error, calculated as the ratio between the L2 norm difference of the observed and compressed data and the L2 norm of the observed data, varies using different combinations of DCT coefficients; for the model space instead, we have used the available borehole data, investigating how the variability of the model, calculated as the ratio between the variance of the compressed and uncompressed models (Aleardi, 2021), changes with the number of retained DCT coefficients.

### Results

To validate our proposed methodology, we applied the approach to a field dataset, acquired in Grenoble, France, as part of the InterPACIFIC project. Three in-line boreholes, spaced at 4.5m intervals, were drilled up to 50m depth. These available well-log data were used to validate the results obtained in our work. The dataset consists of three shot gathers, of which one is split-spread and two are off-ends, recorded by 48 vertical geophones with a spacing of 1 m and a natural frequency of 4.5 Hz. Pre-processing steps, including trace-by-trace amplitude normalization and a zero-phase band-pass filter (3-30Hz), were applied to enhance data quality. Then, a 3D to 2D correction is needed to compensate for the geometrical spreading between the real case point source and the 2D forward modelling where line sources are implicitly used in the simulations. For generating our predicted data, we have constructed a grid with a size of  $276(n_{x_0}) \times 150(n_{z_0})$ , where  $n_{x_0}$  and  $n_{z_0}$  are the number of grid points in the horizontal and vertical direction. The grid spacing is set to 0.25m in both directions, to avoid numerical dispersion in the finite difference modelling. The time sampling is 0.1ms for the forward modelling and the registration time is 0.5s. Both predicted and observed data were resampled to a 2ms time interval. The simulation of the shots is performed using SOFI2D (Bohlen, 2002), a viscoelastic forward modelling code that solves the pure elastic or viscoelastic wave equation by a finite difference scheme in the time domain. The model parameters to be estimated are the  $V_s$  and  $V_p$  values, and we are considering a homogeneous

constant model for the density. However, for brevity, only the  $V_s$  results will be discussed because this is notoriously the most informed model parameters when considering surface wave data. Parallelization of the calculation of the Jacobian matrix across different servers was employed to reduce computational costs.

The seismic data and velocity models must be projected onto the DCT space, where the MCMC sampling runs. For the data, we have noticed that  $60 \times 45 = 2700$  retained coefficients resulted in a relative percentage error with respect to the observed data lower than 8%, reducing the the full  $250 \times 48 \times 3 = 36000$ -D data space to a  $60 \times 45 \times 3 = 8100$ -D domain (where are considering the same number of DCT coefficients for all the three shots). For the model space instead, 20 and 7 coefficients along the two DCT spatial dimensions explain more than 95% of variability of the model obtained extending the borehole data in the horizontal direction, reducing the  $150 \times 276 \times 2 = 82800$ -D elastic space to an  $20 \times 7 \times 2 = 280$ -D domain (i.e., we are considering the same number of DCT coefficients for both the  $V_p$  and  $V_s$  models). We need to point out that this compression not only reduces the dimensions of the vectors and matrices involved in the inversion procedure (such as the gradient and the Hessian), but also greatly reduces the number of forward evaluations needed to construct the Jacobian matrix and so, the overall computational cost of the algorithm.

The implementation used six cores on an Intel® Core™ i7-8700 CPU @ 3.20GHz. Each iteration, including computing the Jacobian, the gradient, the Hessian matrix and drawing a sample, takes approximately 8m wall clock time. A total of 4.000 iterations for a single chain required approximately 6 days. In our case we used five MCMC chains to sample the model space, which started from very simple two layered velocity models. Figures 1a and 1c show, respectively, one of the starting models of the chains used for the GB-MCMC inversion and the posterior mean model, computed considering all the chains. The prior information for the Bayesian inversion (prior mean vector and prior covariance matrix) are directly derived from the two layered model displayed in Figure 1a.

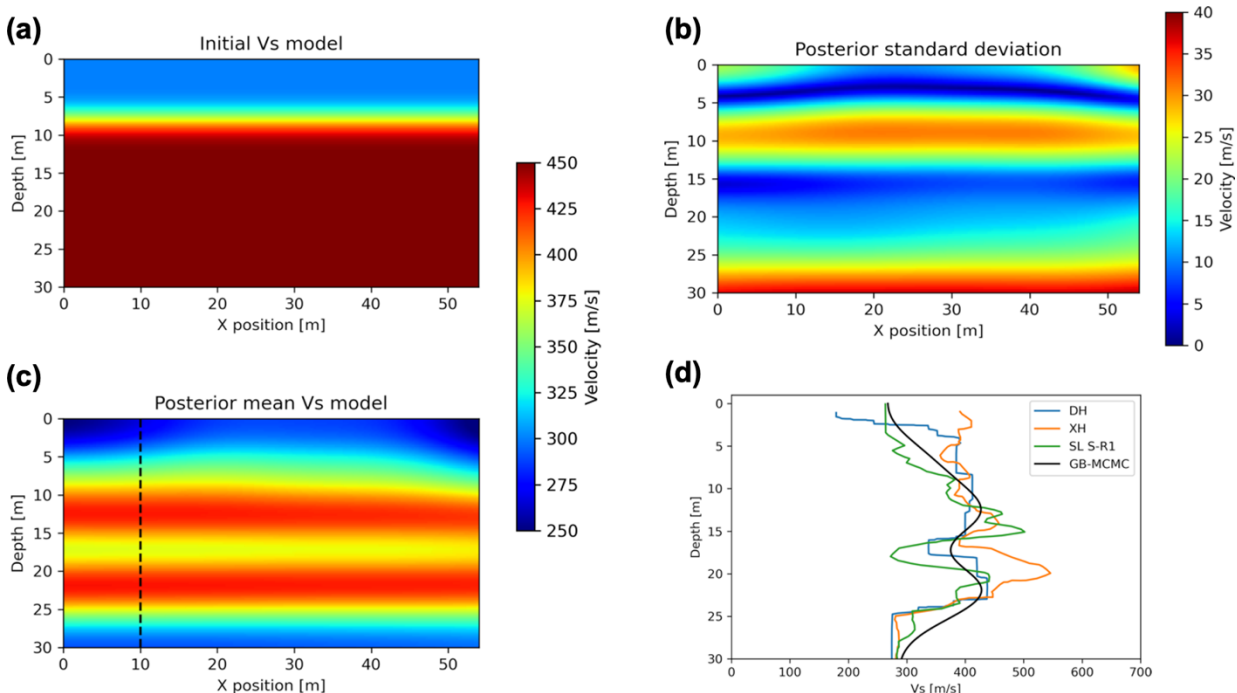


**Fig. 1** (a) One of the starting models used for the GB-MCMC inversion; (b) Posterior standard deviation map; (c) Posterior mean  $V_s$  model considering the five chains; the dashed black line corresponds to the position of the available borehole data; (d) The borehole data together with the velocity profile of the predicted model at the horizontal position of 10m (black).

A comparison between the obtained results at the horizontal position of 10m and the available borehole data revealed an accurate reproduction of all the main velocity variations (Figure 1d). In particular, the two high velocity layers are clearly identified at depths 10-15m and 19-25 m with a  $V_s$  value around 430 m/s. In between, there is a very thin layer (around 3m of thickness) characterized by a lower  $V_s$  velocity, around 370 m/s. We are also able to observe the velocity inversion around 25m of depth, at the bottom edge of the model. As expected, this velocity layer is also characterized by the highest standard deviation values (Figure 1b), considering that it is below the high velocity layer and at the edge of the model. We need to consider that the standard deviation map suggests small uncertainties for all the velocity models (less than 40 m/s).

In Figure 2a we can see the evolution of the negative log-likelihood for all the chains, and we can notice that, after the end of the burn-in period, all the chains oscillate around the same values, meaning that we have reached the stationary regime. Figure 2b shows the acceptance ratio for the five chains, calculated as the ratio between the number of accepted models and the number of iterations. We can see that all the values are very high, compared to the ones usually achieved with standard gradient-free MCMC methods (around 20%), highlighting the superior efficiency of the proposed method. A comparison between the leftmost shot of the observed data (after pre-processing) and the data computed on the starting model of Figure 1a revealed significant cycle-skipping, indicating that any local approach would fail in locating the global minimum of the error function (Figure 3a). Differently, our approach finally provides a mean posterior model that is capable of successfully reproducing the observed seismic data (Figure 3b). This capability was emphasized by the close-ups of Figures 3c and 3d, in which we can appreciate the significant differences between the observed and initial data and how the cycle skips vanish when the data computed on the posterior mean model is considered. This means that the implemented approach could be also used to define an optimal starting model suitable for a subsequent step of local FWI.

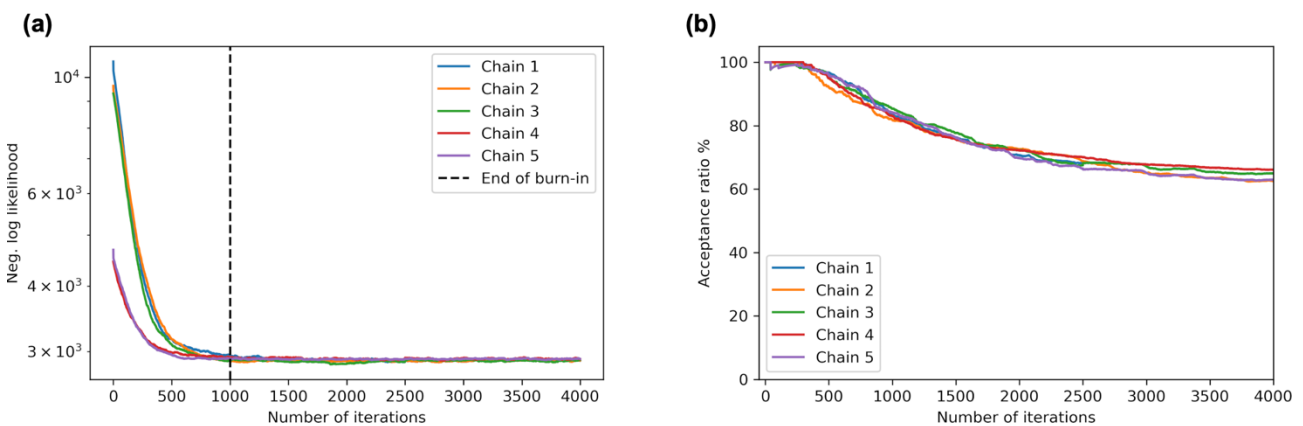


**Fig. 2** (a) Evolution of the negative log-likelihood, which measures the misfit between observed and predicted data, for all the five chains and the end of the burn-in period (dashed black); (b) Acceptance ratio for all the five chains.

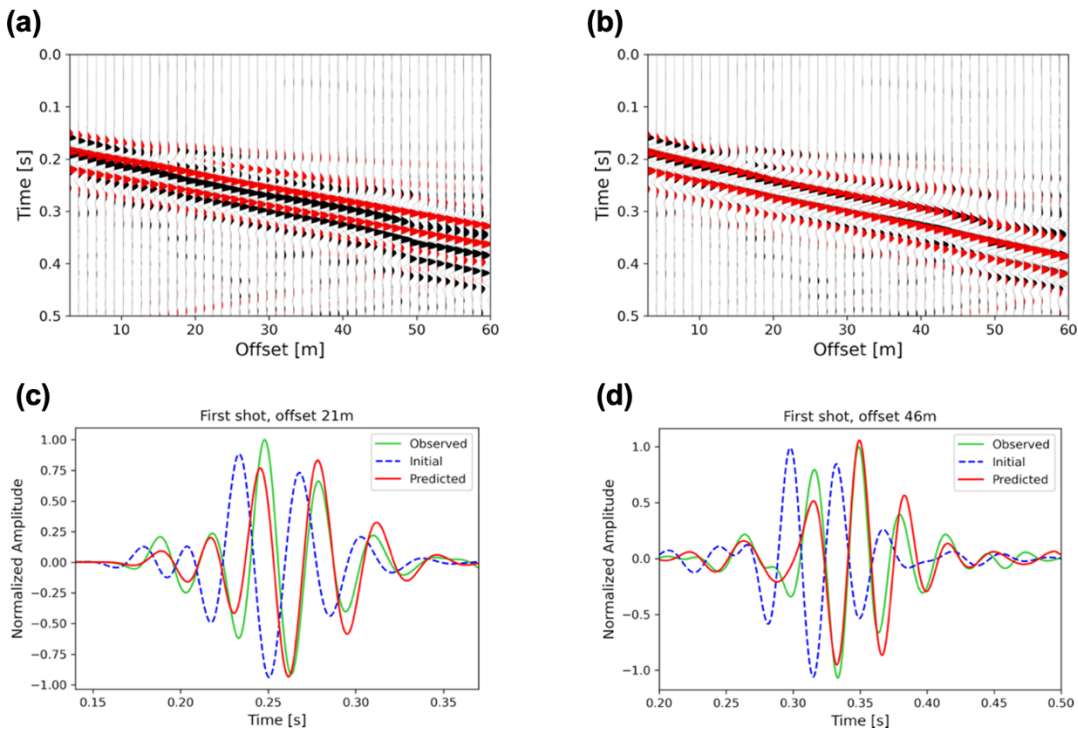


**Fig. 3** (a) The leftmost shot of the observed data in black, compared against the data generated using one of the starting models (red); (b) Comparison between the same observed shot gathers (in black) and the data generated from the posterior mean model (in red); (c, d) Comparison of two seismic traces of the same shot of the observed data (green), the predicted data (red) and the initial data (dashed blue).

## Conclusions

In this study we introduced a computationally efficient Bayesian elastic FWI, leveraging a GB-MCMC sampling technique along with a DCT compression applied to both the model and data spaces. The adopted MCMC strategy addresses the cycle-skipping problem affecting the local FWI approach, utilizing the local gradient and Hessian information of the posterior density to guide the sampling towards the most promising regions of the model space. This results in a significant reduction in computational burden of the probabilistic approach compared with standard gradient-free MCMC algorithms. We demonstrated the efficacy of the GB-MCMC elastic FWI applied to a field dataset, acquired in Grenoble. After pre-processing the seismic data in order to make it comparable with the data generated using the elastic forward modelling, five Markov chains were employed to numerically assess the PPD, each one starting from very simple initial models. The predicted posterior mean model accurately replicated all the vertical velocity variations evidenced by the available borehole data. In addition, our model prediction is also capable to closely match the observed seismic data, affirming the applicability and reliability of the proposed approach that can also be conveniently used to define a starting point for a subsequent step of local inversion, aimed at enhancing the velocity model's resolution and further minimize the difference between predicted and observed data. Our ongoing research focuses on optimizing the overall computational efficiency of our inversion procedure through the integration of deep learning techniques.

## References

Aleardi, M.; 2021: A gradient-based Markov chain Monte Carlo algorithm for elastic pre-stack inversion with data and model space reduction. *Geophysical Prospecting*, 69(3).

Berti, S., Aleardi, M. and Stucchi, E.; 2023. A computationally efficient Bayesian approach to full-waveform inversion. *Geophysical Prospecting*, 1-24.

Bohlen, T.; 2002. Parallel 3D viscoelastic finite difference seismic modelling. *Computers and Geosciences*, 28, 887-899.

Garofalo, F., Foti, S., Hollender, F., Bard, P.Y., Cornou, C., Cox, B. et al.; 2016. InterPACIFIC project: comparison of invasive and non-invasive methods for seismic site characterization. Part I: Intra-comparison of surface wave methods. *Soil Dynamics and Earthquake Engineering*, 82, 222-240.

Lamuraglia, S., Stucchi, E. and Aleardi, M.; 2022. Application of a global-local full-waveform inversion of Rayleigh wave to estimate the near-surface shear wave velocity model. *Near Surface Geophysics*, 1-18.

Corresponding author: Sean Berti, [sean.berti@unifi.it](mailto:sean.berti@unifi.it)

# Full-decay spectral modelling of time-domain induced polarization decoupling model and forward meshes with EEMverter

A.Bollino<sup>1</sup>, G. Fiandaca<sup>1</sup>

<sup>1</sup> *The EEM Team for Hydro & eXploration, Department of Earth Sciences "Ardito Desio", Università degli Studi di Milano, Milano (Italy)*

Direct current (DC) resistivity and induced polarization (IP) geophysical methods are widely used in geophysical near-surface investigations, gaining information about subsurface conductivity structures by injecting electric currents into the ground and measuring electric voltages at different locations. The DC resistivity method provides information about the electrical conductive properties of the subsurface. In contrast, the IP method targets the capacitive characteristics offering additional insight into the physical and electrochemical nature of subsurface materials. The IP phenomenon has been widely investigated both in time (TDIP) and frequency (FDIP) domains, in the laboratory, or through field studies. The TDIP has been used for many years for disseminated ores and mineral discrimination (e.g. Vanhala and Peltoniemi, 1992; Seigel et al., 1997, 2007). Over the last 20 years significant advancements in IP research have taken place, particularly with respect to the spectral content of the IP signal, which can be applied to engineering and environmental problems, such as the detection of contaminants and old landfills (e.g. Weller et al. 1999; Gazoty et al. 2012; Fiandaca et al., 2015; Johansson et al. 2015), and the derivation of grain size distribution parameters in unconsolidated sediments (e.g. Vanhala et al., 1992, Kemna et al., 2004, 2012).

In the frequency domain, IP phenomena can be represented as a complex conductivity  $\sigma^*(\omega)$  that varies with frequency ( $\omega$ ), which can be expressed as:

$$\sigma^*(\omega) = |\sigma(\omega)| e^{i\varphi(\omega)} = \sigma'(\omega) + i\sigma''(\omega) \quad (1)$$

where  $*$  denotes a complex term,  $|\sigma(\omega)|$  is the magnitude of conductivity,  $\varphi$  is the phase angle between injected current and measured voltage,  $\sigma'(\omega)$  is the real component of conductivity,  $\sigma''(\omega)$  is the imaginary component of conductivity,  $\omega = 2\pi f$  is the angular frequency representation of frequency  $f$ , and  $i = \sqrt{-1}$  (Binley, 2015). By neglecting electromagnetic (EM) effects, the complex potential  $u^*(\omega) = u'(\omega) + iu''(\omega)$  is linked to the complex conductivity through Poisson's equation:

$$\nabla \cdot j_S^*(\omega, r) = \nabla \cdot [\sigma^*(\omega, r)E^*(\omega, r)] \quad (2)$$

where  $j_s^*$  is the applied source current density,  $\mathbf{r} = (x, y, z)$  is the spatial location, and  $E^*(\omega, \mathbf{r}) = -\nabla u^*(\omega, \mathbf{r})$  is the complex electric field.

In the time domain, Poisson's equation is given as a convolution between the conductivity and the electric field as a function of the time  $t$  (e.g. Kemna, 2000):

$$\nabla \cdot j_s(t, \mathbf{r}) = \nabla \cdot \left[ \int_0^{\infty} \sigma(t', \mathbf{r}) E(t - t', \mathbf{r}) dt' \right] \quad (3)$$

where  $\sigma(t)$  is the inverse Laplace transform of  $\sigma^*(\omega)$  and  $E(t, \mathbf{r}) = -\nabla u(t, \mathbf{r})$ .

As mentioned above, during the last two decades, significant advancements in induced polarization research have taken place, particularly with respect to spectral IP (SIP) and its increasing application in near-surface investigations even if surveys are usually modelled by taking into account only the integral chargeability, thus disregarding spectral content and neglecting the effect of the transmitted waveform, biasing inversion results. In this context, following Fiandaca et al. (2012, 2013)'s approach, EEMverter has been developed to model IP in electric and electromagnetic (EM) data within the same inversion framework and where the forward response is computed in the frequency domain for all dimensionalities, solving the full version of Poisson's equation, and then transformed into the time domain, thus avoiding the time-domain approximation (eq. 3). Here, we will focus only on the galvanic aspects in EEMverter modelling, while the other modelling features of EEMverter, such as EM modelling, time-lapse and joint inversion of galvanic and EM data are treated in Fiandaca et al. (2024).

From a physical-mathematical point of view, resistivity and IP forward responses are modelled in the frequency domain for a range of frequencies using the finite element method. The responses are then transformed into the time domain for each quadrupole measurement and the transmitted current waveform is applied. In 2-D, the FD forward response assumes an isotropic 2-D distribution of the complex conductivity, neglecting electromagnetic induction. Considering the complex conductivity  $\sigma^*(x, z, \omega)$  at a given frequency  $\omega$  with a point source at the origin with (zero-phase) current  $I$ , the Poisson's equation can be defined as follow:

$$\frac{\partial}{\partial x} \left( \sigma^* \frac{\delta \sigma^*}{\delta x} \right) + \frac{\partial}{\partial z} \left( \sigma^* \frac{\partial \phi^*}{\partial z} \right) - \lambda^2 \phi^* \sigma^* = -I \delta(x) \delta(z) \quad (4)$$

where  $\phi^*$  is the Fourier-transformed complex potential,  $\lambda$  is the Fourier transformation variable for the assumed strike ( $y$ ) direction and  $\delta$  represents the Dirac delta function.

Once the frequency domain potential  $\phi^*$  is computed, the time domain computation is carried out through a cosine/sine transform, solved numerically in terms of Hankel transforms, expressed in terms of Bessel functions of order  $-1/2$  and  $+1/2$ , respectively (Johansen and Sørensen, 1979):

$$\frac{1}{\pi} \int_0^{\infty} f(\omega) \cos(\omega t) d\omega = \sqrt{r} \int_0^{\infty} f_1(\lambda) \lambda J_{\mp \frac{1}{2}}(\lambda r) d\lambda \quad (5)$$

$$\text{Where } r = t\sqrt{2\pi}, \lambda = \frac{\omega}{\sqrt{2\pi}} \text{ and } f_1(\lambda) = \frac{1}{\sqrt{\lambda}} f\left(\frac{\lambda}{\sqrt{2\pi}}\right).$$

Finally, the time-domain IP decay is computed as the convolution of the impulse response with the current waveform  $i(t)$  between the electrodes, solved as proposed by Fitterman and Anderson (1986) for piecewise linear current waveforms.

EEMverter is implemented in such a way that the inversion parameters are defined on the nodes of the model mesh and migrated to the forward mesh through interpolation (that can be chosen and selected by the user). The spatial decoupling between model and forward meshes allows for defining the model parameters, e.g., the Cole-Cole (Cole and Cole 1941; Pelton et al. 1978) ones, on several model meshes, one for each inversion parameter, for example.

For each dataset of the inversion process, a distinct forward mesh is defined. The interpolation from model parameters  $\mathbf{M}$  into the values  $\mathbf{m}_i$  is expressed through a matrix multiplication:

$$m_i = f_i(M) = F_i \bullet M \quad (6)$$

in which the matrix  $F_i$  holds the weights of the interpolation that depends only on the distances between model mesh nodes and the subdivisions of the  $i^{\text{th}}$  forward mesh (Fiandaca et al., 2024).

As for the forward response, the Jacobian matrix is computed in the frequency domain and then transformed into the time domain. The time-domain Jacobian in the  $i^{\text{th}}$  forward mesh is computed as:

$$J_{m_i,TD} = A \bullet T \bullet J_{m_i,FD} \quad (7)$$

where the matrix  $T$  holds the Hankel coefficients, the matrix  $A$  implements the effects of current waveform, gate integration and filters and the frequency-domain Jacobian  $J_{m_i,FD}$  is calculated in 1-D through finite difference and in 2-D/3-D using the adjoint method and the chain rule as in Fiandaca et al. (2013) and Madsen et al. (2020), thus allowing to use any parameterization of the IP phenomenon in the inversion:

$$J_{m_i,FD} = J_{\sigma^*,i} \bullet \frac{\partial \sigma^*}{\partial m_i} \quad (7)$$

where  $J_{\sigma^*,i}$  is the Jacobian of the  $i^{\text{th}}$  forward mesh with respect to the complex conductivity  $\sigma^*$

and  $\frac{\partial \sigma^*}{\partial m_i}$  is the partial derivative of the complex conductivity versus the model parameters

(Fiandaca et al., 2024).

The Levenberg-Marquardt linearized approach is used for computing the inversion model:

$$M_{n+1,j} = M_{n,j} + \left[ J_{M,j}^T C_d^{-1} J_{M,i} + R^T C_R^{-1} R_j + \lambda I \right]^{-1} \bullet \left[ J_{M,j}^T C_d^{-1} \bullet (d - f_{n,j}) + R^T C_R^{-1} R_j \bullet M_{n,j} \right] \quad (8)$$

where the subscript  $j$  indicates that the inversion process can be split in different inversion cycles: in each cycle  $j$  it is possible to change the forward computation for each dataset (e.g., from 1-D to 3-D), as well as to insert/remove data/constraints from the objective function (Fiandaca et al., 2023).

However, when using the resistivity and IP method to map subsurface geological structures with complex geometries, 1-D and 2-D inversion schemes are not always sufficient and 3-D modelling and inversion of the data are required. For this reason, EEMverter is also developed for 3-D inversion, following Madsen et al., (2020). To discretize the 3-D problem, a combined triple-grid inversion approach (presented by Günther et al. 2006) is adopted: a coarse tetrahedral mesh is used for the inversion (the model mesh) and two finer discretized tetrahedral meshes (one for the primary potential field and one for the secondary potential field) are used to compute the forward responses, balancing the modelling accuracy, the computational speed and memory usage. The results of the 2-D implementation on synthetic and field data, as well as the 3-D implementation under development, will be presented at the conference.

## References

- Binley, A. (2015). DC electrical methods.
- Cole, K.S. & Cole, R.H., (1941). Dispersion and absorption in dielectrics I. Alternating current characteristics, *J. Chem. Phys.*, **9**, 341–351.
- Fiandaca, G., Auken, E., Gazoty, A. & Christiansen, A.V., (2012). Time-domain induced polarization: full-decay forward modeling and 1D laterally constrained inversion of Cole-Cole parameters, *Geophysics*, **77**, E213–E225.
- Fiandaca, G., Ramm, J., Binley, A., Gazoty, A., Christiansen, A. V., & Auken, E. (2013). Resolving spectral information from time domain induced polarization data through 2-D inversion. *Geophysical Journal International*, *192*(2), 631-646.
- Fiandaca G., Christiansen A. and Auken E. (2015). Depth of investigation for multi-parameters inversions. Near Surface Geoscience 2015–21st European meeting of environmental and engineering geophysics.
- Fiandaca, G., Madsen, L.M. & Maurya, P.K., (2018). Re-parameterisations of the Cole–Cole model for improved spectral inversion of induced polarization data, *Near Surf. Geophys.*, **16**(4), 385–399.
- Fiandaca, G., Zhang, B., Chen, J., Signora, A., Dauti, F., Galli, S., Sullivan, N.A.L., Bollino, A., Viezzoli, A. (2024). EEMverter, a new 1D/2D/3D inversion tool for Electric and Electromagnetic data with focus on Induced Polarization. NGGTS 2024, 13-16 February 2024, Ferrara, Italy.
- Fitterman, D. V., & Anderson, W. L. (1987). Effect of transmitter turn-off time on transient soundings. *Geoexploration*, *24*(2), 131-146.
- Gazoty, A., Fiandaca, G., Pedersen, J., Auken, E., Christiansen, A.V. & Pedersen, J.K., (2012). Application of time domain induced polarization to the mapping of lithotypes in a landfill site, *Hydrol. Earth Syst. Sci.*, **16**, 1793–1804.
- Günther, T., Rucker, C. & Spitzer, K., 2006. Three-dimensional modelling and inversion of dc resistivity data incorporating topography - II. Inversion, *Geophys. J. Int.*, **166**, 506–517.

- Johansen, H.K. & Sørensen, K.I., (1979). Fast Hankel transforms, *Geophys.Prospect.*, **27**, 876–901.
- Kemna, A, (2000). Tomographic inversion of complex resistivity: theory and application, *Thesis*, Der Andere Verlag, ISBN 3-934366-92-9.
- Kemna, A., Binley, A., & Slater, L. (2004). Crosshole IP imaging for engineering and environmental applications. *Geophysics*, **69**(1), 97-107.
- Kemna, A., Binley, A., Cassiani, G., Niederleithinger, E., Revil, A., Slater, L., ... & Zimmermann, E. (2012). An overview of the spectral induced polarization method for near-surface applications. *Near Surface Geophysics*, **10**(6), 453-468.
- Madsen, L.M., Fiandaca, G., Auken, E. & Christiansen, A.V., (2017). Timedomain induced polarization - an analysis of Cole-Cole parameter resolution and correlation using Markov Chain MonteCarlo inversion, *Geophys. J. Int.*, **211**(2), 1341–1353.
- Madsen, L. M., Fiandaca, G., & Auken, E. (2020). 3-D time-domain spectral inversion of resistivity and full-decay induced polarization data—full solution of Poisson's equation and modelling of the current waveform. *Geophysical Journal International*, **223**(3), 2101-2116.
- Martin, T., Titov, K., Tarasov, A., & Weller, A. (2021). Spectral induced polarization: frequency domain versus time domain laboratory data. *Geophysical Journal International*, **225**(3), 1982-2000.
- Pelton, W.H., Ward, S.H., Hallof, P.G., Sill, W.R. & Nelson, P.H., (1978). Mineral discrimination and removal of inductive coupling with multifrequency IP, *Geophysics*, **43**, 588–609.
- Seigel H.O. (1959). Mathematical formulation and type curves for induced polarization. *Geophysics* **24**(3), 547–565.
- Seigel, H.O., Vanhala, H., Sheard, S.N., (1997). Some case histories of source discrimination using time-domain spectral IP. *Geophysics* **62**, 1394– 1408.
- Seigel, H., Nabighian, M., Parasnis, D. & Vozoff, K., (2007). The early history of the induced polarization method, *Leading Edge*, **26**, 312–321.
- Tarasov, A. & Titov, K., (2007). Relaxation time distribution from time domain induced polarization measurements, *Geophys. J. Int.*, **170**, 31–43.
- Vanhala, H., Peltoniemi, M., (1992). Spectral IP studies of Finnish ore prospects. *Geophysics* **57**, 1545–1555.
- Vanhala, H., Soininen, H., & Kukkonen, I. (1992). Detecting organic chemical contaminants by spectral-induced polarization method in glacial till environment. *Geophysics*, **57**(8), 1014-1017.
- Weller, A., Frangos, W. & Seichter, M., (1999). Three-dimensional inversion of induced polarization data from simulated waste, *J. appl. Geophys.*, **41**, 31–47.

Corresponding author: arcangela.bollino@unimi.it

# Differential arrival times for event location with DAS data

**E. Bozzi <sup>1</sup>, L. Gebraad <sup>2</sup>, A. Fichtner <sup>3</sup>, N. Piana Agostinetti <sup>1</sup>, G. Saccorotti <sup>4</sup>, T. Kiers <sup>3</sup>, T. Nishimura <sup>5</sup>**

<sup>1</sup> *University of Milano-Bicocca (Milan, Italy)*

<sup>2</sup> *Mondaic Ltd (Zurich, Switzerland)*

<sup>3</sup> *ETH Zurich, Institute of Geophysics (Zurich, Switzerland)*

<sup>4</sup> *Instituto Nazionale di Geofisica e Vulcanologia (Pisa, Italy)*

<sup>5</sup> *Tohoku University, Department of Geophysics (Tohoku, Japan)*

Standard seismic networks typically use absolute arrival times of specific seismic phases to estimate source locations. In this context, multiple sensors are positioned over a monitored area, aiming to minimize the azimuthal gap to known seismicity clusters. Distributed Acoustic Sensing (DAS) technology, which converts fiber optic cables (FOCs) into very dense seismic arrays, is nowadays used for similar purposes. DAS has the additional advantage of being able to exploit preexisting telecommunication FOCs (Telecom-FOCs). However, since the original installation purpose for Telecom-FOCs doesn't align with seismological needs, the spanned azimuthal directions can be limited. Hence, relying on absolute arrival times for event location might result in uncertain locations, given poor waveform moveouts and site-specific sources of noise in the data. Nevertheless, the intrinsic DAS channels' spatial density provide a good opportunity to test multi-channel cross-correlation techniques. Here, to assess the potential benefit from using differential arrival times for event location, we cross-correlate all possible DAS channel pairs and identify P-wave time delays. We focus on well-known test environments (i.e., known event locations) and use a Hamiltonian Monte Carlo algorithm to estimate hypocentral parameter uncertainties, considering both absolute and differential arrival times. We demonstrate how differential arrival times better constrain the events' azimuthal directions compared to absolute arrival times. However, computational costs are inevitably higher due to the significant increase in data points when considering all the P-wave delays. A mitigation to this issue is reached by selecting measurements based on thresholds for the minimum cross-correlation index and maximum interchannel distance. This work illustrates how to potentially alleviate DAS geometrical limitations on event location by exploiting selected differential arrival times.

Corresponding author: [e.bozzi3@campus.unimib.it](mailto:e.bozzi3@campus.unimib.it)

# A compact measuring system for UAV based magnetic anomalies surveys

R. Carluccio<sup>1</sup>, I. Nicolosi<sup>1</sup>, F. D'Ajello Caracciolo<sup>1</sup>, L. Minelli<sup>1</sup>

<sup>1</sup> *Istituto Nazionale di Geofisica e Vulcanologia (INGV)*

One of the most commonly used applications of potential fields in geophysics is the measurement of field anomalies in order to produce regional maps. These anomalies are in fact due to anisotropies in terrain geology and can give indirect information on underground layers/structures. In the magnetic field case, anisotropies are mainly due to differences in magnetic susceptibility and to the presence of magnetised material (remanence) in the underlying structures.

Magnetic anomaly maps are usually realised scanning the area of interest with a sensible magnetometer, usually following a parallel, equally spaced lines pattern properly oriented with respect to North.

Areas of interest can generally scale over orders of magnitude ranging from regional (thousands of square kms) to hundreds of square meters. Up to recent years this kind of measure has mainly been done either with airborne measuring systems, airplanes or helicopters or by walking on the ground in small areas. With the advent of UAV systems a series of intermediate targets have become possible since low altitude, square kilometres orders surveys, even on impracticable (by man) wild areas could be easily managed in a fraction of time.

In the case of UAVs, however, there are some technical aspects that arise regarding the magnetic anomaly measure. The magnetometers required for these measurements are usually protons precession or optical pumping total field units, which are heavy and impractical as UAV payloads, weighing several kilograms. However, they are necessary because the anomalies being searched for can often be as low as a few nanotesla, which is five orders of magnitude less than the average Earth magnetic field. Fluxgate magnetometers are small and sensitive enough for this task, but they are difficult to use. Even if they can achieve the required sensitivity, they only measure the magnetic field component along their symmetry axis. In a moving frame, the only way to obtain a meaningful measurement is to mount three of them in an orthogonal frame (creating a tri-axial unit) and calculate the magnetic total field based on those readings. However, this procedure is affected by several factors, including: 1) the calibration of the three units in terms of their response function to the magnetic field and external temperature, 2) the orthogonality of their axes, and to a lesser extent, 3) the mutual interaction of the three sensors in space. It can be demonstrated that these factors can result in an error in the calculated total field that is much larger than the precision requirements mentioned earlier, unless a thorough and challenging calibration is performed for each individual unit.

Only in recent months however a new family of optical pumped miniaturised magnetometers have become available. They have furthermore characteristics comparable to their big-sized relatives.

On the basis of this new technology we have designed from scratch and realised a flying payload mounted in an aerodynamic “rocket-shape” towed assembly. Our system core is a new optically pumped micro magnetometer from QSPIN, the Total-Field Magnetometer (QTFM). Along with this sensor the system has GPS positioning system running at 10 Hz, 9- DOF IMU unit for attitude and heading reference, barometer and thermometer for indirect absolute altitude measuring, laser altimeter (up to 50 m) for direct terrain clearance (AGL) measure.

All of these data are acquired along with milliseconds onboard processor clock for post processing data resync. Data is read from sensors synchronous to the magnetic measure acting as master sync and stored on a local repository.

A bi-directional radio link has also been implemented in order to communicate to a ground based station through LORA (Long Range) signal modulation. It ensures radio connections over long ranges even with very low antenna RF power through the use of a redundant and compressed data modulation scheme. This is important to maximise efficiency with respect to onboard battery weight. The enhanced efficiency is however paid on data bandwidth: for our system setup a maximum of about 22 bytes/second are allowed for connection nominal distances of 5 kilometres and few mW in TX.

Over this link a binary compacted subset of survey measurements is transmitted to a base station: the subset ensures the issue of a magnetic data map rendered on a laptop for real time quality check of survey progression. Even if magnetic data is transmitted to the base station in a simplified-rounded way for bandwidth optimisation it can nonetheless act as data backup in the unlikely cases of on-board log failure.

It is also possible to remotely control the system through a handshake (ready to send status - acknowledge) protocol to change some survey parameters: measurements frequency (future feature), control of recording status and of recording parameters setup for differential barometric altitude measurement.

Fig. 1 shows the magnetometer rocket-shaped system (bird): all of the electronics are in the nose of the bird running around an arduino-like powerful 32 bit microcontroller. The actual sensor is instead put farthest from the electronics and from the battery in order to minimise unwanted magnetic noise: it is in the bird tail, inside the wooden ailerons holder. Apart from the electronic components, the bird is in fact entirely made of non-magnetic materials and during flight it is towed by the UAV with a 10 metres rope.

The system has been conceived to be independent from the AUV host platform. It is furthermore very light weighting about 1kg, battery included. It is very economical if compared with similar commercial systems. It is low energy consuming: a ~5000 mAh USB power pack gives 2-3 hours of autonomy. The actual implementation of the system has demonstrated to fly stable in moderate velocities even with some wind conditions. Future improvements foresee the implementation of an active stabilisation system to minimise bird pendulum-like oscillations for low velocity situations and/or caused by wind turbulence.

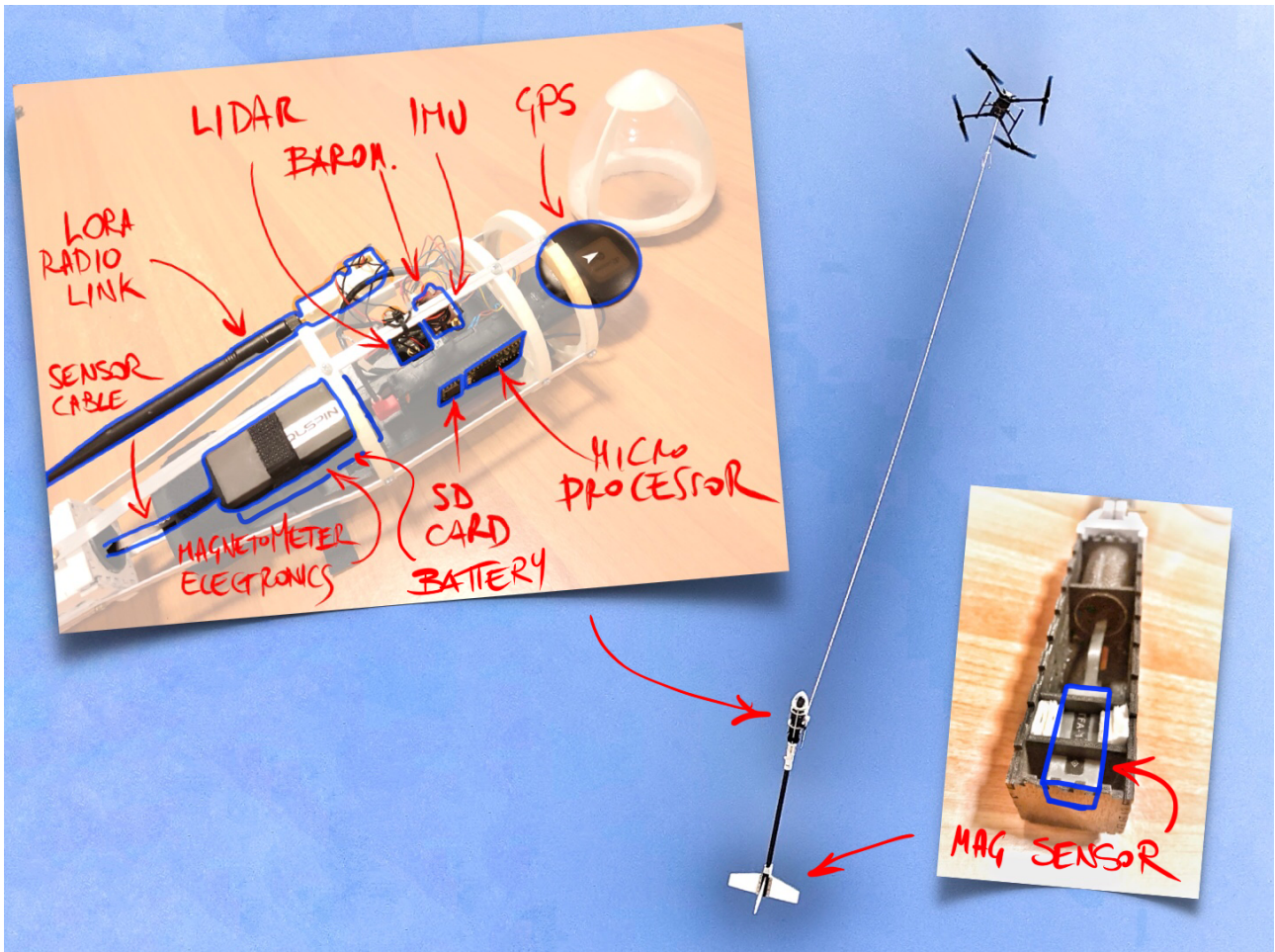


Fig. 1 – Bird towed by UAV with 10m cable with particular images showing operational parts and sensors.

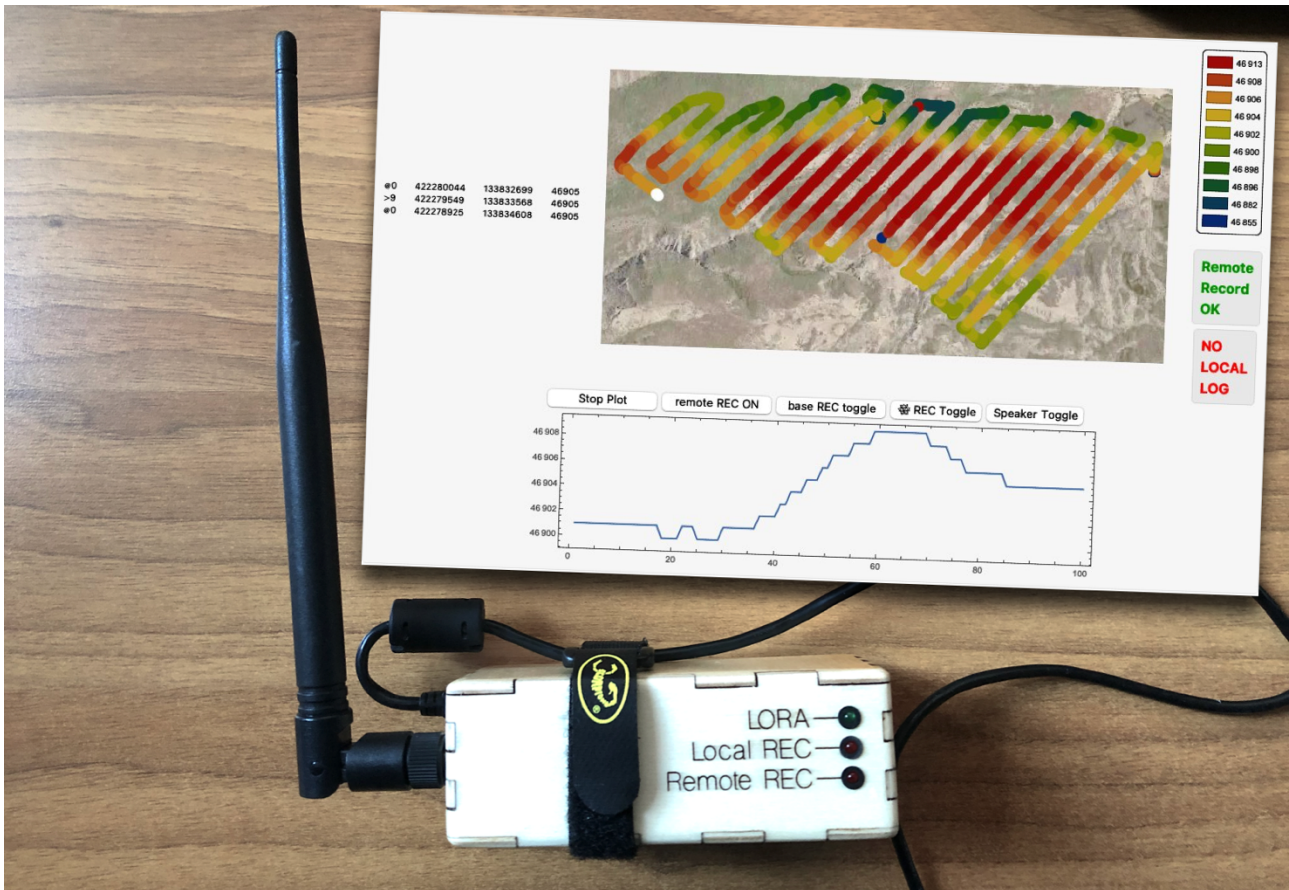


Fig. 2 – Base station LORA radio link together with a screengrab of the beta release of the real-time mapping software. Upper part of the software screen, from left to right: text dump of decoded data stream from the remote sensor, realtime geo-referenced map of survey raw data, adaptive and optimised real-time palette of magnetic field and messages flag signals. Lower part: moving chart of last 100 magnetic field measurements.

Fig. 2 is the base station system consisting of a LORA transceiver and binary packet demodulator USB connected to a laptop for real-time survey map rendering

Fig. 3 Shows processed a magnetic anomaly map of Campo Felice extensional basin, Abruzzo, central Italy, obtained from around 3-hour of UAV flight and a total profile length of 90 km. From post-flight analysis of measured data we have furthermore confirmed the reported sensor heading error to be less than 2 nanotesla.

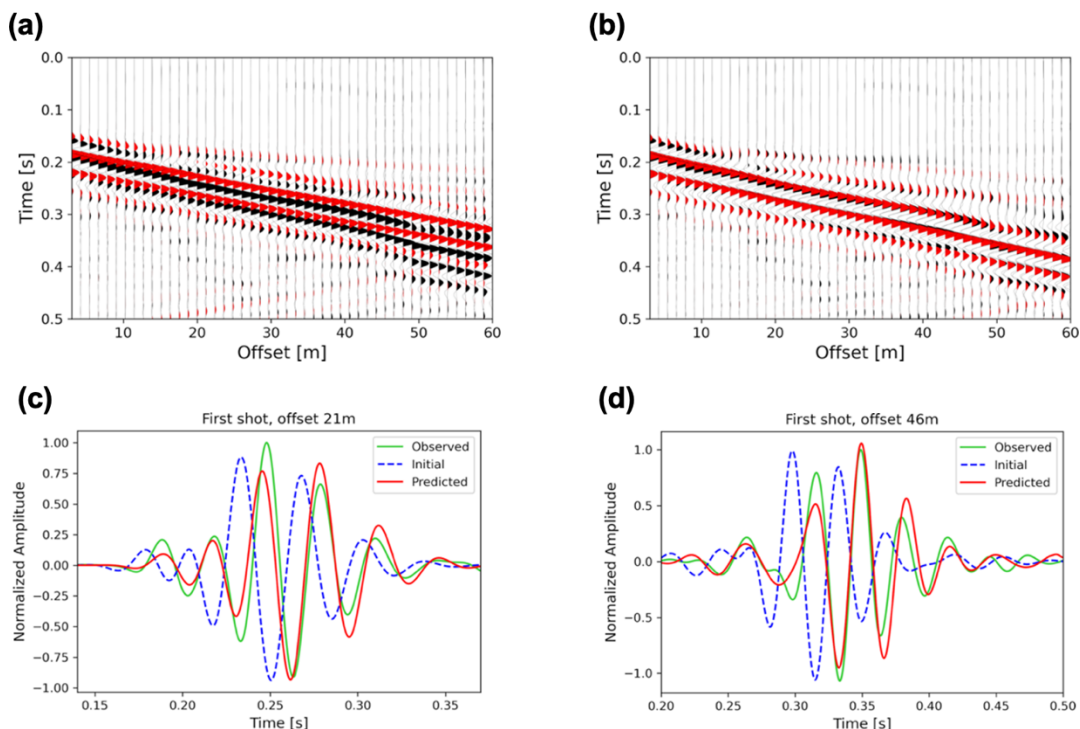


Fig. 3 – Reduced-To-the-Pole magnetic anomaly map of Campo Felice Plain displayed using a nonlinear intensity color scale and contour lines.

**Conclusions**

To recap, UAV-based surveys fill the gap between large-area airborne-based and ground-based magnetic surveys conducted by humans. In addition to the obvious advantage of being able to cover inaccessible areas, UAV surveys actually provide the highest resolution for geophysical surveys and open up new possibilities for local geological interpretation.



They have advantages over ground-based surveys, which in theory could offer greater resolution but are hindered by their close proximity to superficial sources that can potentially produce a dominant signal and obscure geological features. Man-based surveys also suffer from terrain topography and sensor oscillations caused by walking, which introduce external noise. In contrast, UAVs can fly at an optimal minimum distance to maximise the spatial resolution of the geologic signal by following a

smooth linear path that minimises external noise.

For example, we have successfully tested our system in different geological settings, such as intramontane Apenninic basins or mud volcanoes in Sicily, in order to characterise the subsurface geometry.

The QR code here reported points to the Youtube URL of a video showing one of the very first surveys conducted with the system that has been described.

# Bayesian imaging method for towed transient electromagnetic data using probabilistic neural networks

J. Chen<sup>1</sup>, G. Fiandaca<sup>1</sup>

*<sup>1</sup>The EEM Team for Hydro & eXploration, Department of Earth Sciences "Ardito Desio", University of Milano, Milano (Italy).*

## Abstract

The towed transient electromagnetic (tTEM) can conduct efficient geological surveys on the near-surface of about 100 meters underground. Exploring fast and accurate on-site interpretation strategies for electromagnetic data is crucial for geoscientists and engineers to make high-quality decisions and further enhance the applicability of this technology. In this study, we designed a composite probabilistic neural network (cPNN) structure that can simultaneously provide deterministic imaging and Bayesian probabilistic imaging results, providing a comprehensive interpretation of the observed data and estimating its uncertainty. We verified this neural network with nearly 200 km tTEM survey data collected on the Iseo Lake in Italy. The results show that the cPNN network can effectively characterize the location of aquifers and underground clay layers, and the imaging results are consistent with conventional inversion and sonar bathymetry data. Furthermore, since the cPNN network can obtain the Gaussian distribution of underground resistivity, we can estimate the depth of investigation (DOI) of the imaging results and extract smooth models from the Gaussian distribution. The cPNN network can obtain approximate Bayesian inversion results for large tTEM dataset in only tens of seconds on a laptop, which has good practical value.

## 1 Introduction

The towed transient electromagnetic (tTEM) is a new detection technology improved on the basis of the ground-based transient electromagnetic (TEM) method in recent years. This technology enables mobile geological surveys with all-terrain vehicles (Auken et al., 2019) or boats (Maurya et al., 2022), similar to the ground-based version of airborne transient electromagnetic (ATEM) technology (e.g. Silvestri et al., 2019). The survey speed of the tTEM system can reach nearly 20 kilometers per hour (Grombacher et al., 2021), and it can conduct efficient and low-cost geological surveys in large survey areas, with a typical depth of investigation (DOI) ranging from 80 to 100 meters.

At present, the tTEM has been successfully applied in various near-surface geological exploration fields such as agricultural ecological management, groundwater hydrology system mapping

(Grombacher et al., 2021), and groundwater vulnerability assessment (Sandersen et al., 2021). When carrying out large-scale exploration tasks, it is important for equipment operators to view the imaging interpretation results of the detection data, which is conducive to their on-site judgment of geological characteristics and instrument working status, so as to make high-quality decisions.

In recent years, a large number of studies have demonstrated the feasibility of deep learning algorithms in real-time imaging of TEM data (Colombo et al., 2021; Chen et al., 2022). These studies established a specific mapping between the exploration data and the resistivity parameter space based on deep neural network (DNN) frameworks. However, due to the ill-posedness and multi-solution nature of the geophysical electromagnetic inverse problem, the same exploration data can have multiple or infinite different geological model solutions. This one-to-many mapping relationship brings great training difficulty to the deep learning network and also affects the reliability of applying deep learning networks to interpret TEM data.

In this context, the development of probabilistic neural networks (PNN) has provided an effective solution to the nonlinear inversion problems in geophysics. The currently typical PNN structures include mixture density networks (MDN) and invertible neural networks (INN). MDN can learn to map a vector to an n-dimensional conditional probability distribution and parameterize it as a Gaussian mixture model (GMM) to learn arbitrary probability distributions (Mosher et al., 2021). INN can learn the bidirectional mapping between inputs and outputs, and it can estimate the posterior probability density function (PDF) by introducing additional latent variables on the output side. Both of these network structures can effectively simulate Bayesian posterior inference and have been successfully applied in geophysical inversion methods.

Inspired by the outstanding research mentioned above, we propose a composite probabilistic neural network (cPNN) structure that incorporates the LSTM autoencoder network with both DNN and MDN network structures. This design allows for simultaneous deterministic imaging and probabilistic estimation of tTEM data. Furthermore, we are able to evaluate the depth of investigation (DOI) through the resistivity Gaussian distribution output by the cPNN network.

## **II Bayesian imaging framework**

As shown in Fig. 1, the Bayesian imaging framework based on the cPNN mainly includes three stages: data generation, network construction and training, and imaging result output. In the data generation stage, input data and label data for the entire network structure need to be prepared, including TEM response data and the corresponding theoretical resistivity model. In this study, considering the computational complexity caused by high-dimensional layer models and the superior shallow subsurface detection resolution of ground-based TEM compared to ATEM, the number of model layers is set to 30. We generated 30 depth interfaces within a range of 120 m underground using a log increasing with depth method. The last layer is assumed to be a semi-infinite half-space.

In the stage of imaging result output, the difference between MDN and conventional neural networks is that MDN outputs a conditional probability distribution, and it can learn arbitrary

probability distributions through Gaussian Mixture Models (GMMs). Taking TEM inversion as an example, suppose we have  $N$  training datasets  $R=\{\mathbf{d}_i, \mathbf{m}_i\}: i = 1, \dots, N\}$ , where  $\mathbf{d}$  and  $\mathbf{m}$  represent the input space of TEM data and the output space of resistivity model parameters, respectively. Given an input  $\mathbf{d}_i$ , if the trained resistivity model set  $\mathbf{m}_i$  satisfies a prior probability density function distribution, the structure of a conventional neural network will output the corresponding  $\mathbf{m}_i$  by minimizing the sum of squared errors on the set  $R$ . This output result will approximate the mean solution of the Bayesian posterior distribution  $p(\mathbf{m} | \mathbf{d})$  (Earp et al., 2020). In contrast, MDN can directly output an estimate of the Bayesian posterior distribution  $p(\mathbf{m} | \mathbf{d})$ .

### III cPNN network inversion results

The cPNN inversion has been tested on a FloaTEM survey carried out on the south shore of the Iseo lake to study the lake-groundwater interaction (Fig. 2), we carry out a waterborne tTEM (or FloaTEM) survey with a total survey line length of approximately 200 kilometers and a total of nearly 35,000 survey points (Galli et al., 2024). When carrying out measurements with the FloaTEM system, we installed a sonar sounding device on the boat to measure the bathymetry.

We compared the inversion results of the deep learning cPNN network with those based on the EEMverter (Fiandaca et al., 2024) modelling platform. The number of inversion layers and layer thickness are consistent with the deep learning training parameters. As shown in Fig. 3, both the DNN inversion results and the MDN inversion results output by the cPNN network similarly depict the hydrological characteristics under the Iseo lake, and its imaging results of the underground clay layer and underground aquifer are in good consistency with the inversion results of EEMverter. The gray grid in the figure is the bathymetry information of the lake water. It can be clearly seen that the imaging results of the cPNN network correspond well to the bathymetry information of the Sonar. The cPNN network takes about 35 seconds to invert Iseo data, while the EEMverter inversion based on the server platform takes approximately 6500 seconds.

### IV Conclusions

In this study, we proposed a cPNN network structure that integrates DNN imaging-Net and MDN Bayesian-Net, which can directly convert the observed tTEM data into a resistivity model and estimate its uncertainty. The MDN Bayesian-Net captures the posterior PDF of the geological model, providing both maximum probability model and DOI as references, while the DNN imaging-Net provides an estimation of the posterior PDF mean solution. The two imaging results of cPNN complement each other and provide fast and comprehensive geological resistivity information.

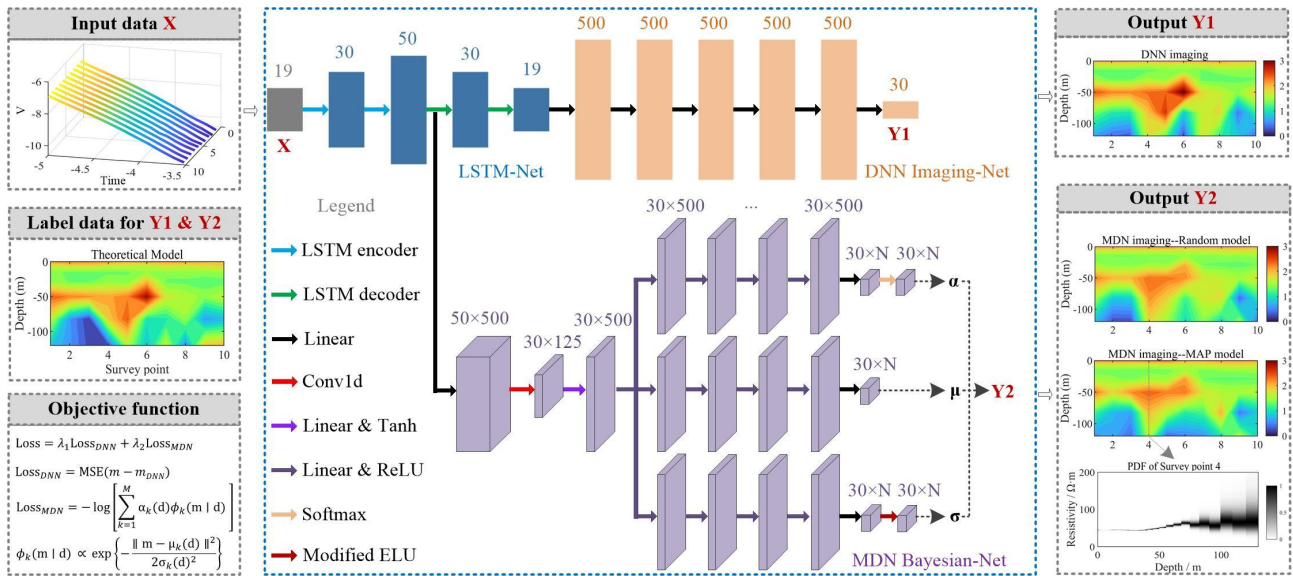


**Fig. 1** The composite probabilistic neural network structure diagram. The input data of the cPNN network structure is TEM response data, and the label data is the corresponding theoretical resistivity models (Y1, Y2). The output data includes the DNN resistivity model and the MDN posterior probability distribution function. In this study, we set N=1.

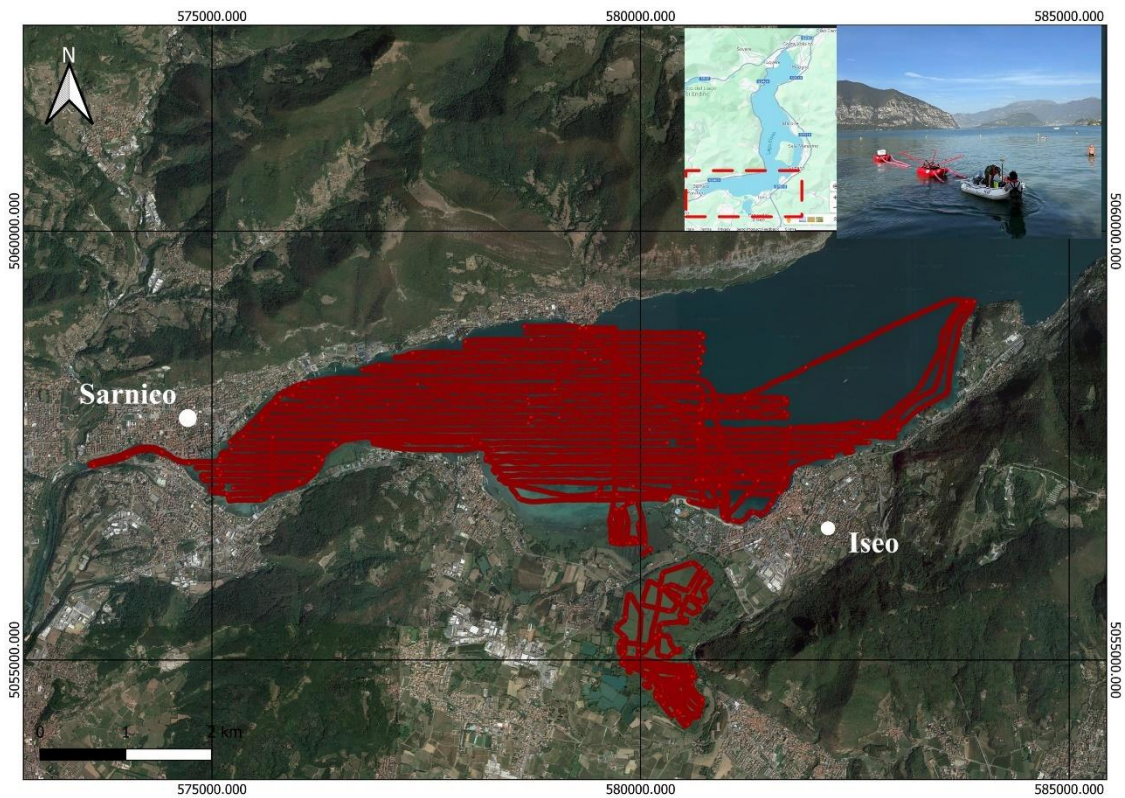


**Fig. 2** The distribution of tTEM survey lines of the survey carried out on the south shore of the Iseo lake, together with an image of the acquisition and a map of the lake.

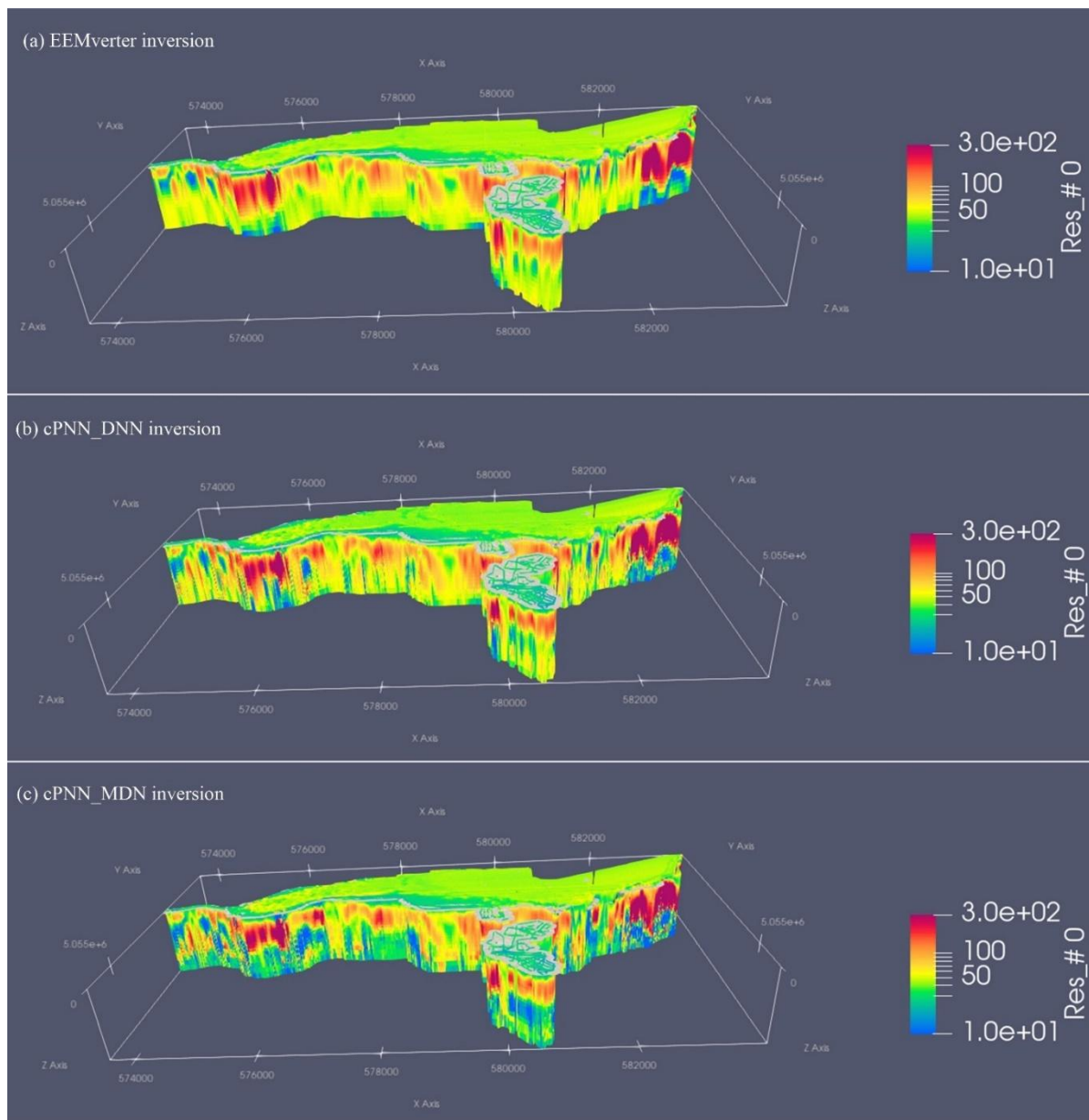


**Fig. 3** Iseo lake tTEM data inversion results. From top to bottom: a) EEMverter deterministic inversion; b) Deep learning Neural Network (DNN) output of the cPNN network; c) mean value of the Mixture Density Network (MDN) output of the cPNN network.

### Acknowledgments

This study has been carried out within the Horizon Europe project SEMACRET. The FloaTEM data have been acquired in the LakEMaging project, funded by Acque Bresciane.

## References

- Auken, E., Foged, N., Larsen, J. J., Lassen, K. V. T., Maurya, P. K., Dath, S. M., & Eiskjær, T. T. (2019). tTEM — A towed transient electromagnetic system for detailed 3D imaging of the top 70 m of the subsurface. *Geophysics*, *84*(1), E13–E22.
- Colombo, D., Turkoglu, E., Li, W., Curiel, E. S., & Rovetta, D. (2021). Physics-driven deep-learning inversion with application to transient electromagnetics. *Geophysics*, *86*(3), E209–E224.
- Chen, J., Zhang, Y., & Lin, T. T. (2022). Transient electromagnetic machine learning inversion based on pseudo wave field data. *IEEE Transactions on Geoscience & Remote Sensing*, *60*, 1–10.
- Earp, S., Curtis, A., Zhang, X., & Hansteen, F. (2020). Probabilistic neural network tomography across Grane field (North Sea) from surface wave dispersion data. *Geophysical Journal International*, *223*, 1741–1757.
- Fiandaca, G., Zhang, B., Chen, J., Signora, A., Dauti, F., Galli, S., Sullivan, N.A.L., Bollino, A., Viezzoli, A. (2024). EEMverter, a new 1D/2D/3D inversion tool for Electric and Electromagnetic data with focus on Induced Polarization. *NGGTS 2024*, 13-16 February 2024, Ferrara, Italy.
- Grombacher, D., Maurya, P. K., Lind, J. C., Lane, J., & Auken, E. (2021). Rapid mapping of hydrological systems in Tanzania using a towed transient electromagnetic system. *Groundwater*, 1–9.
- Galli, S., Signara, A., Chen, J., Schaars, F., Grohen, M., Fiandaca, G. (2024). Waterborne electromagnetic: two case studies. *NGGTS 2024*, 13-16 February 2024, Ferrara, Italy.
- Maurya, P. K., Christensen, F. E., Kass, M. A., Pedersen, J. B., Frederiksen, R. R., Foged, N., Christiansen, A. V., & Auken, E. (2022). Technical note: Efficient imaging of hydrological units below lakes and fjords with a floating, transient electromagnetic (FloaTEM) system. *Hydrology and Earth System Sciences*, *26*, 2813–2827.
- Mosher, S. G., Eilon, Z., Janiszewski, H., & Audet, P. (2021). Probabilistic inversion of seafloor compliance for oceanic crustal shear velocity structure using mixture density neural networks. *Geophysical Journal International*, *227*, 1879–1892.
- Neven, A., Maurya, P. K., Christiansen, A. V., Renard, P. (2021). tTEM20AAR: a benchmark geophysical data set for unconsolidated fluvio-glacial sediments. *Earth System Science Data*, *13*, 2743–2752.
- Prechelt, L. (1998). Early stopping — But when? *Neural networks: Tricks of the trade*, 55–69.
- Silvestri, S., Christensen, C. W., Lysdahl, A. O. K., Anschütz, H., Pfaffhuber, A. A., & Viezzoli, A. (2019). Peatland volume mapping over resistive substrates with airborne electromagnetic technology. *Geophysical Research Letters*, *46*, 6459–6468.
- Sandersen, P. B. E., Kallesøe, A. J., Mølle, I., Høyer, S., Jørgensen, F., Pedersen, J. B., & Christiansen, A. V. (2021). Utilizing the towed transient Electromagnetic method (tTEM) for achieving unprecedented near-surface detail in geological mapping. *Engineering Geology*, *288*, 106125.

Corresponding author: Jian.Chen@unimi.it

# Dynamic Strain Transients Clustering Using an Unsupervised Machine Learning Strategy

**B. Di Lieto<sup>1</sup>, P. Romano<sup>1</sup>, S. Scarpetta<sup>2</sup>, A. Sangianantoni<sup>1</sup>, G. Messuti<sup>2</sup>**

*<sup>1</sup>Istituto Nazionale di Geofisica e Vulcanologia, Osservatorio Vesuviano, Napoli, Italy;*

*<sup>2</sup>Università degli Studi di Salerno, Dipartimento di Fisica "E. R. Caianiello", Salerno, Italy.*

In recent years, machine learning techniques have been exploited in volcanology in order to assess natural hazards, volcano dynamics changes and early warning information. Among all the other approaches followed so far, unsupervised algorithms have shown to be particularly reliable in dealing with huge datasets, thanks to their ability to exploit the underlying information carried by the dataset and classify data characteristics without the need to label the training dataset. Since assigning target labels to the training dataset may be hard and time-consuming in many cases, unsupervised strategies that exploit unlabelled data, have been successfully employed as a clustering and visualization tool in exploratory data analysis in a wide range of applications. Self-organized neural systems (SOM), specifically, have the intrinsic capability to analyze large sets of high-dimensional data and can be implemented in an online learning manner. A SOM algorithm was successfully applied to classify VLP events recorded from a borehole strainmeter at Stromboli volcano during the explosive sequence that occurred during the summer of 2019, when two distinct paroxysms, happened about a month and a half apart, violently shook the volcano. Stromboli is an active, open-conduit strato-volcano, characterized by moderately persistent volcanic activity with a paucity of deformation episodes, always a candidate as a natural laboratory for researchers investigating eruptive precursors on open-conduit volcanoes. Following recent research, data recorded from borehole strainmeters carry several pieces of information inherent the static and dynamic deformations, due to the intrinsic capability of the instrument of recording high precision data within a wide frequency range. The extension of the time period previously examined, from 2018 to 2020 (fig. 1), has led us to find other correlations between observed phenomenologies and VLP shape variations.

Valuable information is embedded in the data used in the current work, which could be used not only for scientific purposes but also from civil protection agencies. Such a variety of possible usage needs the setting of principles and legal arrangements to be implemented in order to ensure that data will be properly and ethically managed, used and accessed from the scientific community.

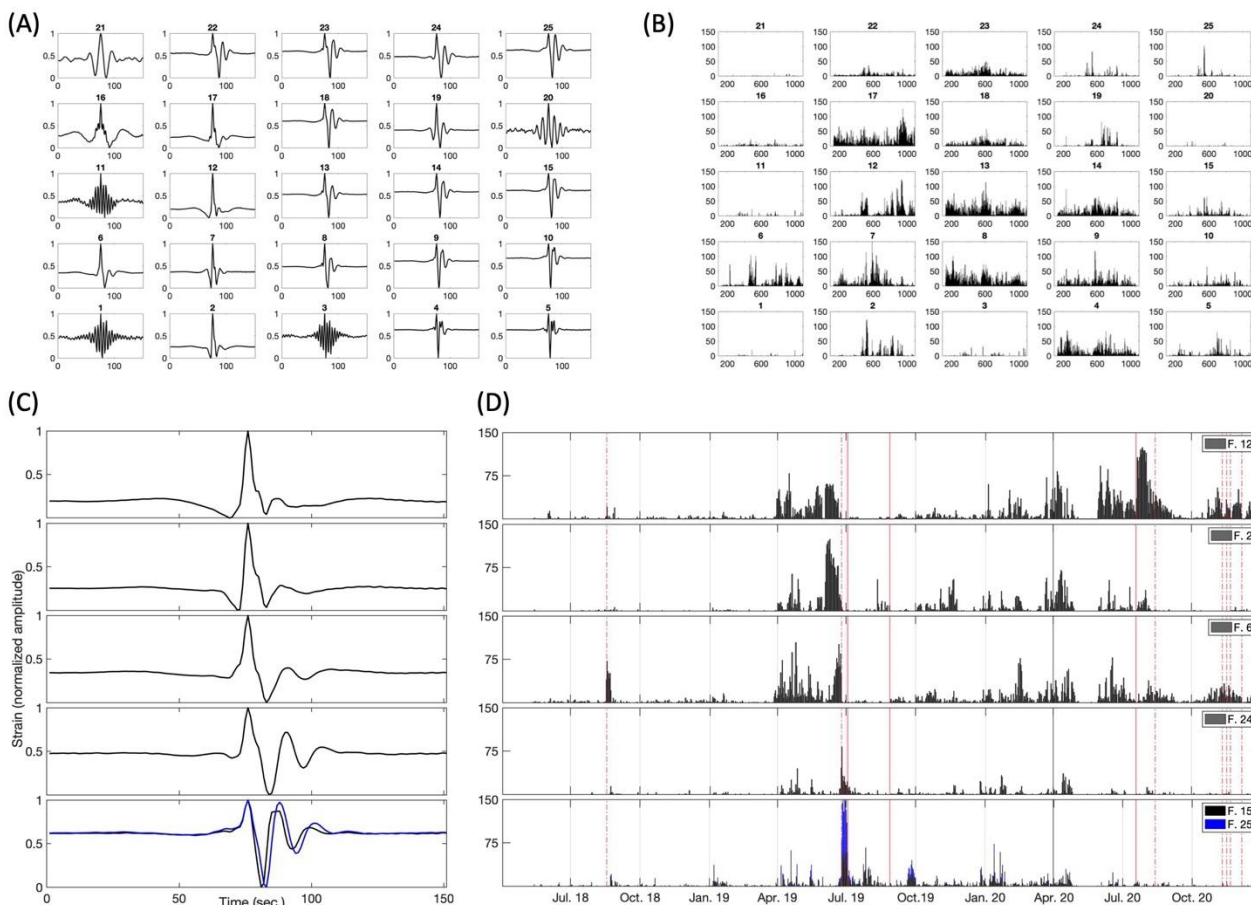


Fig. 1 – SOM cluster of families found in May 2018-December 2020 (A) Normalized stacked waveforms belonging to the  $i^{\text{th}}$  node of the SOM map (B) Temporal histograms of cumulative number of events per day belonging to the  $i^{\text{th}}$  node determined by the SOM algorithm (C,D) Normalized stacked waveforms and histograms of VLP data for noticeable families: black solid line marks the occurrence of the hybrid events on 31 March 2020; red dashed lines mark major explosions; the two red vertical solid lines mark the two paroxysmal events. (from Romano et al., 2022)

## References

Romano P, Di Lieto B, Scarpetta S, Apicella I, Linde AT and Scarpa R; 2022: Dynamic strain anomalies detection at Stromboli before 2019 vulcanian explosions using machine learning. *Front. Earth Sci.* 10:862086. doi: 10.3389/feart.2022.862086

Corresponding author: bellina.dilieto@ingv.it

# EEMverter, a new 1D/2D/3D inversion tool for Electric and Electromagnetic data with focus on Induced Polarization

G. Fiandaca<sup>1</sup>, B. Zhang<sup>2</sup>, J. Chen<sup>1</sup>, A. Signora<sup>1</sup>, F. Dauti<sup>1</sup>, S. Galli<sup>1</sup>, N.A.L. Sullivan<sup>1</sup>, A. Bollino<sup>1</sup>, A. Viezzoli<sup>3</sup>

<sup>1</sup> The EEM Team for Hydro & eXploration, Department of Earth Sciences “Ardito Desio”, Università degli Studi di Milano, Milano (Italy)

<sup>2</sup> Institute of Earth exploration, Science and Technology, Jilin University, Changchun (China)

<sup>3</sup> EMergo S.r.l. , Cascina (Italy)

## Introduction

The induced polarization (IP) phenomenon in airborne electromagnetic AEM data (AIP) presents a challenge to exploration in many parts of the world. It is a well-known phenomenon since Smith and Klein (1996) first demonstrated the presence of IP effects, which have been further discussed by several authors (e.g., Marchant *et al.*, 2014; Macnae, 2016; Viezzoli *et al.*, 2017). IP-affected AEM data are often interpreted in terms of the Cole-Cole model (e.g., Marchant *et al.*, 2014; Viezzoli *et al.*, 2017; Lin *et al.*, 2019), but the inversion problem is particularly ill-posed: for a 1D inversion of a single sounding four parameters have to be retrieved for each model layer. Furthermore, AIP and ground IP modelling are usually carried out in different inversion frameworks, making a direct comparison of the results difficult. In this study we present a novel inversion software, EEMverter, specifically developed to model electric and electromagnetic data taking into account the IP phenomenon. Three distinctive features have been implemented in EEMverter: i) 1D, 2D and 3D forward modelling can be mixed sequentially or simultaneously in the iterative process within multiple inversion cycles, for diminishing the computational burden; ii) the joint inversion of AIP, ground EM-IP and ground galvanic IP data is fully supported with a common IP parameterization; iii) time-lapse inversions of AIP, EM and galvanic IP data is possible with both sequential and simultaneous approaches. In the following, the implementation of EEMverter is described, with examples of synthetic and field inversion results.

## Method and results

In EEMverter the inversion parameters are defined on model meshes which do not coincide with the forward meshes used for data modelling: the link between model and forward meshes is obtained interpolating the model mesh parameters into the forward mesh discretization, as done for 1D AEM in Christensen *et al.* (2017), in 3D galvanic IP in Madsen *et al.* (2020) and in 3D EM in Zhang *et al.* (2021), Engebretsen *et al.* (2022) and Xiao *et al.* (2022a). This spatial decoupling allows

for defining the model parameters, e.g. the Cole-Cole ones, on several model meshes, for instance one for each inversion parameter. In this way, it is possible to define the spectral parameters, like the time constant and the frequency exponent in the Cole-Cole model, on meshes coarser than the resistivity and chargeability ones, vertically and/or horizontally, with a significant improvement in parameter resolution.

For each dataset of the inversion process, a distinct forward mesh is defined. The interpolation from the model parameters  $M$  defined on the model mesh nodes into the values  $m_i$  at the subdivisions of the  $i^{\text{th}}$  forward mesh is expressed through a matrix multiplication, in which the matrix  $F_i$  holds the weights of the interpolation, which depends only on the distances between model mesh nodes and the subdivisions of the  $i^{\text{th}}$  forward mesh:

$$m_i = f_i(M) = F_i \cdot M \quad (1)$$

In EEMverter 1D, 2D and 3D forward & Jacobian computations have been implemented. In particular, Transient EM data are modelled in 1D following Effersø et al. (1999); in 3D the forward solution is carried out in frequency domain, with the finite element method, both with tetrahedral elements or with the octree approach, similarly to what has been done with the time-stepping time-domain approach in Zhang et al. (2021) and Xiao et al. (2022a). The finite element approach is used also for frequency-domain galvanic computations in 2D (Fiandaca et al., 2013) and 3D (Madsen et al., 2020). The transformation to time-domain is obtained through a fast Hankel transformation (as in Effersø et al., 1999) for both the forward response and the Jacobian.

The Jacobian of the model space  $J_M$  is computed summing the contributions of all forward meshes up (Christensen et al., 2017; Madsen et al., 2020, Zhang et al., 2021), using the domain decomposition with a forward mesh for each sounding in 3D EM computations (Cox et al., 2010; Zhang et al., 2021):

$$J_M = \sum_i J_{m_i} \cdot F_i^T \quad (2)$$

The total Jacobian is used for computing the inversion model in a Levenberg-Marquardt linearized approach as follows:

$$M_{n+1,j} = M_{n,j} + \left[ J_{M,j}^T C_d^{-1} J_{M,i} + R^T C_{R,j}^{-1} R_j + \lambda I \right]^{-1} \cdot \left[ J_{M,j}^T C_d^{-1} \cdot (d - f_{n,j}) + R^T C_{R,j}^{-1} R_j \cdot M_{n,j} \right] \quad (3)$$

In equation (3) the subscript  $j$  indicates that the inversion process can be split in several inversion cycles: in each cycle  $j$  it is possible to change the forward computation for each dataset (e.g. from 1D to 3D), as well as to insert/remove data/constraints from the objective function.

Fig. 1 presents the model and forward meshes for a joint inversion, in which 1D AEM and 1D ground EM computations are combined with 2D galvanic computations.

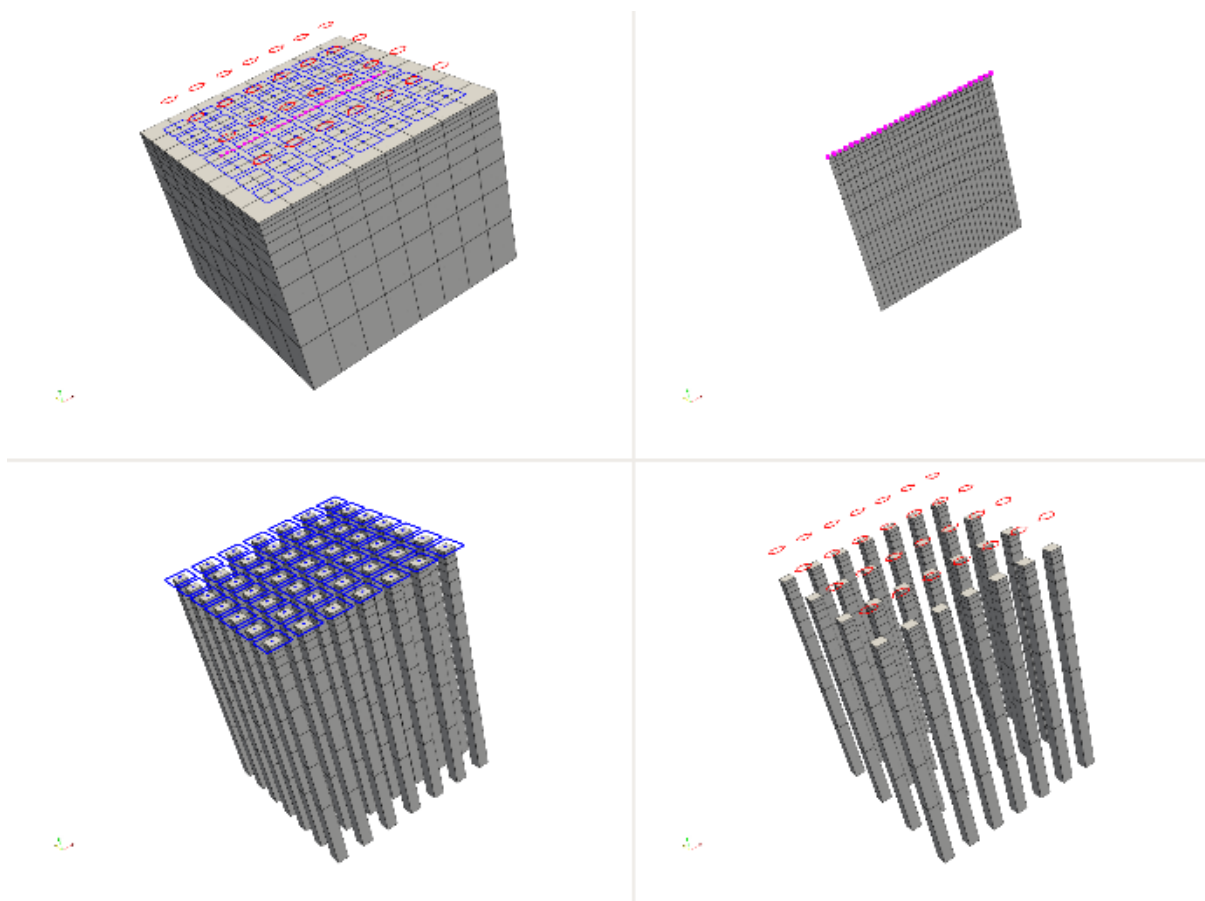


Figure 1. EEMverter multi-mesh inversion scheme for Joint inversion of inductive and galvanic data. Top left) Model mesh and data positions: red polygons for AEM frames; blue squares for ground TEM frames; magenta line for galvanic 2D profile. Top right) Galvanic 2D forward mesh. Bottom left) Ground TEM frames (blue squares) and corresponding 1D soundings (grey bars). Bottom right) AEM frames (red polygons) and corresponding 1D soundings (grey bars).

Fig. 2 presents the time-lapse approach of EEMverter, in which all the models of all the time steps can be inverted at once, without the need of relocating the model meshes when the positions of the acquisitions vary among the time steps, as in Xiao et al. (2022b).

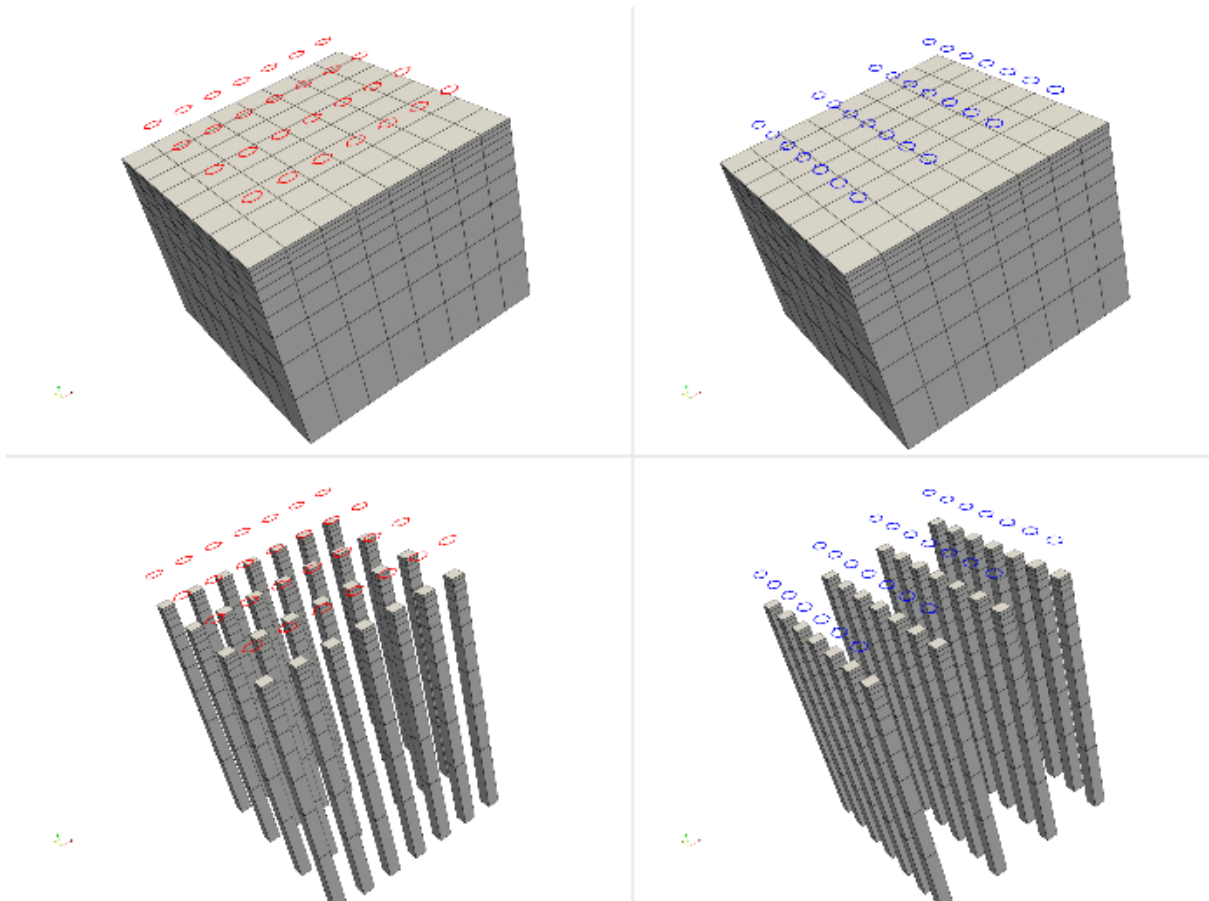


Figure 2. EEMverter multi-mesh inversion scheme for Time-Lapse inversion. Top left) Model mesh corresponding to the first Time-lapse acquisition (red polygons). Top right) Model mesh corresponding to the second Time-lapse acquisition (blue polygons), identical to the first model mesh despite of the different sounding positions. Bottom left) Forward meshes (grey bars) of the first acquisition (red frames). Bottom right) Forward meshes (grey bars) of the second acquisition (blue frames).

Fig. 3 presents the resistivity section of a synthetic model that mimics the electrical properties (both conduction and polarization) of sand, clay and consolidated formations, based on the petrophysical relations described in Weller et al. (2015), together with the inversion model of inductive and galvanic data. In particular, four different inversion results are presented: direct current and full-decay induced polarization (DCIP) galvanic data, with 10 m electrode spacing and 2D gradient sequence; AEM + ground EM data, with sounding distance of 40 m; AEM+ground EM + tTEM data (Auken et al., 2019), with tTEM soundings every 10 m; all data together in a joint inversion scheme.

The joint inversion presents much better resolution capability, with the inductive and galvanic data complementing each other in resolving both conductive and resistive layers. The same kind of improvement is found in Signora et al. (2024) with field data.

Another example of joint inversion of AEM and galvanic VES data in EEMverter, without IP modelling but with integration with resistivity logs is presented in Galli et al. (2024), where the asymmetric minimum support norm (Fiandaca et al., 2015) is used for an automated rejection of

conflicting borehole information. A similar approach is implemented in EEMverter also for automatic processing of AEM data (2021).

Examples of joint inversion of AEM, ground EM and galvanic IP data through EEMverter is presented in Dauti et al. (2024) in applications related to mineral exploration and in Signora et al. (2024) for the characterization of the HydroGeosITe, the Italian reference and calibration site for hydrogeophysical methods under development in Brescia, Italy.

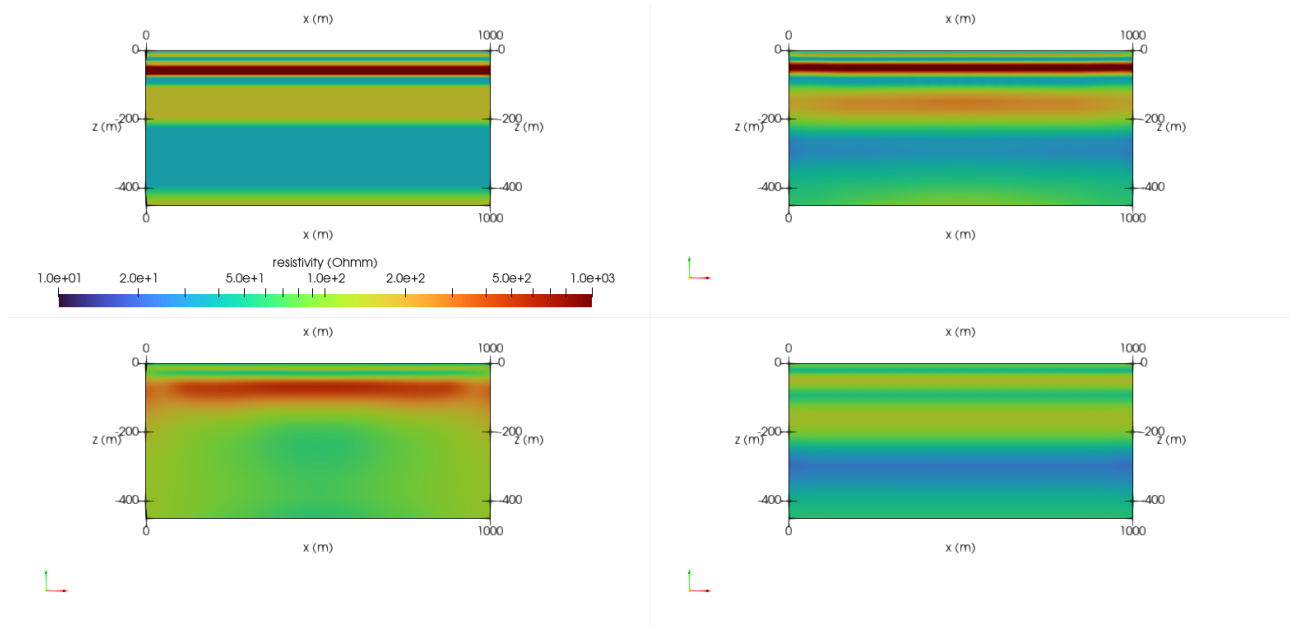


Figure 3. Synthetic model and inversion results. Top left) resistivity section of a MPA IP simulation of electrical properties; Bottom left) inversion model of DCIP data; Bottom right) inversion model of AEM+ground EM data; Top right) joint inversion of all inductive and galvanic data.

## Conclusions

We presented EEMverter, a novel inversion software for electric and electromagnetic data with focus on induced polarization. Three distinctive features have been implemented in EEMverter: i) 1D, 2D and 3D forward modelling can be mixed sequentially or simultaneously in the iterative process within multiple inversion cycles, for diminishing the computational burden; ii) the joint inversion of AIP, ground EM-IP and ground galvanic IP data is fully supported with a common IP parameterization; iii) time-lapse inversions of AIP, EM and galvanic IP data is possible with both sequential and simultaneous approaches. We believe that EEMverter, with its common inversion environment for the IP inversion of inductive and galvanic data will help in closing the gap between electric and electromagnetic data in AEM applications.

## Acknowledgments

This study has been partially carried out within the Horizon Europe project SEMACRET.

## References

- Auken E., Foged N., Larsen J.J., Trøllund Lassen K.V., Maurya P.K., Dath S.M., Eiskjær T.T. (2019). tTEM — A towed transient electromagnetic system for detailed 3D imaging of the top 70 m of the subsurface. *Geophysics*, 84 (1), E13-E22.
- Christensen, N. K., Ferre, T. P. A., Fiandaca, G., & Christensen, S. (2017). Voxel inversion of airborne electromagnetic data for improved groundwater model construction and prediction accuracy. *Hydrology and Earth System Sciences*, 21(2), 1321-1337.
- Christiansen, A. V., Auken, E., Foged, N., & Sørensen, K. I. (2007). Mutually and laterally constrained inversion of CVES and TEM data: a case study. *Near Surface Geophysics*, 5(2), 115-123.
- Cox, L. H., Wilson, G. A., & Zhdanov, M. S. (2010). 3D inversion of airborne electromagnetic data using a moving footprint. *Exploration Geophysics*, 41(4), 250-259.
- Dauti, F., Viezzoli, A., Fiandaca, G. (2024). Airborne and Ground IP: an integrated approach for exploration. *NGGTS 2024, 13-16 February 2024, Ferrara, Italy*.
- Effersø, F., Auken, E., & Sørensen, K. I. (1999). Inversion of band-limited TEM responses. *Geophysical Prospecting*, 47(4), 551-564.
- Engebretsen, K. W., Zhang, B., Fiandaca, G., Madsen, L. M., Auken, E., & Christiansen, A. V. (2022). Accelerated 2.5-D inversion of airborne transient electromagnetic data using reduced 3-D meshing. *Geophysical Journal International*, 230(1), 643-653.
- Fiandaca, G., Auken, E., Christiansen, A. V., & Gazoty, A. (2012). Time-domain-induced polarization: Full-decay forward modeling and 1D laterally constrained inversion of Cole-Cole parameters. *Geophysics*, 77(3), E213-E225.
- Fiandaca, G., Ramm, J., Binley, A., Gazoty, A., Christiansen, A. V., & Auken, E. (2013). Resolving spectral information from time domain induced polarization data through 2-D inversion. *Geophysical Journal International*, 192(2), 631-646.
- Fiandaca, G., Doetsch, J., Vignoli, G., & Auken, E. (2015). Generalized focusing of time-lapse changes with applications to direct current and time-domain induced polarization inversions. *Geophysical Journal International*, 203(2), 1101-1112.
- Fiandaca, G., Madsen, L. M., & Maurya, P. K. (2018). Re-parameterisations of the Cole–Cole model for improved spectral inversion of induced polarization data. *Near Surface Geophysics*, 16(4), 385-399.
- Fiandaca, G. (2021). Inversion-based automatic processing of AEM data. *Australasian Exploration Geoscience Conference AEGC2021, 13-17 September 2021, Virtual Conference*.
- Galli, S., Shaars, F., Smits, F., Borst, L., Rapiti, A., Fiandaca G. (2024). Automated integration of AEM data, VES and borehole logs. *NGGTS 2024, 13-16 February 2024, Ferrara, Italy*.

- Lin, C., Fiandaca, G., Auken, E., Couto, M. A., & Christiansen, A. V. (2019). A discussion of 2D induced polarization effects in airborne electromagnetic and inversion with a robust 1D laterally constrained inversion scheme. *Geophysics*, 84(2), E75-E88.
- Haber, E., Oldenburg, D. W., & Shekhtman, R. (2007). Inversion of time domain three-dimensional electromagnetic data. *Geophysical Journal International*, 171(2), 550-564.
- Kang, S., Oldenburg, D. W., & Heagy, L. J. (2020). Detecting induced polarisation effects in time-domain data: a modelling study using stretched exponentials. *Exploration Geophysics*, 51(1), 122-133.
- Lin, C., Fiandaca, G., Auken, E., Couto, M. A., & Christiansen, A. V. (2019). A discussion of 2D induced polarization effects in airborne electromagnetic and inversion with a robust 1D laterally constrained inversion scheme. *Geophysics*, 84(2), E75-E88.
- Marchant, D., E. Haber, and D. Oldenburg, 2014, Three-dimensional modeling of IP effects in time-domain electromagnetic data: *Geophysics*, 79, no. 6, E303–E314, doi: 10.1190/geo2014-0060.1.
- Madsen, L. M., Fiandaca, G., & Auken, E. (2020). 3-D time-domain spectral inversion of resistivity and full-decay induced polarization data—full solution of Poisson's equation and modelling of the current waveform. *Geophysical Journal International*, 223(3), 2101-2116.
- Signora, A., Galli, S., Gisolo, M., Fiandaca, G. (2024). The Italian calibration and reference site for E & EM geophysical methods: The HydroGeosITe. *NGGTS 2024, 13-16 February 2024, Ferrara, Italy*.
- Sullivan, N.A.L., Viezzoli, A., Fiandaca, G. (2024). EEMstudio: processing and modelling of electric and electromagnetic data in a QGIS plugin. *NGGTS 2024, 13-16 February 2024, Ferrara, Italy*.
- Viezzoli, A., V. Kaminski, and G. Fiandaca, 2017, Modeling induced polarization effects in helicopter time domain electromagnetic data: Synthetic case studies. *Geophysics*, 82, no. 2, E31–E50.
- Weller, A., Slater, L., Binley, A., Nordsiek, S., & Xu, S. (2015). Permeability prediction based on induced polarization: Insights from measurements on sandstone and unconsolidated samples spanning a wide permeability range. *Geophysics*, 80(2), D161-D173.
- Xiao, L., Fiandaca, G., Zhang, B., Auken, E., & Christiansen, A. V. (2022a). Fast 2.5 D and 3D inversion of transient electromagnetic surveys using the octree-based finite-element method. *Geophysics*, 87(4), E267-E277.
- Xiao, L., Fiandaca, G., Maurya, P. K., Christiansen, A. V., & Lévy, L. (2022b). Three-dimensional time-lapse inversion of transient electromagnetic data, with application at an Icelandic geothermal site. *Geophysical Journal International*, 231(1), 584-596.
- Zhang, B., Engebretsen, K. W., Fiandaca, G., Cai, H., & Auken, E. (2021). 3D inversion of time-domain electromagnetic data using finite elements and a triple mesh formulation. *Geophysics*, 86(3), E257-E267.

# Automated integration of AEM data, VES and borehole logs

**S. Galli<sup>1</sup>, F. Schaars<sup>2</sup>, F. Smits<sup>3,4</sup>, L. Borst<sup>5</sup>, A. Rapiti<sup>6</sup>, G. Fiandaca<sup>1</sup>**

<sup>1</sup> *The EEM Team for Hydro and eXploration, Dep. of Earth Sciences A. Desio, Università degli Studi di Milano, Milano (Italy)*

<sup>2</sup> *Artesia Water, 2871 BP Schoonhoven (The Netherlands)*

<sup>3</sup> *Waternet, 1096 AC Amsterdam (The Netherlands)*

<sup>4</sup> *Technical University of Delft, 2628 CD Delft (The Netherlands)*

<sup>5</sup> *PWN, 1991 AS Velsbroek, (The Netherlands)*

## Summary

Airborne electromagnetic (AEM) surveys are widely used for hydrogeological applications. Target areas for AEM campaigns may present a great deal of ancillary information (e.g., resistivity logs, lithology, etc.) and integrating them with AEM data is fundamental. Yet, using this information either as a-priori or a-posteriori may bring out conflicts between different datasets, preventing the fitting of all data. For instance, some borehole drillings may have been logged inaccurately, AEM data may present bias, or data may have been acquired at different times, with variations occurring in between.

In this study we present a way to integrate AEM data and other types of resistivity data (boreholes electrical logging and vertical electrical soundings, in this case), through an inversion scheme that identifies automatically conflicting data without preventing the general convergence of the process. In order to do so, we make use of a generalization of the minimum support norm, the asymmetric generalized minimum support (AGMS) norm, for defining the data misfit in the objective function of an iterative reweighted least squared (IRLS) gauss-newton inversion. The AGMS norm in the data misfit caps the weight of non-fitting data points, allowing for the inversion to focus on the data points that can be fitted. Outliers are identified after the AGMS inversion and excluded, in order to complete the inversion process with a classic L2 misfit.

We present an application of this method in the Netherlands, on a SkyTEM survey complemented with a vast and open-source database of ashore resistivity logs, as well as vertical electrical soundings (VES).

## Introduction

In areas rich with ancillary data, their integration in the inversion is a must, for validation as well as for enhancing sensitivity. However, data integration can be a tricky process for many reasons: biased data, difference in supporting volume along with their location, or they may have been acquired in different periods, with variations occurring in between due, for instance, to the depletion of groundwater resources or seawater intrusion.

Conflicting data in an inversion process can easily prevent the proper convergence of the inversion, but culling too much data out might throw out important information. The removal of conflicting information is even more difficult when there is a significant amount of ancillary information, acquired over a long period of time.

To solve this challenge, we propose to use a generalization of the minimum support norm (Last and Kubik, 1983; Portniaquine and Zhdanov 1999), namely the asymmetric generalized minimum support AGMS norm (Fiandaca et al., 2015), for identifying outliers in a joint inversion of AEM data, vertical electrical soundings (VES) and borehole resistivity logs. We test the method on a synthetic example, mimicking a joint inversion of AEM data and borehole logs, with both correct and incorrect logging, as well as real data. The field case consists of a SkyTEM survey carried out in 2022, complemented with a vast and open-source database of ashore resistivity logs, as well as VES, acquired over many decades.

## Method and results

The inversion of AEM, VES and borehole logs is carried out in EEMverter (Fiandaca et al., 2024), a new inversion algorithm in which different norms are applicable in the objective function for both data misfit and regularization through the iteratively reweighted least squared (IRLS) inversion scheme (Farquharson and Oldenburg, 1998).

In particular, the penalty of the data misfit  $x=d-f$  between data and forward response is expressed through the AGMS norm (Fiandaca et al., 2015) as:

$$\phi(x) = \alpha^{-1} \left[ (1 - \beta) \frac{\left(\frac{x^2}{\sigma^2}\right)^{p_1}}{1 + \left(\frac{x^2}{\sigma^2}\right)^{p_1}} + \beta \frac{\left(\frac{x^2}{\sigma^2}\right)^{p_2}}{1 + \left(\frac{x^2}{\sigma^2}\right)^{p_2}} \right] \quad (1)$$

where

$$\beta = \frac{\left(\frac{x^2}{\sigma^2}\right)^{(p_1, p_2)}}{1 + \left(\frac{x^2}{\sigma^2}\right)^{(p_1, p_2)}}. \quad (2)$$

In (1) and (2),  $\sigma$  is the data standard deviation,  $p_1$  and  $p_2$  control the shape of the norm before and after  $x/\sigma=1$  and  $\alpha$  determines the total weight of the penalty.

With this choice of values for the norm settings the AGMS norm gives misfit 1 for  $x/\sigma=1$  (i.e. the same value of the L2 norm), with similar penalty for low misfit (because of  $p_1=1$ ) and a slow growth of the penalty when  $x/\sigma>1$  (because of  $p_2=0.5$ ). This slow growth allows for applying the AGMS norm in an iterative minimization process, because a decrease in  $x/\sigma$  gives a measurable penalty reduction.

This data norm is applied in a IRLS inversion composed of three inversion cycles (Fiandaca et al., 2024) with 1D forward/Jacobian computations:

- 1.a preliminary cycle which finds the best starting model without vertical variability of the parameters, through the use of a single-layer forward mesh;
- 2.a cycle where the AGMS norm is applied
- 3.the data norm is switched to the L2 norm, to reject the data with misfit above the set thresholds, and the inversion is carried out until the reach of the minimum misfit.

In all cycles, borehole logs are treated as data, with the forward response of the logs consisting in the interpolation of the model resistivity at the log locations (Fiandaca et al., 2024).

Fig. 1 presents a synthetic model of a fresh aquifer enclosed between an unsaturated sand dune and a brackish aquifer, and confined by clay layers. AEM data (Xcite system, New Resolution Geophysics) and three borehole logs are simulated and inverted with a classic L2 data norm and the AGMS norm, with three data scenarios:

1. only AEM data are available (Fig. 1D and 1G);
2. AEM data are complemented with the logs that bear correct information (Fig. 1E and 1H);
3. one log contains wrong resistivity values (Fig. 1F and 1I).

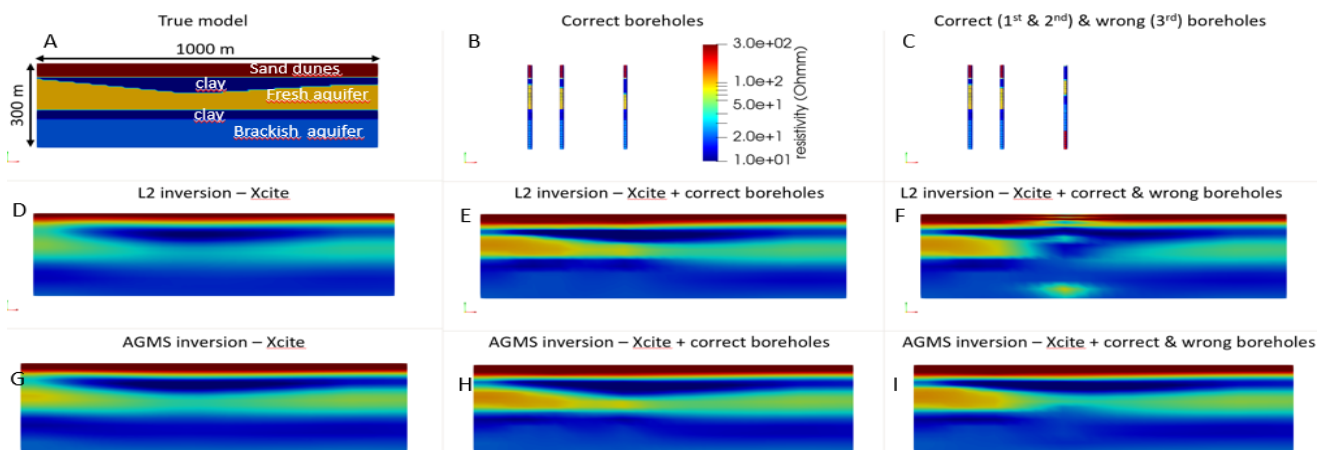


Figure 1. Conceptual model (A), boreholes information (all correct in B, one incorrect in C); model recovered by Xcite AEM data without drilling information using L2 norm (D) and AGMS norm (G); model recovered by Xcite with all correct drilling information using L2 norm (E) and AGMS norm (H); model recovered by Xcite with partially incorrect drilling information using L2 norm (F) and AGMS norm (I).

Both L2 and AGMS inversions improve the model retrieval when correct log information is added, but a very different behaviour occurs when wrong data are fed to the inversions: the L2 inversion shows a significant artifact at the location of the wrong resistivity log, while the AGMS inversion is almost insensitive to the outliers.

The same inversion procedure was used on a SkyTEM dataset acquired in the Netherlands in 2022, 25 kilometres west of Amsterdam (Fig. 2, top left inset), together with 94 borehole resistivity logs, 91 VES, acquired in the same area over a period ranging many decades, in which the volume of the fresh groundwater has changed considerably. Excessive water abstraction from deep wells between 1903 to 1957 caused depletion of fresh groundwater. In 1957 pumping stopped and infiltration with treated water from the river Rhine started. This enlarged the drinking water production capacity and restored the fresh water volume in the deep aquifer (Geelen et al., 2017; Olsthoorn and Mosch, 2020). The wells can still be used as a back-up system if the quality of the water in the river Rhine is not sufficient. That's why the integration of resistivity logs and VES with AEM data is difficult: data will conflict not necessarily because of their different support volume or sensitivity, but because they were acquired over different periods of time. Thus, with the AGMS inversion we aim at two distinct goals: improving the AEM inversion where borehole logs and VES information bring compatible information; identify the conflicting information, as a proxy of the variations that occurred on the fresh-sea water balance over the decades.

A 40 m x 80 m XY horizontal discretization and log-increasing depths from 5 to 400 m were used for the inversion, with the same three-cycle inversion scheme utilized for the synthetic case. Only borehole logs and VES data were rejected in the last cycle, the aim being to identify the information conflicting with the AEM data, which were carefully processed.

Fig. 2 presents the rejection rate for both log data and VES data with the AGMS joint inversion, in comparison with the rejection rate computed after an AEM-only inversion, in which log and VES data do not concur in the model definition. The rejection of log data is not applied to entire logs, but value by value along the borehole depth. So, the rejection rate indicates for each borehole log the fraction of values rejected. The overall rejection rates are presented also in Table 1.

Table 1: Comparison between rejection rates with AGMS joint inversion of AEM, VES and log data and with AEM-only inversion

	Total data	Data rejected with AGMS	Rejection rate %	Data rejected with AEM-only	Rejection rate %
<b>Borehole logs</b>	33646	4399	13	12646	38
<b>VESs</b>	1815	1159	64	1475	81

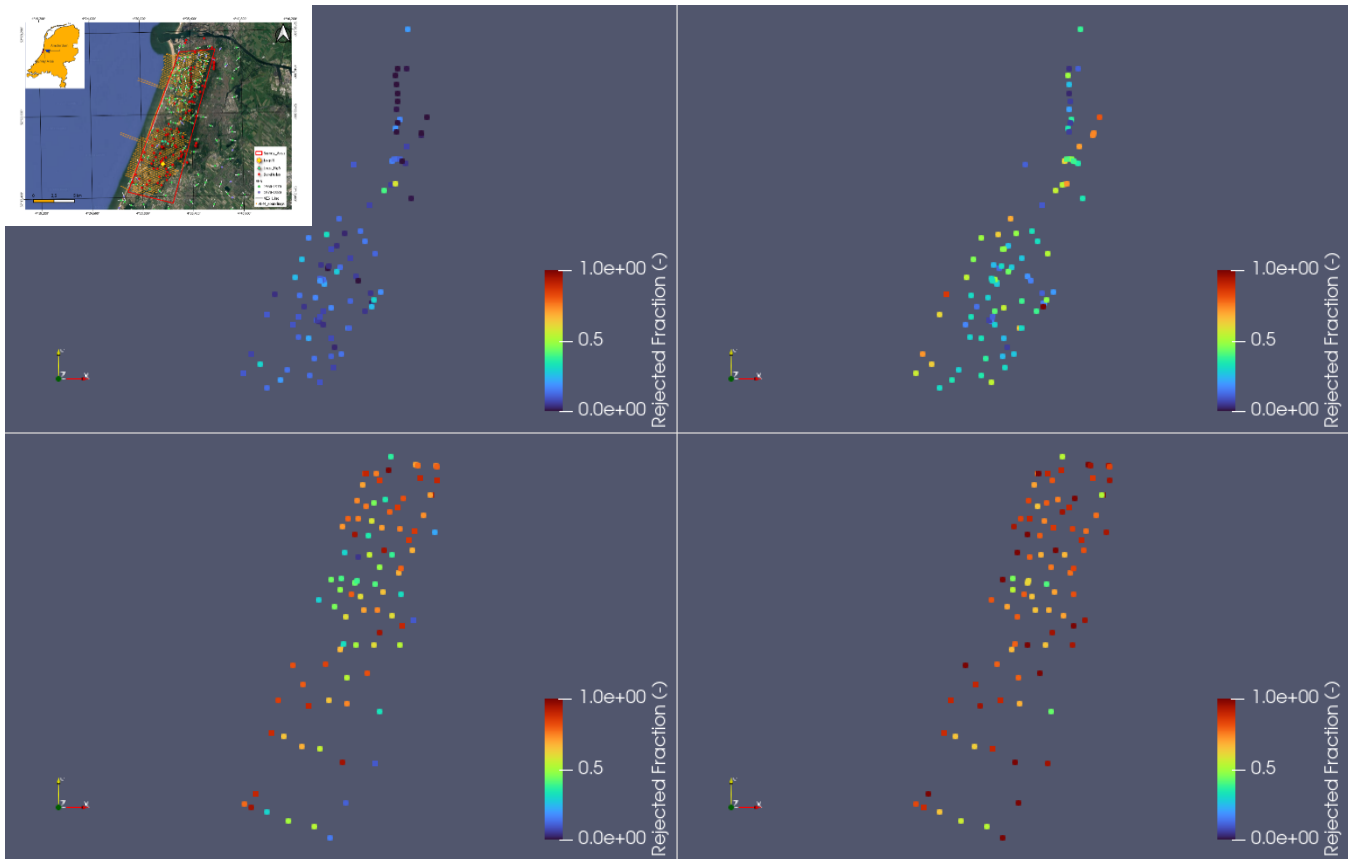


Figure 2. Plots of the fraction of rejected data with application of AGMS norm in joint inversion (left sections) and with AEM-only inversion (right sections); Top – rejections of log data; bottom – rejection of VES data. In the top right corner the surveyed area

As clearly shown by Fig. 2 and Table 1, the AGMS inversion has a much lower rejection rate, with very good compatibility between logs and AEM data, and poorer compatibility between the old VES data and the AEM ones. However, spatial patterns exist in the rejection fractions, which might be correlated with the variations occurred in the fresh-sea water interface. The AEM-only inversion has a much lower compatibility with the ancillary data, which is mostly due to equivalence problems instead of conflicting information.

Finally, Fig. 3 presents the comparison of the joint AGMS inversion and of the AEM-only inversion on an exemplary log, where AGMS inversion model fits much better the borehole information.

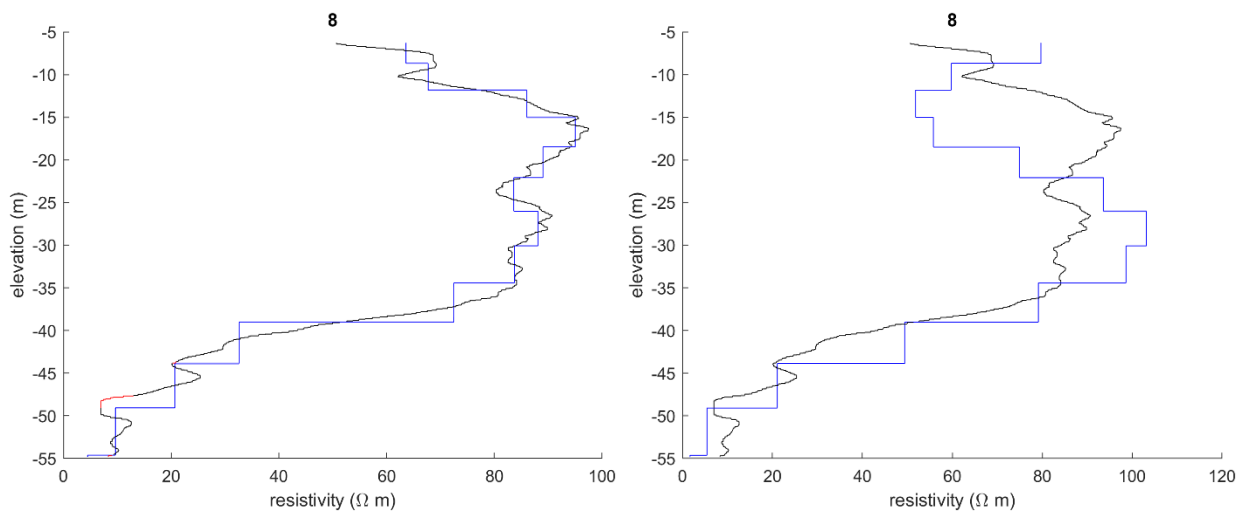


Figure 3. Comparison between Borehole#8 log (yellow star in Fig. 3) and inversion model. Left – AGMS joint inversion; right – AEM-only inversion. Blue lines – inversion model; black lines – resistivity logs; red lines – rejected data in resistivity log in the joint AGMS inversion.

## Conclusions

The inversion scheme proposed in this study allows an automated integration of AEM data and resistivity logs, as well as ground-based galvanic VES measurements, even in presence of conflicting information. The AGMS data norm puts a cap at the misfit penalty of outliers, and grants convergence to the inversion without culling valuable information out.

This approach allows to integrate to AEM surveys a great amount of ancillary data, without the need of careful and time-consuming data vetting: the accurate inspection of ancillary information could be reserved only to the data rejected by the automated scheme, with the kept data readily usable for further integration and interpretation.

Furthermore, this automated integration scheme is fully general, and can be applied not only to AEM data, but to any geophysical problem simply using the appropriate forward modelling.

## Acknowledgments

This work has been carried out within the project LakEMaging, funded by Acque Bresciane. The SkyTEM measurements are paid for by PWN, the municipality of Amsterdam, the waterboard Amstel, Gooi and Vecht, the Province of Noord-Holland and the Delta Programma Zoet Water (Delta Program for Fresh Water) of the Dutch Ministry of Infrastructure and Water Management.

## References

- Farquharson, C.G. & Oldenburg, D.W., (1998). Non-linear inversion using general measures of data misfit and model structure, *Geophysics*, 134, 213–227.
- Fiandaca, G., Doetsch, J., Vignoli, G., & Auken, E. (2015). Generalized focusing of time-lapse changes with applications to direct current and time-domain induced polarization inversions. *Geophysical Journal International*, 203(2), 1101-1112.
- Fiandaca, G., Viezzoli, A., Schaars, F. (2021). Advanced Automated Integration of Aem and drilling data, 48th IAH Congress, Brussels, Belgium, 6-10 september 2021.
- Fiandaca, G., Zhang, B., Chen, J., Signora, A., Dauti, F., Galli, S., Sullivan, N.A.L., Bollino, A., Viezzoli, A. (2024). EEMverter, a new 1D/2D/3D inversion tool for Electric and Electromagnetic data with focus on Induced Polarization, GNGTS 2024, 13-16 February 2024, Ferrara, Italy.
- Geelen, L. H. W. T., Kamps P. T. W. J., Olsthoorn T. N. (2017). "From overexploitation to sustainable use, an overview of 160 years of water extraction in the Amsterdam dunes, the Netherlands." *Journal of coastal conservation* 21.5: 657-668.
- Last, B.J. & Kubik, K., 1983. Compact gravity inversion, *Geophysics*, 48, 713-721.
- Olsthoorn, T. N., & Mosch, M. J. M. (2020). Fifty years artificial recharge in the Amsterdam dune area. In *Management of Aquifer Recharge for Sustainability* (pp. 29-33). CRC Press.
- Portniaquine, O. & Zhdanov, M.S., 1999. Focusing geophysical inversion images, *Geophysics*, 64, 874-887.

Corresponding author: stefano.galli2@unimi.it

# NUMERICAL PROBLEMS OF THE UNCERTAINTY ASSESSMENT OF THE SIBSON INTERPOLATION METHOD

M. Iurcev <sup>1</sup>, F. Pettenati<sup>1</sup>

<sup>1</sup> Istituto di Oceanografia e di Geofisica Sperimentale, OGS, Trieste

## Introduction

In 2022 we presented a note (Iurcev et al. 2022) on the assessment of uncertainties for the Natural Neighbours – hereafter NN - interpolation method (Sibson 1980, 1981) with bidimensional scalar data. This non-parametric interpolation method uniquely determines the interpolated data and is therefore classified as a deterministic method. However, it is important to quantify the uncertainties due to the spatial distribution of the dataset to be interpolated. The implementation of this approach is now reported in Iurcev et al. 2023. This approach is based on a gradient method derived from the bivariate version of the Mean Value Theorem MVT (also known as the Lagrange Theorem) in  $\mathbb{R}^2$ , combined with Sibson's formula for interpolation (Iurcev et al. 2023).

This deterministic method, based on the MVT, raises two major issues. The first problem concerns gradient estimation. The second issue is the unknown location of the points  $\xi_i$  of MVT, along the line between the interpolation point and the  $i$ -th Natural Neighbour. The purpose of this note is to show how we have tried to solve these two issues.

## Gradient estimation

In Iurcev et al. 2022, we presented an approach that is widely used in the literature. The approximation of the gradient using finite differences superimposed on a regular grid in which the function value is known or estimated. However, this method introduces an additional level of uncertainty as the function must be interpolated through the grid. The proposed approach is the Local Least Squares plane approximation of the unknown surface. The OLS (Ordinary Least Squares) approximation requires a subset of points  $\mathbf{x}_i, f(\mathbf{x}_i)$  in the neighbourhood. If there are at least three non-colinear points in  $\mathbb{R}^3$  space, the linear regression defines a plane whose slope is a possible gradient estimator. In this context, two different least squares strategies for computing the gradient for bivariate interpolation of surfaces are investigated by Belward et al. (2008). The two methods are based on the generalization of Moving Least Squares (MLS). The first method is the classical method based on a linear system of equations in which the gradient is derived by a second order truncated Taylor expansion. In the second method, the gradient is a consequence of the Finite Volume Method (FVM) solution which is used to solve a diffusion equation. Belward et

al. (2008) show that "the uniqueness of the gradient estimates, [using both methods], is not a result of the analytical properties of the approximation processes, it is a consequence of the method of linear least squares".

We studied some possibilities to compute the gradients by OLS, using the subset of points around a grid point. A method is an "n" estimate (based on NNs) and another using an "r" estimate (using the distance within a fixed radius). Of course, the choice of radius in the r-method is quite arbitrary, whereas the n-method is uniquely defined. If the radius is too small, the subset used for the OLS estimator may be for many interpolation points. If the radius is too large, the gradient estimate will be very poor. The best choice for the fixed radius depends on the local density of the dataset. As described in De Keyser et al. (2007), the method is only valid if the so-called spatial homogeneity condition is fulfilled.

To test the gradient, we used a random dataset of 500 points in the unitary square  $[0,1]^2$  of Franke (1979) function. The Franke function is a differentiable function that is often used as a test function in literature. The main problem for the optimal radius depends strictly on the local spatial density of the dataset, instead. The NN bypasses this problem, but at the same time is not feasible if we approximate the points  $\xi_i$  with the relative NNs, since the vectorial expression becomes zero. The statistical tests performed so far suggest that OLS gradient estimation with a fixed radius can provide reasonable estimates. There are many ways to combine gradient estimation and our equations. Since the Franke function is known, it is also possible to obtain a "semi-exact estimator" using its exact gradient. The only problem is the true location of points  $\xi_i$ , which must be approximated by the point of interpolation  $x^*$ , the data points  $x_i$ , the midpoint, or in some other way.

Although many interesting questions have been raised, the investigation is still ongoing and requires further analysis from both theoretical and experimental perspectives.

## References

- Belward J.A., Turner I.W., Ilić M.; 2008: *On derivative estimation and the solution of least squares problems*. J. Comp. and Appl. Math., 222, 511–523.
- De Keyser J., Darrouzet F., Dunlop M.W., Décréau P.M.E.; 2007: *Least-squares gradient calculation from multi-point observations of scalar and vector fields: methodology and applications with Cluster in the plasmasphere*. Ann. Geophys., 25, 971–987, [www.ann-geophys.net/25/971/2007/](http://www.ann-geophys.net/25/971/2007/).
- Franke R.; 1979: *A critical comparison of some methods for interpolation of scattered data*. Naval Postgraduate School, Monterey, CA, USA, Technical Report, NPS-53-79-003, <hdl.handle.net/10945/35052>.
- Iurcev M., Majstorovic M., Pettenati F.; 2022: Introduction to Interpolation Uncertainty of the Natural Neighbors Method (Sibson). 40° Convegno Nazionale Gruppo Nazionale di Geofisica della Terra Solida NGGTS.Online, 27-29 Giugno. 2022, Trieste. Abstract, 504-506.

Iurcev M., Pettenati F.; 2023: *Exploring error estimation methods for natural neighbour interpolation: preliminary research and analysis*. Bull. Geoph. and Oceanog., 64, 4, 433-448, December 2023; doi 10.4430/bgo00423.

Sibson R.; 1980: *A vector identity for Dirichlet tessellation*. Math. Proc. Camb. Philos. Soc. 87, 151–155.

Sibson R.; 1981: *A brief description of natural neighbor interpolation*. Interpreting Multivariate Data, V. Barnett editor, Chichester, John Wiley, 21-36.

Corresponding author: miurcev@ogs.it

# Ensemble-based Acoustic Full Waveform Inversion: A Synthetic Data Application

F. Macelloni<sup>1</sup>, M. H. Altaf<sup>1</sup>, M. Aleardi<sup>1</sup>, E.M. Stucchi<sup>1</sup>

<sup>1</sup> *Department of Earth Sciences, University of Pisa, Pisa, Italy*

## Introduction

Full Waveform Inversion (FWI) is one of the most powerful techniques to estimate the distribution of seismic wave velocity in the subsurface. The determination of the velocities from the recorded seismograms represents an inverse problem and FWI aims to solve it by exploiting the full information content of the data.

Despite the high resolution results that FWI is able to provide, there are some drawbacks we have to deal with when using this kind of optimization. One of them is the risk of being trapped in local minima of the objective function, which expresses the distance between observed and estimated data. This problem is mainly due to the lack of low frequencies in the data (cycle skipping issue) and to a starting model lying too far from the global minimum of the error function. To alleviate this problem, a global optimization approach could be adopted to replace the standard local, deterministic strategy, at the expense of a significant increase of the computational workload. Another limitation of the deterministic inversion is also the impossibility to assess the uncertainty affecting the estimated subsurface velocity model.

In this work we cast the FWI into a probabilistic framework. The aim of the work is twofold: making the FWI results less dependent from the starting model, while also estimating the uncertainty on the inversion outcomes. Therefore, our aim is not to estimate a single, best-fitting solution but providing as the final results the so called posterior probability density function from which extract significant statistical properties concerning the estimated model (i.e., mean model and the associated standard deviation).

In particular, we present an ensemble-based approach to FWI, using the Ensemble Smoother with Multiple Data Assimilation (ES-MDA) algorithm (Emerick et al., 2013). This method allows us to perform a Bayesian FWI by considering an ensemble of velocity models and iteratively updating each of these realizations. The underlying assumption is that data and model parameters follow a Gaussian distribution. MDA can be considered as an iterative version of the standard ES and, instead of a single and large correction, it performs multiple smaller updates, achieving good data predictions in less iterations. For additional details, see Thurin et al. (2019) and Aleardi et al. (2021b).

This kind of approach makes the inversion highly demanding from a computational point of view, so it is necessary to adopt some strategies to alleviate this effort: here we employ the Discrete Cosine Transform (DCT) to compress both data and model space. This technique reduces the number of unknown in the inversion and also the dimensions of the matrices and vectors involved in the ES-MDA approach. The DCT is a Fourier-related transform through which a signal can be expressed as sum of cosine functions. Since the DCT concentrates most of the energy of the signal in low order coefficients, it is possible to get an approximation of the original signal by discarding those that are very close to zero and retaining only the low order ones. Other information can be found in Britanak et al. (2010) and Aleardi et al. (2021a).

In this work we restrict the application of EB-FWI to a synthetic case, but its utilization to field data is being prepared. In fact, we processed a 2D seismic line from the FORGE (Frontier Observatory for Research in Geothermal Energy) geothermal experiment located in Utah, USA (Miller et al., 2018). Precisely for the purpose of applying a FWI to this dataset, we performed a dedicated processing, comprehensive of Migration Velocity Analysis (MVA), for improving the velocity field estimation.

### Method

In this work we use an ensemble-based approach implementing the ES-MDA algorithm to cast the FWI in a Bayesian inference framework. The ensemble-based method represents a data assimilation algorithm in which the posterior distribution consists of a set, also called ensemble, of model realizations. It can be demonstrated that ES corresponds to a single Gauss-Newton step, but it usually requires many iterations to ensure a good data prediction when compared to MDA, which speeds up the convergence performing multiple assimilations (corrections) of the data.

The steps of MDA algorithm are the following: choice of the number of data assimilations (iterations); generation of the starting ensemble of models drawn from a Gaussian prior distribution; for each iteration and for each model of the ensemble, computation of the data associated to each member of the ensemble, perturbation of each data and update of the models. A schematic representation of the algorithm is shown in Fig.1. The perturbation of each data vector is made according to

$$d^{\sim}_k = d + \sqrt{\alpha_i} C_d^{\frac{1}{2}} \cdot n,$$

where:  $d$  is the observed data,  $d^{\sim}_k$  is a random perturbation of the observed data,  $\alpha$  is called inflation coefficient,  $C_d$  is the data covariance matrix and  $n = N(0, Id)$ , with  $N(d, C_d)$  representing a Gaussian distribution and  $Id$  the identity matrix. The update of each model of the ensemble is defined as follows:

$$m_k^u = m_k^p + K^{\sim} (d^{\sim}_k - d_k^p),$$

with  $k = 1, \dots, N$ , where  $N$  is the number of models in the ensemble, the superscripts  $u$  and  $p$  refers to variable computed at the current iteration (updated) and to the previous one,

respectively, and  $d_k^p$  is the data associated to the  $k$ -th model  $m_k^p$ . The matrix  $K^{\sim}$  represents the so called Kalman gain, given by:

$$K^{\sim} = C_{md}^p (C_{dd}^p + \alpha C_d)^{-1}.$$

In the previous equation  $C_{md}^p$  is the cross-covariance matrix between the model  $m^p$  and the associated data  $d^p$ , whilst  $C_{dd}^p$  is the covariance matrix of the predicted data.

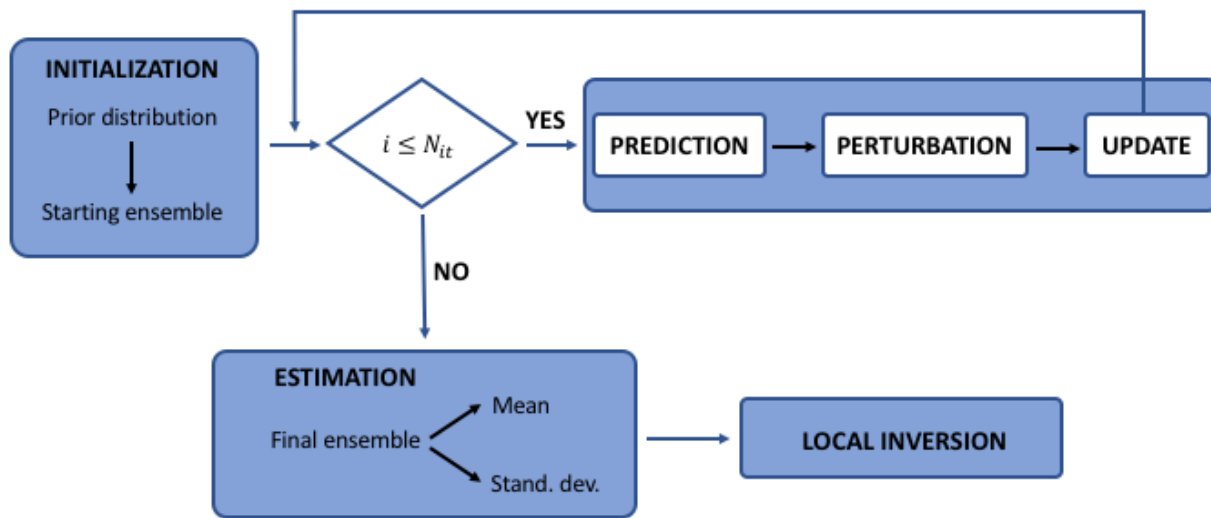


Fig. 1 – Schematic representation of the EB-FWI algorithm. This scheme also shows the possibility to apply a local FWI using as starting model the result of the global one. This step allows to improve the resolution of the result.

The velocity models forming the starting ensemble are drawn from a Gaussian prior distribution in which a Gaussian variogram has been included to impose the desired spatial variability on the velocity model.

The workload of the procedure can be alleviated by adopting a reparameterization technique able to considerably reduce the computational complexity of the problem. Among the possible methods, we choose the DCT for its compression ability, its linearity, the possibility to easily extend it to more than one dimension and because its application does not overload the inversion procedure with additional computational time. The compression power of this method relies on the fact that it is able to concentrate most of the information of the signal into the low order coefficients. As a consequence, the majority of these coefficients are very close to zero, and retaining only the low order ones is sufficient to approximate the original signal without losing relevant information. Furthermore, compressing data and model space, we considerably reduce the size of matrices and vectors involved in the computations. The DCT compression also mitigated the ensemble collapse issue, consisting in the fast convergence of the ensemble towards the mean and in the consequent underestimation of the posterior variance. The most common solution to

reduce this problem is to increase the ensemble size (Roe et al., 2016). The DCT, in this sense, helps in lowering the number of ensemble individuals needed to avoid collapse and, as a consequence, the number of forward modelling computations. We perform the compression through a 2D DCT, applying it in both horizontal and vertical directions. The choice of the number of DCT coefficients to retain in each direction is made through an analysis of the variability of the original signal that it is preserved after the compression. The variability is here defined as the ratio between the standard deviations of compressed and uncompressed signal (see Aleardi et al., 2021a).

### **Synthetic inversion**

We applied the ES-MDA acoustic FWI to a portion of the synthetic Marmousi benchmark model. The considered model extends 4.3 km horizontally and 1.340 km in depth. This is the portion that has been inverted, and it lies below a water layer 0.260 km deep, considered when computing the synthetic seismograms. The inverted portion was discretized with a grid characterized by a spacing of 20 m in both horizontal and vertical direction. This results in 216 nodes along the horizontal direction and 68 on the vertical one. A Ricker wavelet with a central frequency of 5 Hz is considered as the source signature. We simulated 5 shots equally spaced along the horizontal axis, from the left to the right edge of the considered area and recorded by 200 receivers, with a constant receiver interval of 21.6 m. The time interval is 4 ms and the record length is 3 s. We added to the observed data uncorrelated Gaussian noise, with a standard deviation equal to 10% of the standard deviation of the noise-free data.

We observed that retaining 30 DCT coefficients along the first (horizontal) dimension and 15 along the second (vertical) one was enough to properly represent about 95% of the variability of the original  $V_p$  model. In this way, we can compress the model space from  $68 \times 216 = 14688$ -D to  $15 \times 30 = 450$ -D. A similar analysis on the seismic data led us to use 55 DCT coefficients along the horizontal and 65 along the vertical direction. Considering that we simulate 5 shots, the original  $751 \times 200 \times 5 = 751000$  parameters are reduced to  $65 \times 55 \times 5 = 17875$  in the compressed data space.

A test phase has been performed to assess the minimum number of models within an ensemble needed to obtain a good reproduction of the main features of the original velocity model. We noticed that a good compromise between the quality of the results and the computational time was possible considering ensembles of 10000 models. Increasing this number does not lead to a considerable improvement of the inversion result, whilst it highly affects the computational cost of the procedure. We further observed that 10 iterations of the algorithm are enough to reach convergence. The computational time required by the EB-FWI is approximately 8 days.

The acoustic forward modeling has been performed using Devito, a python package that implements a high performance finite difference partial differential equation solver (Louboutin et al., 2019). We run the serial code implementing the inversion on a server equipped with Intel® Xeon® Silver 4114 CPU @ 2.20 GHz.

Fig.2 shows the result of the inversion, comparing the original model, the corresponding model after the DCT compression, the model used as mean of the prior distribution and the mean of the

final ensemble. As a prior mean model we used a gradient model, with velocity values increasing from top to bottom and ranging from the minimum to the maximum value of the original model (Fig.2-c). We observe that the model obtained with the EB-FWI (Fig.2-d) contains all the main features visible in the DCT-compressed version of the original portion of the Marmousi model. The main differences are placed on the bottom and in lateral portions of the model, where the algorithm is sometimes not able to correct high or low wrong velocity values. Anyway, this happens in the less illuminated parts of the model, characterized by higher values of the standard deviation (Fig.2-e). A comparison of observed and predicted data is shown in Fig.3, along with their difference. The represented shot is the third of the five simulated, and its position corresponds to the center of the horizontal extension of the model. The represented seismograms show a good fit between observed and predicted data. Fig.3-b shows the shot gather computed on the gradient model, used as the mean of the prior distribution. Considering that this is the seismogram associated with the mean of the starting ensemble and comparing the observed data (Fig.3-a) with the seismogram corresponding to the mean of the last ensemble (Fig.3-c), we clearly see that the algorithm appears able to properly reproduce the main events in the data.

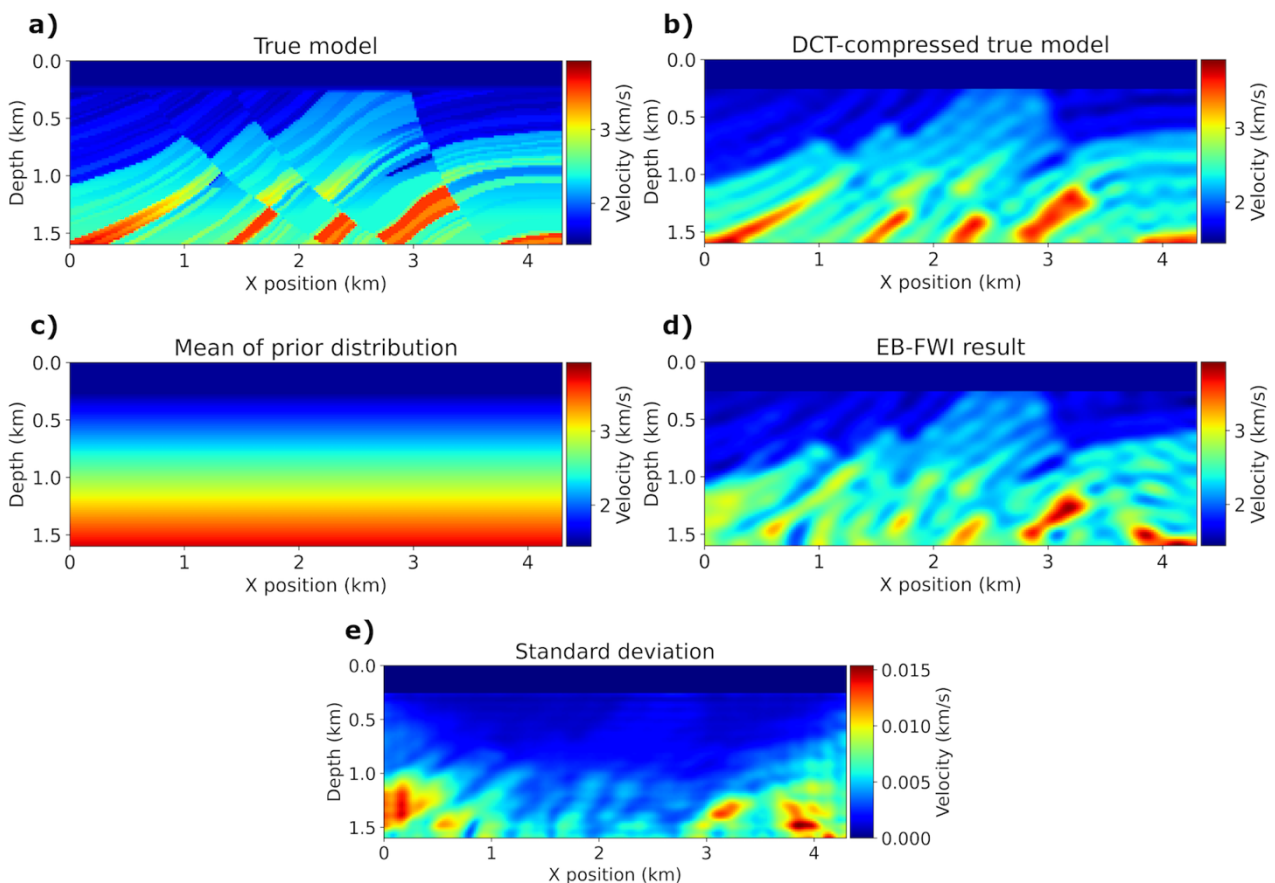


Fig. 2 – a) True model, portion of the synthetic Marmousi model; b) true model after the DCT compression; c) mean model of the prior distribution; d) final result of the EB-FWI; e) standard deviation associated to the inversion result.

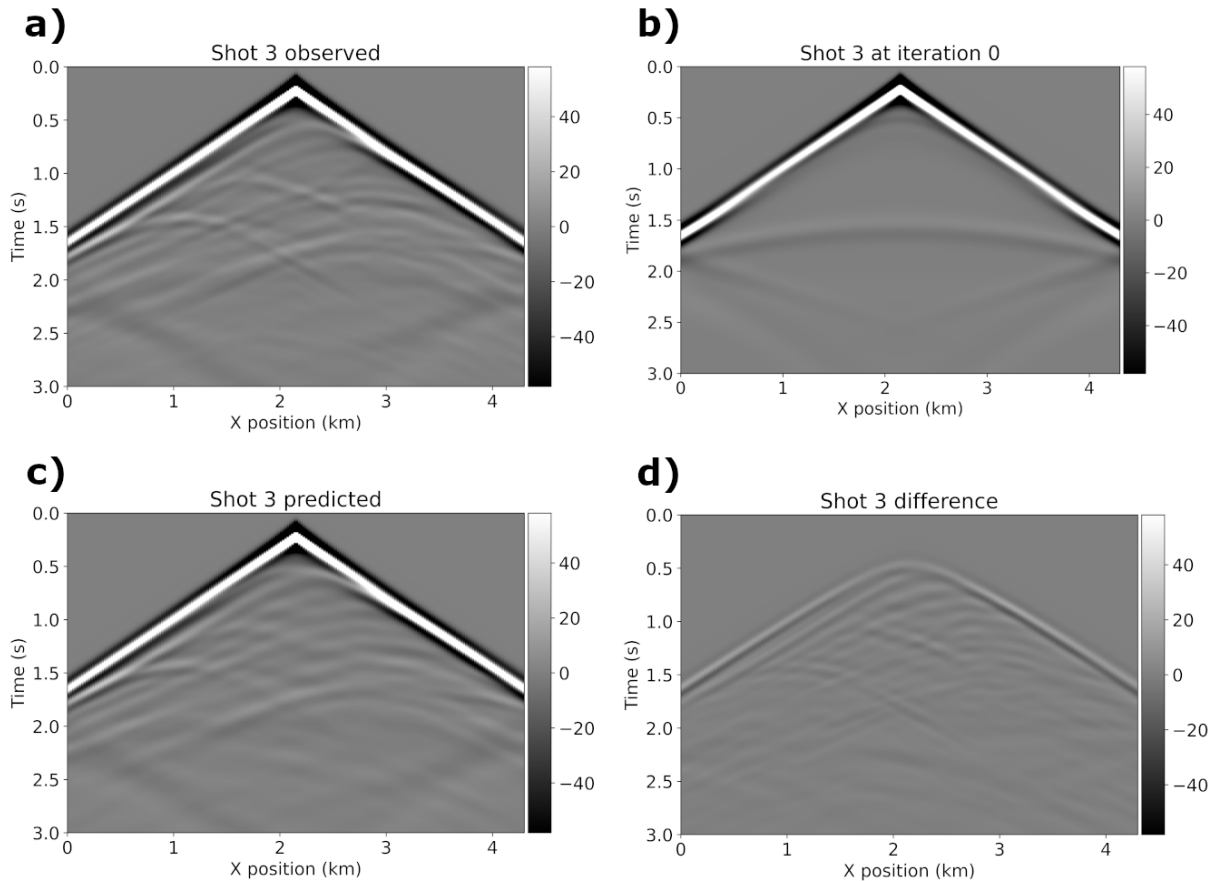


Fig. 3 – a) Observed seismogram; b) seismogram computed from the mean model of the prior distribution; c) predicted seismogram; d) difference between observed and predicted seismograms.

## Conclusions

We presented an ensemble-based approach to FWI using the ES-MDA algorithm. To reduce the computational effort required by such an approach, we compress both data and model space through a 2D DCT. We applied the algorithm to a portion of the synthetic Marmousi model in the acoustic approximation. The results are satisfactory: the mean of the final ensemble contains all the main features of the original, DCT compressed, model showing the main differences on the deepest portion and on the edges. Even in data space we observe a good fit between observed and predicted data. The algorithm appears able to deal with the cycle skipping issue mitigating it: to this end, some tests, not shown here for the lack of space, have been performed.

Future steps of this research are further tests on the algorithm, with the aim of approaching the application to field data. The code will also be improved to run in parallel, to considerably reduce the overall computational time. Further investigations will be carried out to obtain a more reliable estimation of the uncertainties.

## References

Aleardi M., Vinciguerra A. and Hojat A.; 2021a: A Convolutional Neural Network approach to Electrical Resistivity Tomography. *Journal of Applied Geophysics*, 193.

Aleardi, M., Vinciguerra, A., and Hojat, A.; 2021b: Ensemble-Based Electrical Resistivity Tomography with Data and Model Space Compression. *Pure and Applied Geophysics*, 178, 1781-1803.

Britanak, V., Yip, P.C., and Rao, K.R.; 2010: Discrete cosine and sine transforms: General properties, fast algorithms and integer approximations. Elsevier.

Emerick, A.A., and Reynolds, A.C.; 2013: Ensemble smoother with multiple data assimilation. *Computers and Geosciences*, 55, 3-15.

Louboutin, M., Lange, M., Luporini, F., Kukreja, N., Witte, P.A., Herrmann, F.J., Velesko, P., and Gorman, G.J.; 2019: Devito (v3.1.0): an embedded domain-specific language for finite differences and geophysical exploration. *Geoscientific Model Development*, 12(3), 1165-1187.

Miller, J., Allis, R., and Hardwick, C.; 2018: Seismic Reflection Profiling at the FORGE Utah EGS Site. *GRC Transactions*, vol. 42.

Roe, P., Almendral Vazquez, A., and Hanea, R.; 2016: Distinguishing Signal from Noise in History Matching – Analysis of Ensemble Collapse on a Synthetic Data Set. 15<sup>th</sup> European Conference on the Mathematics of Oil Recovery, 29 August – 1 September 2016, Amsterdam, Netherlands.

Thurin, J., Brossier, R., and Métivier, L.; 2019: Ensemble-based uncertainty estimation in full waveform inversion. *Geophysical Journal International*, 219(3), 1613-1635.

Fabio Macelloni, [fabio.macelloni@phd.unipi.it](mailto:fabio.macelloni@phd.unipi.it)

# Greenland and Antarctica ice mass balance (2002-2017) through source decomposition in hypercompact atoms.

M. Maiolino<sup>1</sup>, M. Fedi<sup>1</sup>, G. Florio<sup>1</sup>

<sup>1</sup>University of Naples "Federico II" – DiSTAR, Dipartimento di Scienze della Terra dell'Ambiente e delle Risorse

We present a new estimation based on a novel approach named ECS (Extremely Compact Sources) of the ice-sheet total mass variation in Greenland and Antarctica using time varying NASA GRACE (Gravity recovery and climate experiment) Stoke's coefficient data in the time span 2002-2017. Over a 15-year period the NASA missions GRACE (Gravity Recovery and Climate Experiment) and the following GRACE-FO provided a unique opportunity to map the changes in Earth's gravitational field and gave to the scientific community a new vision of the major ice sheet dynamics. In the last years, it has become clear that the ice sheet total mass response to climate change is crucial for understanding the sea level rising phenomena related to grounded ice melting and to quantify the ice sheet front retreat in the polar regions. Even if an approximation of the total mass changes in the polar regions can be done with the standard methods, namely the conversion method (Wahr et al., 1998) or the point mass inversion (Baur et al., 2011), a major issue in the GRACE data interpretation comes from the leakage effect caused by the presence of outlying melting ice bodies which gravity effects interfere each other. Our estimation uses a novel approach that, exploiting the non-uniqueness of the gravity field, retrieves a hypercompact model of the sources by an iterative inversion. We will show that this approach solves the inherent leakage effects of the GRACE data and, thanks to the extreme compactness of the sources, allow us to do a quantification of the total mass loss in the study area with less ambiguity.

## References

- Baur, O., Sneeuw, N.; 2011: *Assessing Greenland ice mass loss by means of point-mass modeling: a viable methodology*. J Geod 85, 607–615. DOI <https://doi.org/10.1007/s00190-011-0463-1>.
- Wahr, J., M. Molenaar, and F. Bryan.; 1998: *Time variability of the Earth's gravity field: Hydrological and oceanic effects and their possible detection using GRACE*. J. Geophys. Res., 103(B12), 30205–30229, DOI:[10.1029/98JB02844](https://doi.org/10.1029/98JB02844).

# Offshore seismic monitoring: the Rospo seismic station as a pilot case study for the InSEA project.

A. Mantovani<sup>a</sup>, A. Costanza<sup>a</sup>, G. Fertitta<sup>a</sup>, G. Tusa<sup>a</sup>

<sup>a</sup> *Istituto Nazionale di Geofisica e Vulcanologia, Osservatorio Etneo*

## Introduction

Extending multiparameter monitoring, and in particular seismic one, to offshore areas represents a great challenge from many points of view. Nowadays it has become indispensable for a better understanding of the phenomena affecting the marine environment, as the oceans cover 70 percent of the Earth's surface, and also to provide a better localization of earthquakes along coastal and offshore sectors.

For many years, the Istituto Nazionale di Geofisica e Vulcanologia has been involved in the underwater multiparameter monitoring of the ocean floor (Beranzoli *et al.*, 2000, 2015; D'Anna *et al.*, 2009; Favali *et al.*, 2006a, 2006b; Monna *et al.*, 2005, 2013; Sgroi *et al.*, 2006, 2007, 2019, 2021). Since 2005, the OBS Lab of Gibilmanna (Cefalù, Italy) has been dealing with the technological development of submarine systems, and the on-site specific operations for both deployment and recovery of the scientific instruments.

Recently the InSEA project (detailed description in De Santis *et al.*, 2022), funded by the Italian Ministry of University and Research, aims to increase at national level the network of marine observation and monitoring systems in accordance with EMSO (European Multidisciplinary Seafloor and water column Observatory) ERIC (European Research Infrastructure Consortium) infrastructures in the less developed regions of Southern Italy. The project is developed according to six Objectives of Realization (ORs); in particular, among the activity belonging to the OR3, are listed the increase of the equipment for seafloor seismic monitoring (Ocean Bottom Seismometers - OBS) and the extent of the geophysical network between the Adriatic and Ionian Sea, by deploying submarine multi-parameter monitoring modules within the safety areas of five oil platforms (ca. 200 m away).

An opportunity to study the possible advantages and disadvantages of installing scientific instrumentation in such a prohibitive environmental context is represented by the Rospo seismic station. In May 2018, a Framework Agreement between the Ministry of Economic Development – General Department for the Safety of Mining and Energy (DGS-UNMIG), INGV and Assomineraria, was signed to start a scientific collaboration. Subsequently, DGS-UNMIG, INGV and EDISON Spa (as a member of Assomineraria) signed an Implementing Agreement for research purposes. As a first implementation of the Agreement, one of the conductor pipe (hereinafter c.p. D) of the Rospo Mare C oil platform (RSM-C, middle Adriatic Sea) has been made available for seismic and multiparameter monitoring. The installation of an OBS was concluded in January 2020 and, since February 2020, it belongs to the National Seismic Network (<http://www.gm.ingv.it/index.php/rete->

[sismica-nazionale](#)), whose recorded data are transmitted in real time, through the EDISON network, to the INGV seismic monitoring centre.

### The Rospo Mare C oil platform: arrangement and mechanical behaviour

The RSM-C oil platform (42° 14' 8,365" N, 14° 55' 54,682" E) is located offshore facing the city of Vasto and is part of a group of three platforms interconnected with each other by submarine pipelines. It is characterized by a four-legged reticular structure, about 100 m high from the seabed, while around 80 m are submerged. About 40 m of the c.p. D are buried within the soft sediments of the seafloor, while around 94 m between the seafloor and the sea surface, and other 10 m from the latter to the platform.

The offshore platforms are obviously subjected to several natural forces (winds, sea currents, waves) and anthropogenic ones (*e.g.* oil extraction processes), that excite the vibrational mode shapes of their structures. All these vibration fields can interfere with the seismic data acquisition system, in terms of quality of the recordings, reducing the Signal-to-Noise Ratio (SNR).

To calculate the natural frequencies of the c.p. D, we perform a finite element modal analysis, appropriately constrained, following the method described in Cammalleri and Costanza (2016). For the same purposes, the natural frequencies of other existing platforms, structurally similar to RSM-C, were collected from the literature (Jiammeepreecha *et al.*, 2008; Raheem *et al.*, 2012; Weldelassie, 2014). Furthermore, the frequencies of marine waves and those related to Von Karman's vortices (caused by sea currents flowing around the c.p. D) were considered. All those frequencies are listed in Tab. 1.

[Hz]					
Nat. Freq. of platforms structurally similar to RSM-C					
Nat. Freq. C.p. D	[Jiammeepreecha]	[Raheem]	[Weldelassie, 2014]	Marine waves	Von Karman
0.3	0.8	1.1	0.25	0.005 – 0.15	0.03
0.8	0.8	1.1			0.06
1.5	2	1.4			0.12
2.5		3.6			0.15
3.7		3.6			

Tab 1. Vibration frequencies

### Data acquisition system

The installation of an OBS at the base of the c.p. D of the RSM-C has been logistically possible, with the awareness of disturbances and relatively high noise levels between 0.1 and 10 Hz. As to minimize the influences of such disturbances, and also to ensure a good coupling, we developed a system which allows the sensor self-burying within the pelitic sediments of the seabed. As shown in Fig. 1, two conical caps are attached to the sensor and connected to a hydraulic circuit which conveys a flow of water from the top of the c.p. D to the seabed. A downward jet of water, coming out from below the sensor, digs a hole in the sediments, both ensuring an easier deployment and

recovery of the instrumentation. A dispersing nozzle was also designed to optimize the burying system.

The whole data acquisition system is composed of a broadband seismometer Nanometrics Trillium OBS 120 s and a Guralp DM24 digitizer inside the electronics vessel. A 150 m long marine cable, carrying data and power, connects the vessel to the surface unit. As it can be seen in Fig. 1 (a-c), a custom-made centering disc, made of polyethylene, guarantees the correct positioning of the bundle formed by the cables, rope and pipe above the sensor. It supports the electronic vessel and prevents the bundle from touching the walls of the c.p., as they may transmit mechanical noise to the sensor through the bundle.

The core of the surface unit is a Guralp EAM-U digital acquisition system, hosting a SEEDLink server. The server is accessible from the INGV seismic monitoring center, where a SEEDLink client will continuously receive the seismic data, available in near real-time.

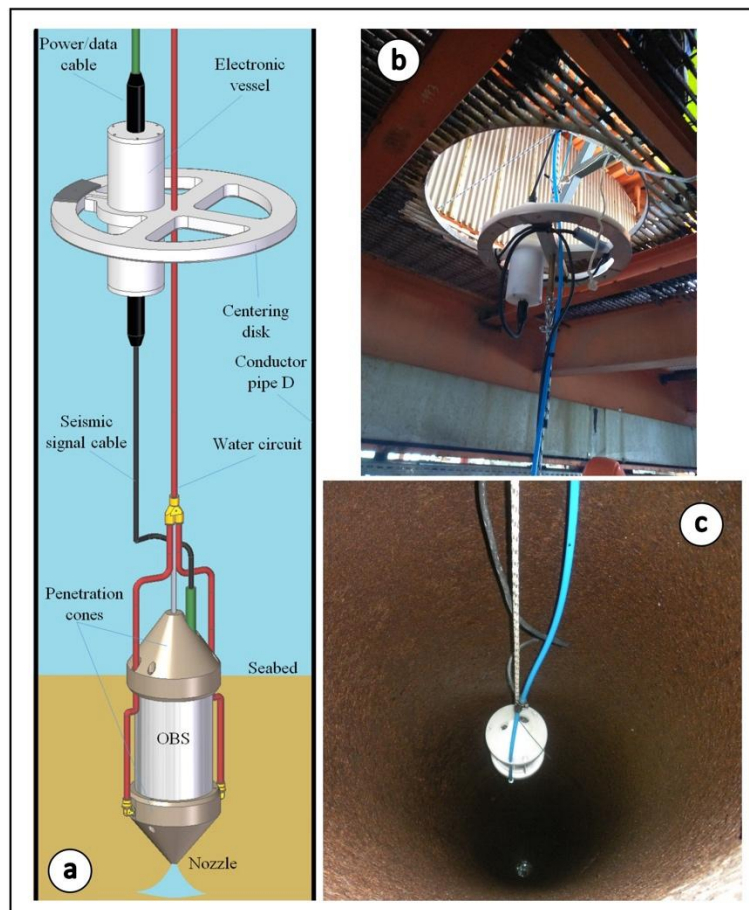


Fig. 1 – Schematic arrangement of the whole instrumentation deposited at the bottom of the c.p. D (a). In (b) and (c) a focus on the centering disc supporting the digitizer.

### Quality evaluation of the recorded signals

As a first step, we collected the signals of the first week of each month, day by day, between March 2020 and October 2023 through the dedicated FDSN Web Services (<https://www.fdsn.org>).

Sample frequency is equal to 100 Hz so, as to investigate the whole range of frequencies of the sensor, we employ a signal windowing of 16.384 samples. We thus calculated the so-called Power Spectral Density (PSD, Fig. 2), the amplitude spectra and the spectral ratio (Nakamura, 1989) (Fig. 3d), as their temporal variability identifies the main noise sources at the recording sites, defines the noise levels of a station and assesses the earthquakes detection capability. Fig. 2 shows the PSDs calculated for the three components and the seasonal ones of the vertical component, for the whole period (308 days analysed). Comparing our results with the NLNM and NHHM reference curves (Peterson, 1993) we observed that the noise spectra levels are generally high and exceed the upper limit for period below 2 s and above 10-20 s. In the microseisms band (0.1-10 s), we observed the typical peaks, the so-called single (SF) and double frequency (DF), as a result of the interaction between atmosphere, sea surface, and seafloor (Webb, 1998).

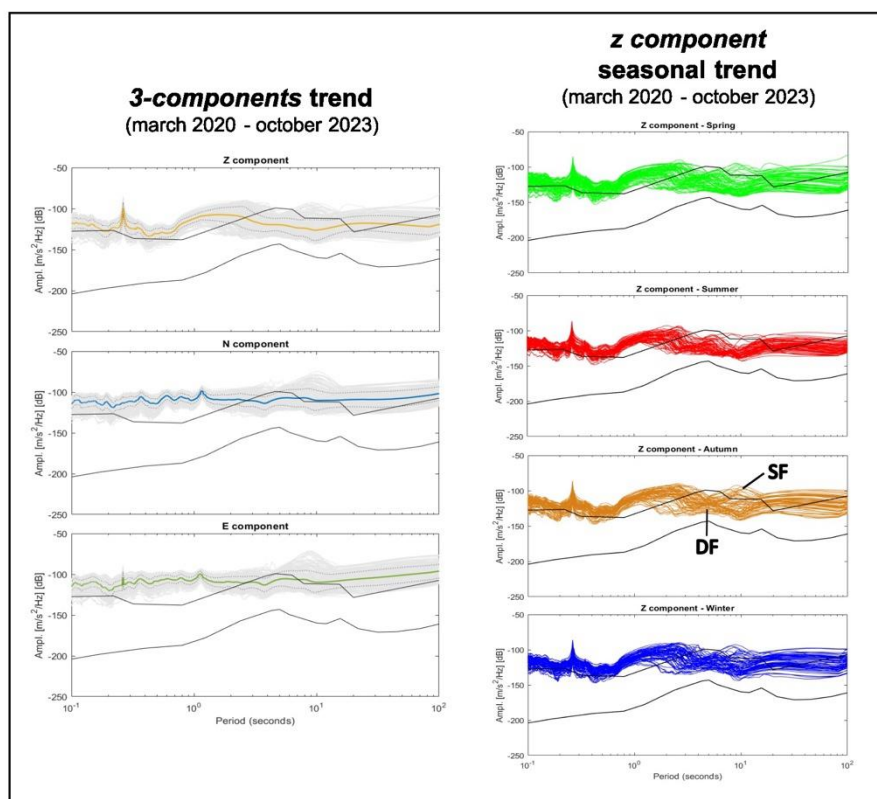


Fig. 2 – Seasonal and whole period PSD's for the three components. All the curves are reported in grey, while the mean one is color-coded. Peterson reference curves in black.

Because it is not always possible to check the arrangement of the instrumentation during the deployment, is fundamental the *a posteriori* establishment of the eventual correction to apply to the horizontal channels signals as to bring them to the conventional Cartesian reference. Among the several approaches known in the literature, we choose that proposed by Doran and Laske (2017) which is based on the measurement of the Rayleigh wave arrival angles. The result highlighted a deviation from north of  $107^\circ$ ; therefore, by applying this correction we observed that the signal is almost constantly polarized towards SSE-NNW (Fig. 3c).

Nowadays this procedure has been automated in MATLAB by the development of an interface we called “on demand” (Fig. 3), which allows a qualitative inspections of the recorded signals in near real-time.

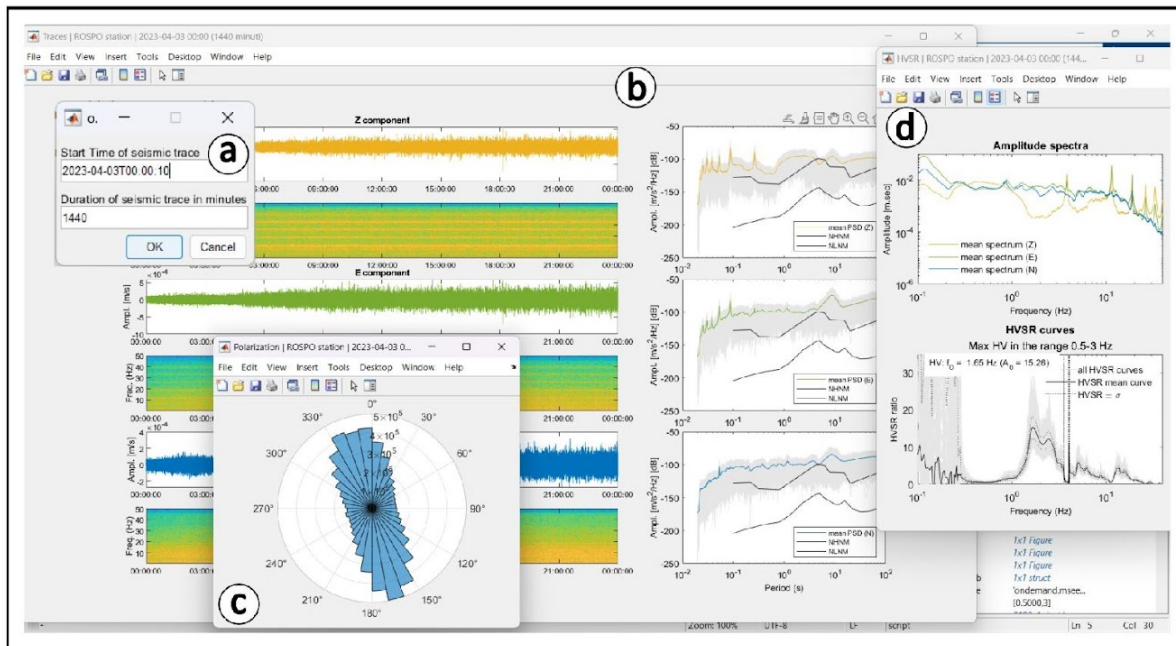


Fig. 3 – “On demand” interface. In (a) the dialog box. In (b) the spectrograms (on the left) and the Power Spectral Density (on the right) for the three components. In (c) the signal polarization polar histogram and in (d) the amplitude spectra (on the top) and the horizontal-to-vertical spectral ratio (on the bottom).

## Conclusions

The OBS Lab of Gibilmanna performed the first installation of a broadband OBS at the bottom of one of the conductor pipes of the Rospo Mare C oil platform. For a preliminary analysis of the signals we developed a semi-automated MATLAB interface, which allow a fast qualitative evaluation. Notwithstanding our results highlighted that the site is noisy, compared to some land-stations, the system has been extensively tested and nowadays is fully functional. Hopefully, our experience and observations could help in exploring the opportunities that such structures may offer to extend the national seismic network to the marine environment, reducing the current seismic gap and thus improving earthquake’s location.

## References

- Beranzoli L., Braun T., Calcara M., Calore D., Campaci R., Coudeville J.-M., De Santis A., Di Mauro D., Etiope G., Favali P., Frugoni F., Fuda J.-L., Gamberi F., Gasparoni F., Gerber H.W., Marani M., Marvaldi J., Millot C., Palangio P., Romeo G. and Smriglio G.; 2000. *GEOSTAR: the first European long term seafloor observatory*, EOS, Trans. Am. Geophys. Un., 81 (5), 45-49.
- Beranzoli L., Cifardini A., Cianchini G., De Caro M., De Santis A., Favali P., Frugoni F., Marinaro G., Monna S., Comntuori C., Qamili E and Sgroi T.; 2015. *A first insight into the Marsili volcanic seamount (Tyrrhenian Sea, Italy): Results from ORION-GEOSTAR3 experiment*. In: SEAFLOOR OBSERVATORIES. Springer Praxis Books. Springer, Berlin, Heidelberg.

- Cammalleri M. and Costanza A.; 2016. *A closed-form solution for natural frequencies of thin-walled cylinders with clamped edges*. International Journal of Mechanical Sciences, 110, pp. 116-126.
- D'Anna G., Mangano G., D'Alessandro A., D'Anna R., Passafiume G., Speciale S. and Amato A.; 2009. *The new INGV OBS/H*. Quaderni di Geofisica, 2009, N° 65.
- Doran A. K. and Laske G.; 2017. *Ocean-Bottom Seismometer Instrument Orientations via Automated Rayleigh-Wave Arrival-Angle Measurements*. BSSA, Vol. 107, No. 2, pp. 691–708
- De Santis A., Chiappini M., Marinaro G., Guardato S., Conversano F., D'Anna G., Di Mauro D., Cardin V., Carluccio R., Rende S.F., Giordano R., Rossi L., Simeone F., Giacomozzi E., Fertitta G., Costanza A., Donnarumma G.P., Riccio R., Siena G. and Civitaresse G.; 2022. *InSEA Project: Initiatives in Supporting the Consolidation and Enhancement of the EMSO Infrastructure and Related Activities*. Front. Mar. Sci. 9:846701.
- Favali P., Beranzoli L., D'Anna G., Gasparoni F., Marvaldi J., Clauss G., Gerber H.W., Nicot M., Marani M.P., Gamberi F., Millot C. and Flueh E.R.; 2006a. *A fleet of multiparameter observatories for geophysical and environmental monitoring at seafloor*, Ann. Geophys., 49, 2/3, 659-680.
- Favali P., Beranzoli L., D'Anna G., Gasparoni F. and Gerber H.W.; 2006b. *NEMO-SN1 The 1st "Real-Time" Seafloor Observatory of ESONET*, Nuclear Instruments and Methods in Physics Research Section A: Accelerators, Spectrometers, Detectors and Associated Equipment, 567/2, 462-467.
- Jiammeepreecha W., Chucheepsakul S. and Kantiyawichai K.; 2008. *Dynamic Analysis of Offshore Structures in the Gulf of Thailand by Using Abaqus Program*. In: Conference Paper, Conference: Proceedings of the 13th National Conference on Civil Engineering, At Chonburi, Thailand, May 2008.
- Monna S., Frugoni F., Montuori C., Beranzoli L., Favali P.; 2005. *High quality seismological recordings from the SN-1 deep seafloor observatory in the Mt. Etna region*. Geophys. Res. Lett., 32, L07303.
- Monna S., SgROI T. and Dahm T.; 2013. *New insights on volcanic and tectonic structures of the southern Tyrrhenian (Italy) from marine and land seismic data*. Geochem. Geophys. Geosys., 14, 3703–3719.
- Nakamura Y.; 1989. *A method for dynamic characteristics estimation of subsurface using microtremors on ground surface*. Quarterly report of Railway Technical Research of Institute of Japan, vol. 30, n. 1
- Peterson J.; 1993. *Observation and Modeling of Seismic Background Noise*. US Geological Survey Open File Report; US Geological Survey: Albuquerque, NM, USA; pp. 96-322
- Raheem A.S.E., Aal A.E. M.A., Shafy A.G.A. and Seed A.F.K.; 2012 *Nonlinear Analysis of Offshore Structures Under Wave Loadings*. In: Conference Paper, 15 WCEE, Lisbon.
- SgROI T., Braun T., Dahm, T. and Frugoni, F.; 2006. *An Improved Seismicity Picture of the Southern Tyrrhenian Area by the Use of OBS and Land-Based Network: the TYDE experiment*. Ann. Geophys. 49 (2-3), 801–817.
- SgROI T., Beranzoli L., Di Grazia G., Ursino A. and Favali P.; 2007. *New Observations of Local Seismicity by the SN-1 Seafloor Observatory in the Ionian Sea, Off-Shore Eastern Sicily (Italy)*. Geophys. J. Int. 169 (2), 490–501

Sgroi T., Di Grazia G., and Favali P.; 2019. *Volcanic Tremor of Mt. Etna (Italy) Recorded by NEMO-SN1 Seafloor Observatory: a New Perspective on Volcanic Eruptions Monitoring*. *Geosciences* 9 (3), 115.

Sgroi T., Polonia A., Beranzoli L., Billi A., Bosman A., Costanza A., Cuffaro M., D'Anna G., De Caro M., Di Nezza M., Fertitta G., Frugoni F., Gasperini L., Monna S., Montuori C., Petracchini L., Petricca P., Pinzi S., Ursino A. and Doglioni C.; 2021. *One Year of Seismicity Recorded Through Ocean Bottom Seismometers Illuminates Active Tectonic Structures in the Ionian Sea (Central Mediterranean)*. *Front. Earth Sci.* 9:661311.

Webb S. C.; 1998. *Broadband Seismology and Noise under the Ocean*. *Rev Geophys.* 36, 105-142.

Weldeslassie M.W.; 2014. *Investigation of Which Sea State Yield the Dominating Contribution to Fatigue Accumulation in Offshore Structures*. Master's Thesis.

Corresponding author: [ambra.mantovani@ingv.it](mailto:ambra.mantovani@ingv.it)

# ShellSet – Parallel dynamic neotectonic modelling

J. B. May<sup>1</sup>, P. Bird<sup>2,1</sup>, M. M. C. Carafa<sup>1</sup>

<sup>1</sup> *Istituto Nazionale di Geofisica e Vulcanologia (INGV), Italy*

<sup>2</sup> *Department of Earth, Planetary, and Space Sciences, UCLA, U.S.A*

## Introduction

Recent decades have seen an almost continuous improvement in computing power and techniques; but the general scientific community too often misses out on these improvements. Research institutions, both academic and industrial (public and private), typically provide employees with personal machines for their work, with even the least powerful of these capable of simulations, in serial and parallel, that would have required much more expensive hardware only a decade previously. Unlocking this potential is key to accelerating scientific discovery in every field, particularly where modelling is concerned.

The calculations involved in forward modelling are often time-consuming, perhaps because of the number of calculations e.g., 3D models, or because the underlying model is very large, e.g., a global model. Reducing the time required for these models would improve program usability and lead to faster hypothesis testing. Simply relying on the relentless improvement of computing capabilities to increase program performance is sub-optimal and many existing programs would benefit from relatively small alterations to their source code to fully utilize these improvements.

Here, we present a hybrid parallel program called ShellSet (May et al. 2023). ShellSet improves upon well-known and robust software by simplifying the user interface, removing all prompted user input, and reducing the time to result by employing an MPI (message passing interface) framework to run multiple models in parallel.

## Software

ShellSet (first presented in May et al., 2023) is a combination of three programs which are well known within sections of the geoscientific community, having been developed over recent decades, all of which are available from <http://peterbird.name>.

Briefly, OrbData calculates the crust and mantle-lithosphere thicknesses at each node of a given finite element grid, adding a “lithospheric density anomaly of chemical origin” at each node which is adjusted to achieve isostasy with other nodes. OrbScore calculates the scores for any/all of the six Shells predictions, for relative realism, against supplied real data. The six testable predictions

are: relative velocities of geodetic benchmarks (GV); most-compressive horizontal principal stress directions (SD); long-term fault heave and throw rates (FSR); rates of seafloor spreading (SSR); the distribution of seismicity on the map (SC); and fast-polarization directions of split SKS arrivals (SA).

Shells is where the main forward model calculations occur. Shells uses the thermal and compositional structure of thin spherical shells of planetary lithosphere, together with the physics of quasi-static creeping flow, to predict patterns of velocity, straining, and fault-slip on the surface of a planet. A primary goal of users has been to understand the balance of forces that move the plates while a secondary goal has been to predict fault slip rates and distributed strain rates for seismic hazard estimation.

Shells, OrbData and OrbScore are serial programs except for calls to Intel's Math Kernel Library (MKL) to solve generated linear systems. To improve these programs, we leverage the power of parallel computing to create a single program, ShellSet, which allows multiple models to be tested simultaneously. ShellSet, like Shells before it, uses MKL routines with OpenMP style threads to solve its system of linear equations. While the combination with OrbData and OrbScore moves inter-program interfaces from the user to the program - meaning a simplified user interface and further time savings.

### **ShellSet Vs an existing model**

An example application of ShellSet is shown where we improve upon an existing global model (Earth5-049 in Bird et al., 2008).

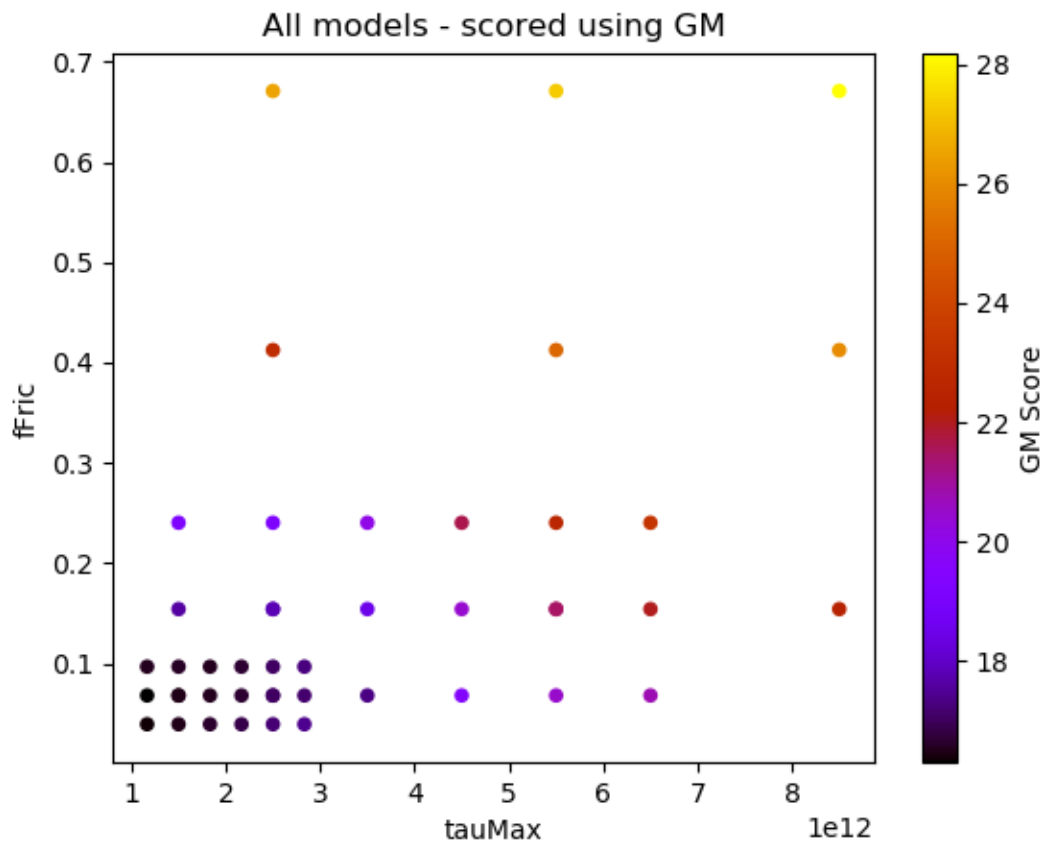


Figure 1: Complete 3-level grid search history of 2D parameter space generated by ShellSet.

We use ShellSet’s grid search model generator to automatically search the defined 2D parameter space for an optimal model. The grid search contains 45 models, generated over 3 levels starting with 9 models before generating a further 9 within the cell of each of the best 2 models at the first and second levels, see Fig. 1.

Among the 45 models we find 8 models with an equal or improved (lower) geometric mean score. These 8 models can be seen in Tab. 1, along with the original score for the best model of Bird 2008 (Earth5-049) and a re-run to account for newer software accuracy (New Earth5-049).

Model ID	fFric	tauMax	Geometric Mean $(\sqrt[4]{SSR*GV*SD*SA})$
Earth5-049	0.10	$2.00 * 10^{12}$	18.10
New Earth5-049	0.10	$2.00 * 10^{12}$	16.58
10	0.07	$1.50 * 10^{12}$	16.50
28	0.04	$1.17 * 10^{12}$	16.34
29	0.07	$1.17 * 10^{12}$	16.29
30	0.10	$1.17 * 10^{12}$	16.55
31	0.04	$1.50 * 10^{12}$	16.49
32	0.07	$1.50 * 10^{12}$	16.50
33	0.10	$1.50 * 10^{12}$	16.58
35	0.07	$1.83 * 10^{12}$	16.55
36	0.10	$1.83 * 10^{12}$	16.56

Table 1: Searched models with improved Geometric mean score when compared to Earth5-049.

### ShellSet performance testing

The performance of ShellSet can be measured in 2 ways. Firstly, Tab. 2 proves that running multiple models in parallel can yield good performance improvement, even on a mid-level machine. It shows the time taken (mm:ss) for a given number of MPI processes to complete a set of models. The bracketed time is the speed up relative to the time taken by 1 process to complete the same number of models. This speed up is plotted in Fig. 2. It is trivial to state that larger machines would offer more significant improvements or the ability to test higher numbers of models and processes.

MPI Processes	Models						
	1	2	4	8	16	32	64
1	3:50	7:47	16:06	32:33	64:26	128:39	262:09
2	X	5:12 (1.50)	10:19 (1.56)	21:13 (1.52)	42:06 (1.53)	84:59 (1.51)	172:33 (1.52)
4	X	X	7:59 (2.02)	15:45 (2.05)	32:05 (2.01)	62:12 (2.07)	125:49 (2.08)
8	X	X	X	15:02 (2.15)	29:35 (2.18)	58:21 (2.21)	113:03 (2.32)
16	X	X	X	X	29:31 (2.18)	57:22 (2.24)	111:15 (2.36)

Table 2: Intel Core i9-12900 CPU at 2.4GHz desktop with 64GB RAM, 16 physical cores (8 performance, 8 efficient) and 24 threads.

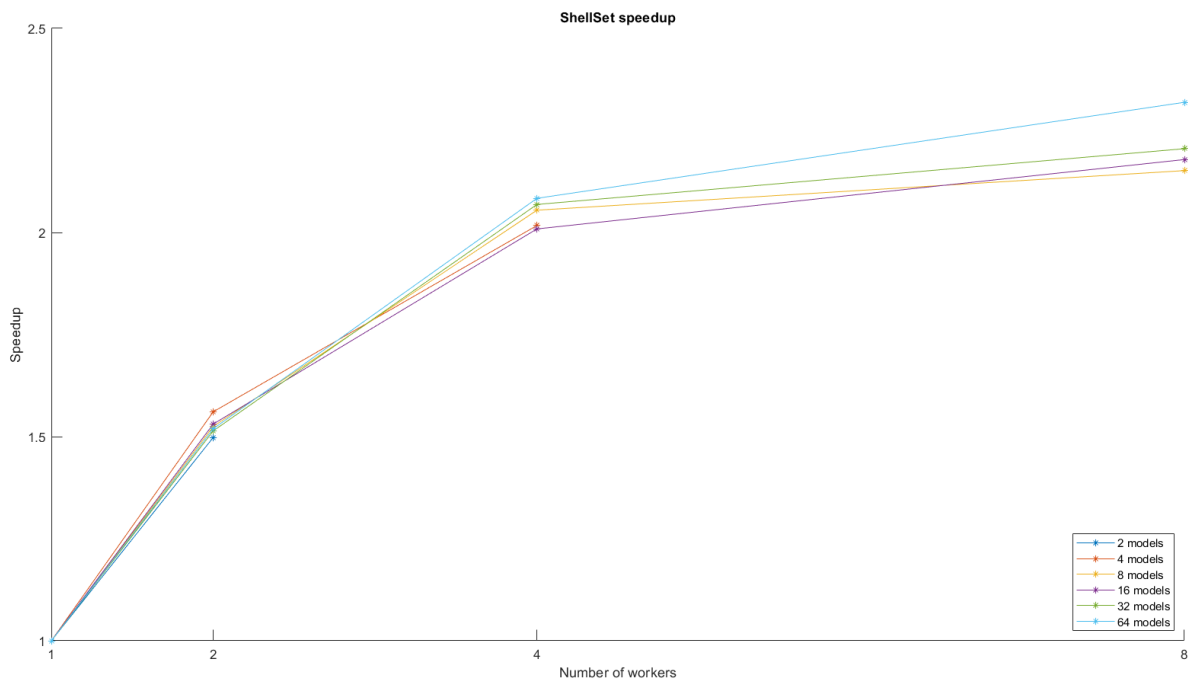


Figure 2: ShellSet speed up performance. The 16 worker speed up results are omitted as they are similar to 8.

Secondly, we know from experience that the simplified user interface and model input options greatly increase the program's performance. The original programs worked in serial (1 model at a time using parallel MKL routines) with the inter-program interfaces handled manually by the user, the newly optimized program removes this requirement on the user by automatically feeding information between the 3 constituent program parts. Not only do these automated connections offer a performance boost but they allow a "start and ignore" treatment of the program, meaning a user can simply begin a test and wait for the result with no further input required.

The ability to utilize parallel computing combined with a simplified user interface, ShellSet also includes a GUI to aid the user in setup, significantly widens the possible user base. This makes ShellSet accessible to anyone from seasoned researchers to master's or even bachelor's degree students whose research time may be limited.

### References

Bird P., Liu Z., and Rucker W.K.; 2008: Stresses that drive the plates from below: Definitions, computational path, model optimization, and error analysis. *Journal of Geophysical Research: Solid Earth*, 113, B11.

May J.B., Bird P., and Carafa M.M.C.; 2023: ShellSet v1.1.0 - Parallel Dynamic Neotectonic Modelling: A case study using Earth5-049 (pre-print). *EGUsphere*, 1-21.

Corresponding author: [jonbryan.may@ingv.it](mailto:jonbryan.may@ingv.it)

# An innovative machine learning algorithm for gravity modelling

C. Messina<sup>1</sup>, L. Bianco<sup>1</sup>, M. Fedi<sup>1</sup>,

<sup>1</sup> *Department of Earth, Environment and Resources Sciences, University of Naples "Federico II", Naples, Italy*

We describe a Machine Learning algorithm for interpretation of gravity data generated by rather complex structures. We choose a Convolutional Neural Network (CNN) with a U-Net architecture. This architectural design of the network has been recently applied in gravity modelling scenarios, in which the training dataset was built introducing strong prior information about the source without obtaining a generalized training set. To overcome this limit we train the network through examples composed by labels constituted by simple elements, here called building blocks, with features being their corresponding gravimetric anomalies. Next to the training we test our method first analysing gravity anomalies produced by simple structures (e.g., prisms, horizontal cylinders), and then with those generated by increasingly complex sources with irregular shapes, such as salt diapirs. We show examples of 2D-3D of real cases. We assume that a gravimetric anomaly can be seen as composed of the constructive interference of anomalies generated by the edges of the source associated to building blocks. Moreover, this method streamlines decision-making and reduces computational efforts involved in assembling a suitable dataset.

Corresponding author: [ciromessina631@yahoo.it](mailto:ciromessina631@yahoo.it)

# A data-driven supervised neural network approach for surface waves inversion: synthetic and field data applications

Felipe Rincón<sup>1</sup>, Sean Berti<sup>1,2</sup>, Mattia Aleardi<sup>1</sup>, Eusebio Stucchi<sup>1</sup>

<sup>1</sup> University of Pisa, <sup>2</sup> University of Florence

## Introduction

In near-surface applications, S-velocity models are commonly obtained through the analysis of the dispersion characteristic of the surface waves. One of the most popular approaches is the multichannel analysis of surface waves (MASW) which is a phase-velocity inversion method (Park et al., 1999). The forward operator involved in the computation of the dispersion curves presents two strong assumptions: a 1D layered model and plane-waves. These limitations strongly affect the capability of the method to account for lateral velocity variations. To overcome these limitations, it is imperative to employ more sophisticated methods such as Full Waveform Inversion (FWI). FWI is an inverse problem that exploits the full information content of the seismic waveforms. Traditionally it is solved through deterministic approaches which seek to find a single best-fit model that explains the observed data. Even though this approach is computationally efficient it heavily relies on a good starting model to reach convergence.

The rapid advancements in algorithms and computing present an unprecedented opportunity for significant progress in seismic inversion, enabling the solution of previously infeasible problems through data-driven approaches. A promising avenue of research involves establishing a direct inverse mapping from observed seismic waveforms to subsurface structures through the training of neural networks using paired data of seismic waveforms and corresponding velocity models (Wu et al., 2018). These approaches seek to leverage the power of deep learning to learn complex relationships between seismic data and subsurface properties, potentially revolutionizing the traditional FWI methodology. However, the efficacy of learning-based methods stems from their ability to leverage vast amounts of high-quality training data, a challenge for seismic methods due to their high costs and confidentiality concerns that limit the accessibility of seismic data. In this study we introduce a novel approach that combines a reparameterization of both the data and model parameters employing Discrete Cosine Transform (DCT) with neural networks to approximate the inverse operator. We tested our method in both synthetic and field data from the InterPACIFIC project (Garofalo et al., 2016). Our objective is to conduct time-effective training to generate S-velocity models from the data. The proposed model could serve as a starting point for a FWI frameworks, helping to mitigate the cycle skipping problem and reduce the number of iterations to reach convergence.

## Methods

We performed our training in DCT-domain as a strategy to reduce the memory storage of the dataset, to enable a flexible matching relation between input and output second dimensions using a versatile number of coefficients, thereby facilitating the application of a reasonable number of geophones, and to reduce the number of model and data parameters during the learning process, leading to accelerate the training. The DCT is a linear orthogonal transformation that decomposes a signal into a combination of cosine functions oscillating at varying frequencies (Ahmed et al., 1974). To construct the Vs model dataset, we carefully selected a set of "base models" representing prevalent geological environments, including features like landslide, sinkholes, stratification, layer displacements, and landfills. Subsequently, we generated multivariate normal random models by utilizing the mean values of these base models and five distinct covariance matrices. To compute the seismograms, we utilized SOFI2D algorithm, an elastic forward solver proposed by Bohlen (2002). We kept fixed the hyperparameters of the forward computation guaranteeing that the CFL conditions were satisfied, and for all the computations we employed a Ricker wavelet of 15 Hz. In this way we generated 9500 Vs-model and data as the training dataset, with an additional of 500 for validation.

Figure 1a depicts a schematic representation of the neural network, showcasing the transformation of both input seismograms and the output velocity model into the DCT domain. The architecture comprises an encoding-decoding stage, employing max-pooling and transposed convolution, respectively. The number of channels progressively increases from 64 to 1024, with each stage duplicating its number until reaching a latent space, before decoding the information into the truncated DCT model dimension. Figure 1b displays the training and validation monitoring curves. Validation is conducted on 500 seismograms and velocity models pairs that were not utilized during the training process. The Mean Square Error (MSE) Loss function is utilized for monitoring the training (blue curve), alongside the L2-norm of the predicted data computed from the proposed model, serving as the validation metric (orange curve). Note that with an increase in the number of epochs, both the MSE and L2-norm decrease, indicating successful learning improvement by the network. However, after 1300 epochs (black-dashed curve), the loss function reached convergence, and the L2-norm becomes unstable, suggesting a potential occurrence of overfitting during training.

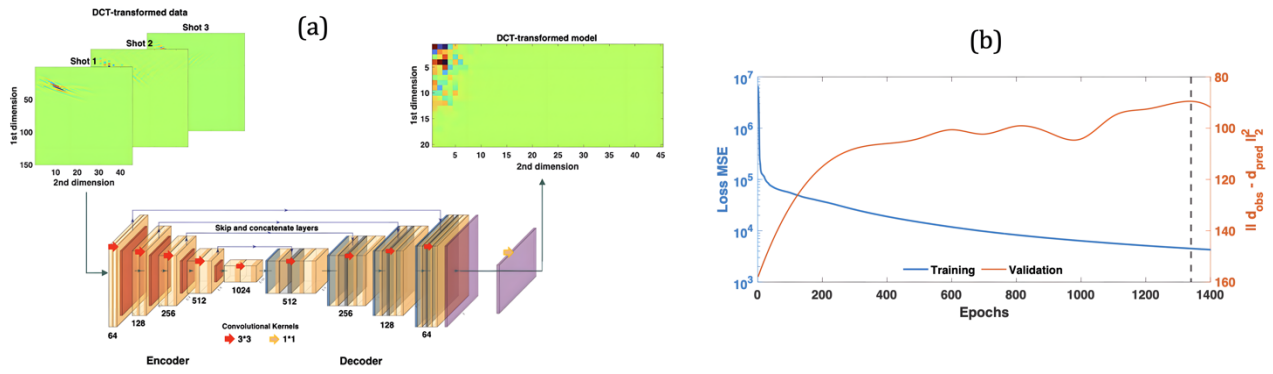


Fig. 1 – (a) Scheme of the network architecture for a 3-shots acquisition array. The input data and output velocity models are in DCT-domain. (b) Training and validation are represented by the blue and orange curves, respectively. The analysis is confined to the initial 1300 epochs, as indicated by the black-dashed curve, until which convergence is achieved.

### Results

To illustrate the capability of the trained network to propose Vs-models, it is presented below an example for synthetic and field data. The field data was taken from the InterPACIFIC project which also includes Vs measurements in boreholes located at 10 m of the acquisition array. The borehole data was utilized to validate the obtained results. The synthetic data was constructed using the same array of the field data. The acquisition setting consists of 48 receivers separated 1 meter, and 3 sources (two off-end and one middle shots).

**Synthetic data example:** Figure 2 shows the network’s prediction on the synthetic example. The data was created using the same Ricker wavelet as the training dataset. In Figure 2a it is shown the true and predicted velocity model. Note that the trained network accurately predicts both the main features and magnitudes of the true velocity model. In Figure 2b, a comparison between the observed and predicted data is presented. It is noteworthy that the data exhibit a perfect match and do not show any signs of cycle-skipping.

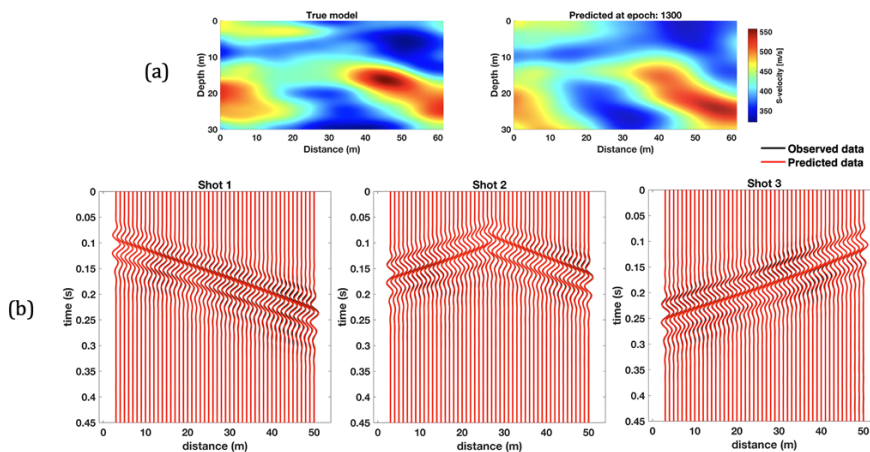


Fig. 2 – Synthetic example: (a) S-velocity model predicted using the NN at epoch 1300. (b) Observed and predicted data comparison.

**InterPACIFIC data example:** Figure 3 presents the network's prediction on a real dataset. To align the data with the training simulations, a low-pass filter with a cutoff frequency of 30 Hz was applied. The predicted data was computed using an estimated wavelet derived from the observed data after filtering. In Figure 3a, the predicted model is depicted alongside a mean 1D Vs-model profile (black curve) derived from multiple borehole measurements available from the InterPACIFIC project. Note that a significant high-low-high velocity contrast is observed in the borehole between 15-18 meters depth, aligning well with the corresponding features in the predicted model at that position. The network proposes a layered model with a velocity range consistent with those obtained from the borehole measurements. In Figure 3b it is shown the comparison between observed and predicted data. It is noteworthy that the data exhibits excellent agreement, except for traces located between the distances 30-40 meters. Despite this, the data does not present cycle-skipping, meaning that the predicted model is a very good starting model proposal for an FWI framework.

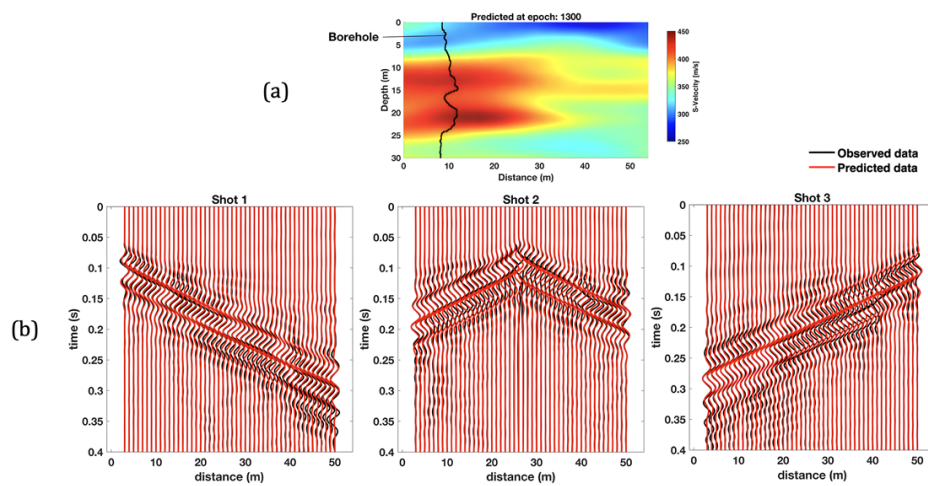


Fig. 3 – Field data example: (a) S-velocity model predicted using the NN at epoch 1300. (b) Observed and predicted data comparison.

## Conclusions

We introduced a time-efficient neural network training in DCT-domain. The construction of the training and validation datasets was completed in parallel within 3.8 hours. The training process to reach epoch 1300 took 7.6 hours, and the required time to propose a model using the trained network and conduct the inverse DCT is 0.2 seconds. All these algorithms were performed in a computer system powered by a 12th Gen Intel(R) Core (TM) i9-12900KF equipped with NVIDIA GeForce RTX 3080 Ti graphics card and the system runs with CUDA Version: 11.8.

The use of DCT compression is an optimal strategy in neural network training, offering significant advantages. This approach notably reduces the memory requirement from 21 to 1.2 gigabytes, resulting in a 94% reduction in memory usage. Moreover, the computational cost during training is decreased by 74% with respect a full-domain training. Finally, the DCT compression enables

practical training with a reasonable number of geophones since the number of coefficients in the DCT can be readily adjusted to align with both the data and model requirements.

We demonstrated the trained network's capability in generating data-driven S-velocity model proposals with minimal data misfits between observed and predicted data. Modifications in array settings and source characteristics may necessitate retraining the network, which, under similar hyperparameters as presented in this work, requires approximately 11.4 effective hours. The proposed S-velocity model can serve as a starting model for FWI frameworks, offering the potential to reduce computational costs and address the cycle-skipping issue.

### **Acknowledgements**

We express our gratitude to Nicola Bienati for providing valuable assistance and insightful comments that significantly enhanced the quality of this work.

### **References**

- Ahmed, N., Natarajan, T., & Rao, K. R. (1974). Discrete cosine transform. *IEEE transactions on Computers*, 100(1), 90-93.
- Bohlen, T. (2002). Parallel 3-D viscoelastic finite difference seismic modelling. *Computers & Geosciences*, 28(8), 887-899.
- Garofalo, F., Foti, S., Hollender, F., Bard, P. Y., Cornou, C., Cox, B. R., ... & Yamanaka, H. (2016). InterPACIFIC project: Comparison of invasive and non-invasive methods for seismic site characterization. Part I: Intra-comparison of surface wave methods. *Soil Dynamics and Earthquake Engineering*, 82, 222-240.
- Moghadas, D., & Vrugt, J. A. (2019). The influence of geostatistical prior modeling on the solution of DCT-based Bayesian inversion: A case study from Chicken Creek catchment. *Remote Sensing*, 11(13), 1549.
- Park, C. B., Miller, R. D., & Xia, J. (1999). Multichannel analysis of surface waves. *Geophysics*, 64(3), 800-808.
- Wu, X., Shi, Y., Fomel, S., & Liang, L. (2018, October). Convolutional neural networks for fault interpretation in seismic images. In *SEG International Exposition and Annual Meeting* (pp. SEG-2018). SEG.

Corresponding author: felipe.rincon@phd.unipi.it

# Filling active seismic null space with LSTM

G. Roncoroni<sup>1</sup>, I. Deiana<sup>2</sup>, E. Forte<sup>1</sup>, M. Pipan<sup>1</sup>

<sup>1</sup> *University of Trieste, Italy*

<sup>2</sup> *Stanford University, California, USA*

## Introduction

Post-stack seismic data analysis plays a crucial role in understanding subsurface structures and petrophysical properties, often associated with a peculiar low or high frequency behaviour. Sinha et al. (2005) highlighted the presence of low-frequency shadows in association with hydrocarbon reservoirs, emphasising the significance of low-frequency information in post-stack seismic data for reservoir characterization. Moreover, the application of discrete wavelet transform-based multi-resolution analysis for spectral enhancement in post-stack seismic data was discussed by Camacho-Ramírez et al., 2016, which remarked on the role of frequency analysis in characterising heavy oil reservoirs. Reiser & Bird (2016) presented case studies of broadband quantitative interpretation, emphasising the utilisation of frequency-related information for improved target delineation and estimation of reservoir properties from post-stack seismic data. Additionally, Du et al. (2016) addressed the challenges of low signal-to-noise ratio and the importance of considering the main frequency and signal-to-noise ratio of seismic data for thin beds interpretation in post-stack seismic data. Furthermore, Karsli et al. (2006) discussed the application of complex-trace analysis for random-noise suppression and temporal resolution improvement in post-stack seismic data, emphasising the significance of frequency-related analysis for enhancing data quality, while Shi et al. (2009) addressed near-surface absorption compensation technology and its application in the Daqing Oilfields, stressing the importance of frequency-related compensation techniques for improving the resolution of post-stack seismic data. Moreover, Chopra et al. (2003) discussed high-frequency restoration of surface seismic data, indicating the relevance of frequency-related restoration techniques for enhancing the resolution of post-stack seismic data. Therefore, post-stack seismic data analysis encompasses various dedicated frequency-related analyses and methodologies, emphasising the significance of low and high-frequency information for reservoir characterization, attribute prediction, noise suppression, and resolution enhancement.

In fact, low and high-frequency extrapolation from active seismic data is essential for various applications such as imaging, reservoir characterization, and monitoring. Classical methods for low-frequency extrapolation involve techniques such as full-waveform inversion (FWI) and autoregressive (AR) spectral extrapolation. FWI with extrapolated low-frequency data has been proposed as an effective method for determining the low-wavenumber components of the model from extrapolated low frequencies (Sun & Demanet, 2020). Additionally, the autoregressive extrapolation method has been utilised to extend the spectral bandwidth of seismic data, enabling

the recovery of missing low and high frequencies for acoustic impedance inversion (Karsli, 2010; Karsli, 2006). In recent years, deep learning approaches have gained attention for low-frequency extrapolation from seismic data. Ovcharenko et al. (2019) and Li & Demanet (2016) have proposed application of deep learning - specifically convolutional neural networks - for low-frequency extrapolation, showing promising results in extrapolating low frequencies from multi-offset seismic data. Furthermore, machine-learning-based data recovery has been suggested for simultaneous deblending, trace reconstruction, and low-frequency extrapolation, indicating the potential of deep learning in addressing multiple challenges in seismic data processing (Nakayama & Blacqui re, 2021). Multi-task learning has been proposed for addressing low-frequency extrapolation and elastic model building from seismic data, showing the potential of integrating classical physics-based methods with deep learning techniques (Ovcharenko et al., 2022). In addition to low-frequency extrapolation, high-frequency extrapolation from seismic data has also been a focus of research. Ovcharenko et al. (2020) emphasised the importance of low frequencies in high-frequency land seismic data due to the elastic nature of the Earth's subsurface, highlighting the significance of low-frequency extrapolation in addressing the challenges associated with high-frequency data inversion. Furthermore, a 1-D phase-tracking method has been proposed for extrapolating low-frequency data based on phases and amplitudes in the observed frequency band, indicating the significance of considering different dimensions for effective extrapolation (Li & Demanet, 2016).

## Methods

We propose a novel 1-D approach based on LSTM (Long Short-Term Memory) Neural Networks (NN) to address the low- and high-frequency gap (i.e. null space) in reflection seismics. We trained two different NNs: one is trained to infer a lower frequency output from a higher frequency signal, from now on called low-frequency model, and another with switched input and output, from now on called high-frequency model, with both the input and output assumed to have maximum phase. The training dataset is generated using a convolutional approach. The data generation process involves creating synthetic noisy seismic traces for training, considering modifications to the classical seismic convolutional model to enhance its generalization to better mimic real seismic data. The NN is trained with a custom loss function that includes both amplitude and frequency components.

The method is easily scalable thanks to the fact that the NN operates without direct consideration of frequency, time length and sampling information, enabling the generation of desired frequency output just by adjusting how the input data is sampled. The NN will undergo the training based on a parameter known as Sample Duration (SD), representing the estimated duration of the source wavelet. We have the flexibility to resample each input signal provided to the network to align with the sample duration exploited in NN training. SD serves as the crucial parameter governing frequency content generation, enabling the network to produce new frequencies in accordance with it. Since it is not always easy to determine SD on field data, we use the second zero of the auto-correlation to make it easier to get and more objective such a parameter. Once we have

trained the NN we can scale every signal to the trained SD and make the inference that will output a signal with half the frequency, for the Low-frequency model and one with a double central frequency, for the High-frequency model. Thanks to the constraints given by the custom loss function with the frequency counterpart taken into account, we are able to further generalize the results to other frequencies just by applying a Scaling Factor (SF), i.e. a factor applied to the SD term that multiplies the number of samples in the output. This feature allows us to infer quite easily different frequency predictions. In Figure 1 we plot some of these predictions with varying SF: low-frequency model in Figure 1A where the input SD is divided by the SF and high-frequency model, in Figure 1B, where the SD is multiplied by the SF. The input in both of these results is a frequency filtered version of the Viking Graben Line 12 (Keys and Foster, 1998), filtered with a band-pass filter at 6-20Hz.

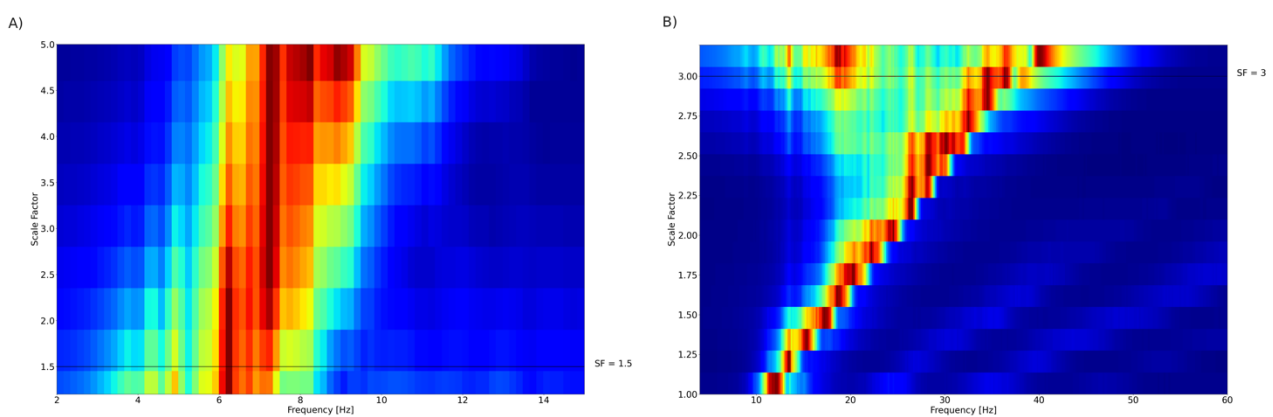


Figure 1: Low (A) and High (B) frequency inference of the Viking Graben Line 12 on the x-axis frequency, and on the y-axis the Scaling Factor. The solid line in A and B marks the chosen frequency that will be used in the next section.

## Results and Discussion

### Low Frequency inference

Results of the application of the methodology are shown in Figure 2. We moved the central frequency from 14Hz to 8Hz, as shown in the amplitude-frequency plot in Figure 2C. If we compare the input (Figure 2A) and the prediction (Figure 2B), it is clear that, as expected from the low frequency counterpart, more importance is given to main reflectors, e.g. horizontal reflector at 2s in the data. We can furthermore appreciate that amplitude is preserved as expected and interference is properly predicted, e.g. in the wedge around 1s in the first 750m .

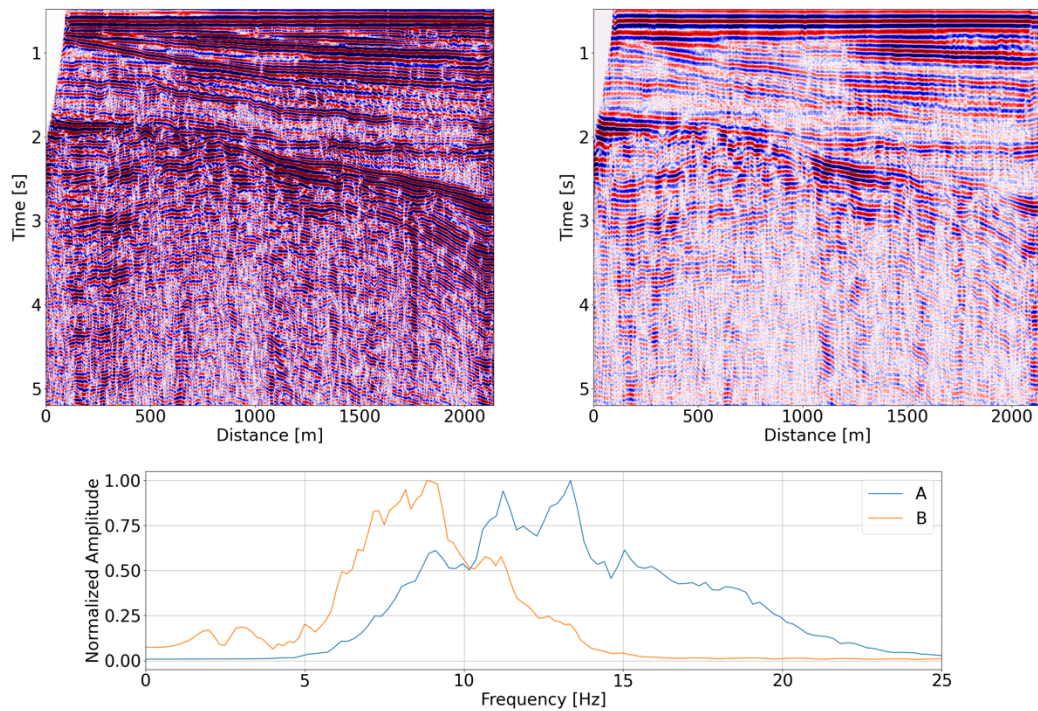


Figure 2: Low frequency inference on a section of the Viking Graben dataset: A represents the input data, B the low-frequency version and C the amplitude spectra of the seismic line depicted in A (blue)- and in B (orange).

### High Frequency inference

For the High-Frequency model, the data shown in Figure 1B is depicted in Figure 3. Since the data had the predicted range of frequency in the raw data, we take now into account 2 different data: Figure 3A is the NN input with central frequency of 14Hz, as used in Figure 2, while in Figure 3C we show the reference data, i.e. the raw data after a 10-40Hz band-pass filter.

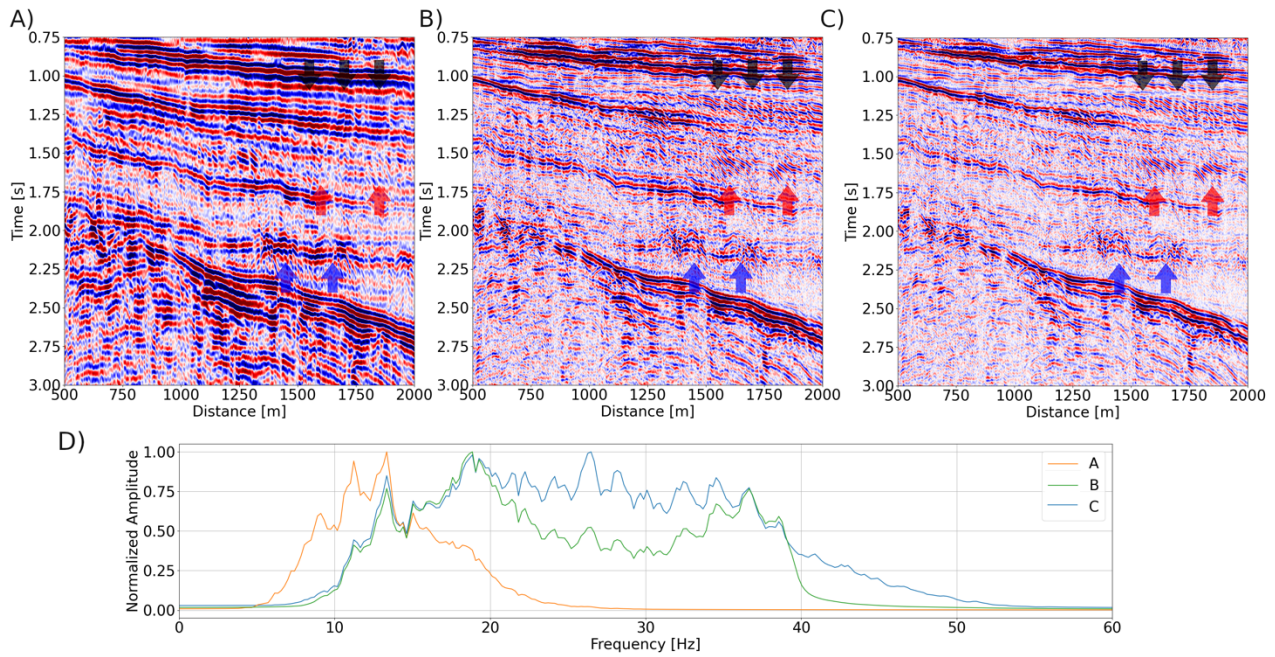


Figure 3: High frequency inference on a section of the Viking Graben dataset: A represents the low-filtered data, the same used in Figure 2A, B is the high frequency inference, and C represents the high frequency reference data. The amplitude spectra of the seismic line depicted in A (Orange), in B (Green), and C (Blue) are reported in D.

Thanks to this, we can make a proper comparison between the input (Figure 3A), the prediction (Figure 3B) and the reference data (Figure 3C). If we focus on the strongly dipping reflector marked with black and red arrows, we can see that while the prediction matches pretty well the reference, this feature was not visible (black arrow) or barely visible (red arrow) in the NN input. Further focus should be put on the diffraction patterns pointed out with the blue arrows: while the match is very good between NN predictions and reference data (i.e. Figure 3B and C), hyperbolas are difficult to be interpreted in the input lower frequency data (i.e. Figure 3A).

In order to further evaluate the results of the two models, we focus on the area from 120-1250m and from 0.6-1.3s (see e.g. Figure 2A). This area is very interesting because it images a typical wedge structure. In Figure 4 we present a wiggle plot of the input (Figure 4A) and the high-frequency inference (Figure 4B).

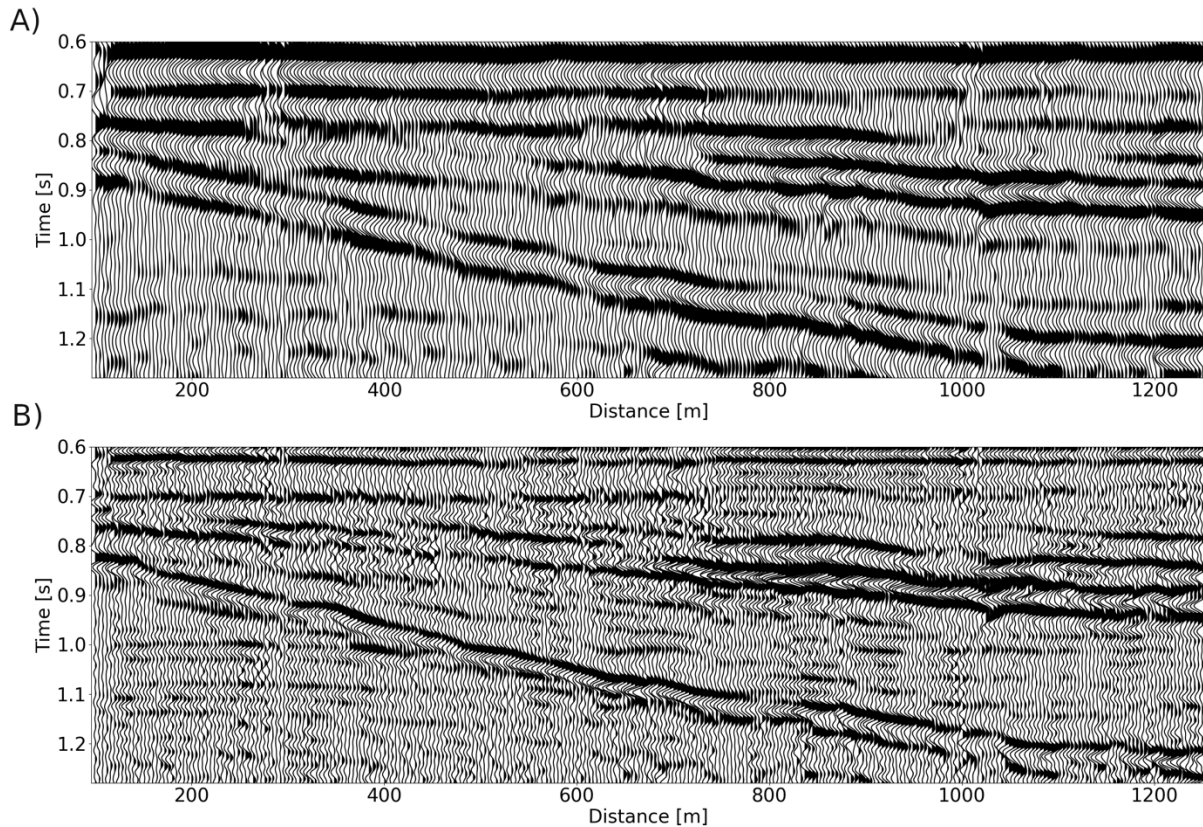


Figure 4: Wiggle plot of the area between 0.6s-1.3s and 120m-1250m of the Viking Graben dataset, focusing on a wedge structure. The input seismic line is shown in A, while the high frequency prediction of the same area is depicted in B.

In Figure 4B, the prompt detection of coherent signals is evident, notably horizontal reflectors beneath and within the wedge structure. Despite the limited leftward extent of the section, there is a remarkable improvement in vertical resolution, potentially enabling the identification of pinch-out structures.

## Conclusions

We introduce a novel 1-D approach based on LSTM (Long Short-Term Memory) Neural Networks for addressing the low- and high-frequency gaps in seismic signal processing. The proposed method involves training two distinct neural networks: a low-frequency model, trained to infer lower frequency output from higher frequency signals, and a high-frequency model, trained with reversed input and output.

The method's scalability is assured thanks to its ability to operate without direct consideration of the frequency components, time length, and sampling information. The NN is trained with a custom loss function that incorporates both amplitude and frequency components. A crucial parameter known as Sample Duration (SD) governs the frequency content generation during training, providing flexibility for adjusting input data sampling and, consequently, the generated frequency output. The method's adaptability is demonstrated by rescaling signals to the trained

SD, allowing the inference of different frequencies through the application of a dedicated Scaling Factor (SF).

The results illustrate the effectiveness of the proposed approach in both low and high-frequency inferences using exemplary seismic data from the Viking Graben Line 12. The low-frequency model successfully shifts the central frequency from 14Hz to 8Hz while preserving amplitude and accurately predicting signal interference. The high-frequency model demonstrates reliable inference when compared to reference data the application of a band-pass filter between 10-40Hz, revealing a better detectability of different features, such as dipping reflectors and diffraction patterns, that were challenging to interpret in the lower frequency input data, while are confirmed by the reference data.

Overall, the proposed LSTM Neural Network-based approach proves to be a promising solution for addressing frequency gaps in seismic signal processing, offering high adaptability, scalability, and enhanced predictive capabilities for both low- and high-frequency components predictions.

## References

- Camacho-Ramírez, E., González-Flores, E., & Campos-Enriquez, J. (2016). Discrete wavelet transform-based multiresolution analysis and spectral enhancement to characterize heavy oil reservoirs in the southern gulf of Mexico region. *Interpretation*, 4(4), T497-T505. <https://doi.org/10.1190/int-2015-0184.1>
- Chopra, S., Alexeev, V., & Sudhakar, V. (2003). High-frequency restoration of surface seismic data. *The Leading Edge*, 22(8), 730-738. <https://doi.org/10.1190/1.1605071>
- Du, W., Xin, P., Wang, P., & Sun, Y. (2016). Multiple-track ant body attribute extraction method improved. <https://doi.org/10.2991/iceeg-16.2016.72>
- Guo, J. and Wang, Y. (2004). Recovery of a target reflection underneath coal seams. *Journal of Geophysics and Engineering*, 1(1), 46-50. <https://doi.org/10.1088/1742-2132/1/1/005>
- Karsli, H. (2006). Further improvement of temporal resolution of seismic data by autoregressive (ar) spectral extrapolation. *Journal of Applied Geophysics*, 59(4), 324-336. <https://doi.org/10.1016/j.jappgeo.2005.11.001>
- Karsli, H. (2010). An application of the autoregressive extrapolation technique to enhance deconvolution results: a 2d marine data example. *Geophysical Prospecting*, 59(1), 56-65. <https://doi.org/10.1111/j.1365-2478.2010.00895.x>
- Karsli, H., Dondurur, D., & Çifçi, G. (2006). Application of complex-trace analysis to seismic data for random-noise suppression and temporal resolution improvement. *Geophysics*, 71(3), V79-V86. <https://doi.org/10.1190/1.2196875>
- Li, Y. and Demanet, L. (2016). Full-waveform inversion with extrapolated low-frequency data. *Geophysics*, 81(6), R339-R348. <https://doi.org/10.1190/geo2016-0038.1>
- Nakayama, S. and Blacquièrè, G. (2021). Machine-learning-based data recovery and its contribution to seismic acquisition: simultaneous application of deblending, trace reconstruction, and low-frequency extrapolation. *Geophysics*, 86(2), P13-P24. <https://doi.org/10.1190/geo2020-0303.1>

Ovcharenko, O., Kazei, V., Alkhalifah, T., & Peter, D. (2022). Multi-task learning for low-frequency extrapolation and elastic model building from seismic data. *IEEE Transactions on Geoscience and Remote Sensing*, 60, 1-17. <https://doi.org/10.1109/tgrs.2022.3185794>

Ovcharenko, O., Kazei, V., Kalita, M., Peter, D., & Alkhalifah, T. (2019). Deep learning for low-frequency extrapolation from multioffset seismic data. *Geophysics*, 84(6), R989-R1001. <https://doi.org/10.1190/geo2018-0884.1>

Ovcharenko, O., Kazei, V., Plotnitskiy, P., Peter, D., Silvestrov, I., Bakulin, A., ... & Alkhalifah, T. (2020). Extrapolating low-frequency prestack land data with deep learning.. <https://doi.org/10.1190/segam2020-3427522.1>

Reiser, C. and Bird, T. (2016). Advances in broadband quantitative interpretation.. <https://doi.org/10.1190/segam2016-13818140.1>

Shi, Z., Tian, G., Wang, B., & Chen, S. (2009). Near-surface absorption compensation technology and its application in the daqing oilfields. *Applied Geophysics*, 6(2), 184-191. <https://doi.org/10.1007/s11770-009-0019-9>

Sinha, S., Routh, P., Anno, P., & Castagna, J. (2005). Spectral decomposition of seismic data with continuous-wavelet transform. *Geophysics*, 70(6), P19-P25. <https://doi.org/10.1190/1.2127113>

Sun, H. and Demanet, L. (2020). Extrapolated full-waveform inversion with deep learning. *Geophysics*, 85(3), R275-R288. <https://doi.org/10.1190/geo2019-0195.1>

Robert G. Keys and Douglas J. Foster, (1998), "1. A Data Set for Evaluating and Comparing Seismic Inversion Methods," *Open File Publications* : 1-12. <https://doi.org/10.1190/1.9781560802082.ch1>

Corresponding author: [groncoroni@units.it](mailto:groncoroni@units.it)

# Modelling temperature effect in time-lapse DC monitoring experiments through inversion of thermal diffusivity

A. Signora<sup>1</sup>, G. Fiandaca<sup>1</sup>

<sup>1</sup> *The EEM Team for Hydro & eXploration Dep. Of Earth Sciences A. Desio, Università degli Studi di Milano, Via Botticelli 23, Milano (Italy)*

## 1. Motivation

In the recent years, time-lapse surveys have been performed widely to monitor, for instance, hydrogeological tracer experiments (Cassiani et al., 2006), groundwater watershed characterization (Miller et al., 2008; Deiana et al., 2018), seasonal variations (Hiblich et al., 2011; Musgrave and Binley 2011), landslide behaviour and evolution (Cassiani et al., 2009, Wilkinson et al., 2010), and so on. One of the main concerns, when resistivity surveys are performed, is to be sure to impute the variations to the right phenomena, distinguishing the electrical changes of interest from all the others, which are assumable as noise. Temperature variations might represent the main noise source in the time-lapse conductivity surveys since temperature has a strong impact on the resistivity parameters, hence the inversion results. For example, seasonal temperature trends could mask the conductivity variations, and thus lead to misleading interpretations, up to the depths from the surface that can be reached by external fluctuations. Haley et al. (2007; 2009; 2010) have pointed out the importance of considering the temperature variations in time-lapse geoelectrical surveys, including in the inversion procedure a correction for this effect. In this study we intend to disentangle the temperature effect from resistivity variations inverting for the thermal diffusivity of the medium in a simultaneous time-lapse inversion that does not require direct temperature measurements below ground, both on a synthetic dataset and on-field experiments.

## 2. Inversion scheme

The temperature effect on electrical resistivity is modelled through the equation proposed by Haley (2007):

$$\sigma_T = (1 + m(T - T_{25}))\sigma_{25} \quad (1)$$

where:

- i)  $\sigma_T$  and  $T$  are effective electrical conductivity and temperature.
- i)  $\sigma_{25}$  is the reference conductivity of the material at 25°degrees.
- ii)  $T_{25}$  is the conventional temperature of 25 °C.
- iii)  $m$  is the fractional change in electrical conductivity per degree Celsius.

The temperature is defined in the entire medium solving for the heat equation:

$$\frac{\partial T}{\partial t} = k \frac{\partial^2 T}{\partial z^2} \quad (2)$$

Where, as depicted in Fig. 1, the temperature at the bottom of the model is considered constant, while the surface temperature varies seasonally. For any given thermal diffusivity  $k$ , the temperature can be estimated through the numerical solution of eq. 2 at each time instant and each depth.

Time-lapse 2D DC data are then inverted simultaneously in EEMverter (Fiandaca et al., 2024), using as model space the electrical resistivity at 25 °C in each inversion cell of all time-lapse models and a unique thermal diffusivity value  $k$  for the entire 2D profile. The sensitivity on the thermal diffusivity is retrieved enforcing time-lapse constraints between all time-lapse models, which favour the inversion models that minimize variations through the correct evaluation of the temperature effect. The asymmetric generalized minimum gradient support (AGMS) introduced by Fiandaca et al. (2015) has been used for time-lapse constraints.

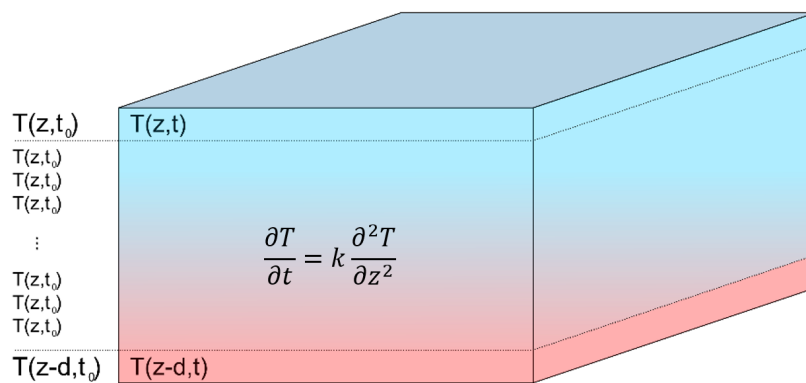


Figure 1. Schematization of the heat flux equation solved for the model discretization. Surface and bottom temperatures of the model need to be fixed as boundary condition within this inversion scheme.

### 3. Synthetic simulation and fieldwork case study

Synthetic simulations have been performed mimicking the seasonal variability of subsoil temperature caused by a homogeneous thermal diffusivity, constant temperature at depth and seasonal-varying surface temperature. On top of the temperature-induced changes in resistivity, a growing plume had been modelled, with 75-100 Ωm 25 °C resistivity in a homogeneous 150 Ωm halfspace. Nine time steps have been modelled, with 50 days of time difference, and all time-steps have been inverted simultaneously with AGMS time-lapse constraints.

Fig. 2 presents the comparison of the models obtained with: i) the standard resistivity inversion; ii) the simultaneous time-lapse inversion with temperature correction. Not only the time-lapse inversion retrieves the correct resistivity distribution, not altered by the temperature effect, but the simulated thermal diffusivity is retrieved correctly by the inversion.

As field example, a 730 days-long real experiment is analyzed. The temperature effect is clearly visible in data space, with apparent resistivity variations clearly correlated with surface temperature (Fig. 3). The survey has been carried out continuously on the rooftop of an MSW landfill, with stainless-steel electrodes whose position never changed for the whole duration of the study. The daily ERT (Electrical Resistivity Tomography) acquisitions were performed through 18 electrodes, spaced 5 meters from each other, with the Wenner-Alpha array configuration and 5 mA alternate currents injected with the frequency of 5 Hz. The result of this survey clearly shows a

sinusoidal fluctuation of the apparent resistivity values during the time and with decreasing magnitude with depth (Fig. 3, upper panels). This decreasing fluctuation points out the effect of the temperature variation on the external portions of the landfill, which vanish increasing the depth of analysis, as evident when comparing the apparent resistivity values and the temperature measured at the site (Fig 3, bottom panels). The deeper portions of the landfill, despite the presence of more noise measurements, show more stable apparent resistivity values through time, therefore less effect of the atmospheric temperature trends. Time-lapse inversions with modelling of temperature effect show much smaller resistivity variations throughout the entire monitoring, showing the improvement of the time-lapse scheme proposed in this study.

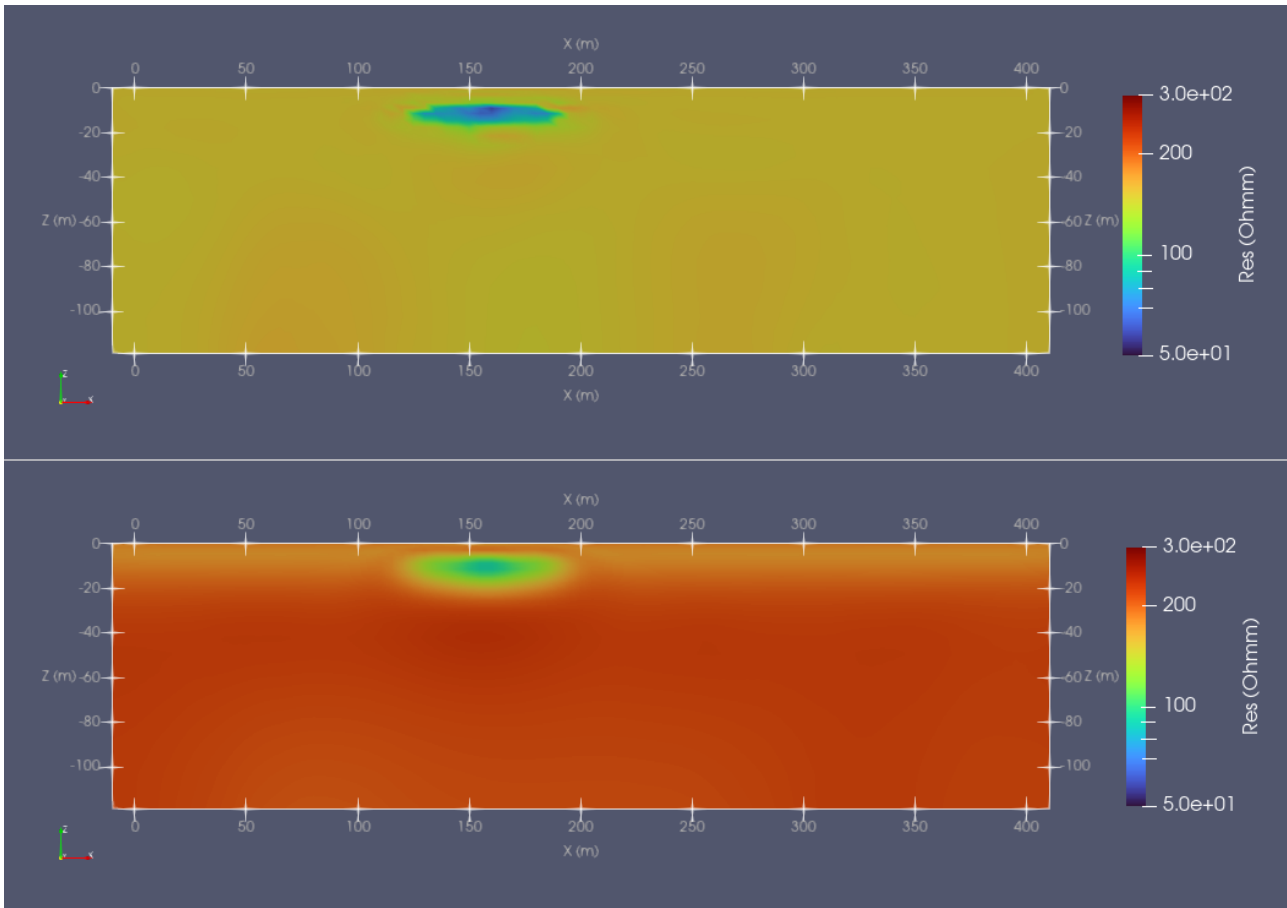


Figure 2. Comparison of standard resistivity inversion (bottom panel) and time-lapse inversion with modelling of thermal diffusivity (top panel).

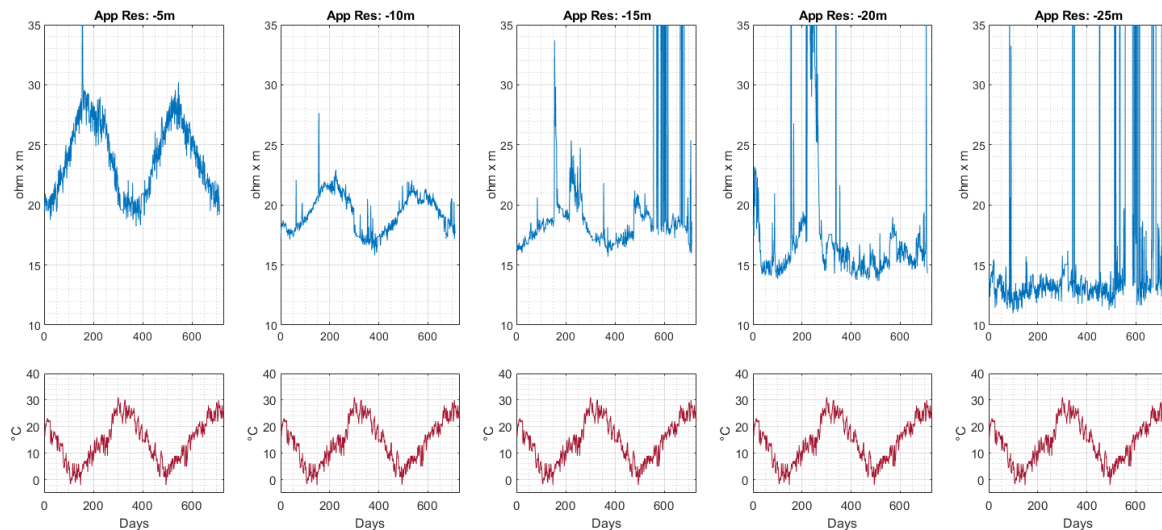


Figure 3. Fluctuation of apparent resistivity recorded within the body waste (blue lines) with different depths during the 740 day-long survey. The red lines in the below graphs represent the mean value of temperature for each survey day.

## 4. Conclusions

In this study a new time-lapse inversion scheme for modelling temperature effect in DC monitoring experiments is presented. The modelling scheme estimates the thermal diffusivity of the subsoil through the simultaneous inversion of time-lapse data, without the need of a direct measurement of the subsoil temperature. Both synthetic test and analysis of real data, acquired in a 730 days long monitoring experiment on an MSW landfill, show the potential of this new inversion scheme, which enable to disentangle temperature effects from resistivity variations induced by changes, for instance, of the groundwater conductivity.

## Acknowledgments

We acknowledge Geo.Ti.La for the data provision. This study is funded by the project HydroGeosITe financed by A2A Ciclo Idrico.

## References

- Cassiani, G., 2009. Monitoring the hydrologic behaviour of a mountain slope via time-lapse electrical resistivity tomography. *Near Surface Geophysics - NEAR SURF GEOPHYS.*
- Cassiani, G., Bruno, V., Villa, A., Fusi, N., Binley, A., 2006. A saline trace test monitored via time-lapse surface electrical resistivity tomography. *Journal of Applied Geophysics* 59, 244–259. <https://doi.org/10.1016/j.jappgeo.2005.10.007>
- Deiana, R., Cassiani, G., Kemna, A., Villa, A., Bruno, V., Bagliani, A., 2007. An experiment of non-invasive characterization of the vadose zone via water injection and cross-hole time-lapse geophysical monitoring. *Near Surface Geophysics.*

- Fiandaca, G., Doetsch, J., Vignoli, G., Auken, E., 2015. Generalized focusing of time-lapse changes with applications to direct current and time-domain induced polarization inversions. *Geophys J Int* 203, 1101–1112. <https://doi.org/10.1093/gji/ggv350>
- Fiandaca, G., Zhang, B., Chen, J., Signora, A., Dauti, F., Galli, S., Sullivan, N.A.L., Bollino, A., Viezzoli, A., 2024. EEMverter, a new 1D/2D/3D inversion tool for Electric and Electromagnetic data with focus on Induced Polarization. GNGTS 2024, 13-16 February 2024, Ferrara, Italy.
- Hayley, K., Bentley, L.R., Gharibi, M., 2009. Time-lapse electrical resistivity monitoring of salt-affected soil and groundwater. *Water Resources Research* 45. <https://doi.org/10.1029/2008WR007616>
- Hayley, K., Bentley, L.R., Gharibi, M., Nightingale, M., 2007. Low temperature dependence of electrical resistivity: Implications for near surface geophysical monitoring. *Geophysical research letters* 34.
- Hayley, K., Bentley, L.R., Pidlisecky, A., 2010. Compensating for temperature variations in time-lapse electrical resistivity difference imaging. *GEOPHYSICS* 75, WA51–WA59. <https://doi.org/10.1190/1.3478208>
- LaBrecque, D. & Yang, X., 2001. Difference inversion of ERT data: a fast inversion method for 3-D in situ monitoring, *J. Environ. Eng. Geophys.*, 6, 83–89.
- Miller, C.R., Routh, P.S., Brosten, T.R., McNamara, J.P., 2008. Application of time-lapse ERT imaging to watershed characterization. *GEOPHYSICS* 73, G7–G17. <https://doi.org/10.1190/1.2907156>
- Musgrave, H., Binley, A., 2011. Revealing the temporal dynamics of subsurface temperature in a wetland using time-lapse geophysics. *Journal of Hydrology* 396, 258–266. <https://doi.org/10.1016/j.jhydrol.2010.11.008>
- Wilkinson, P.B., Chambers, J.E., Meldrum, P.I., Gunn, D.A., Ogilvy, R.D., Kuras, O., 2010. Predicting the movements of permanently installed electrodes on an active landslide using time-lapse geoelectrical resistivity data only. *Geophysical Journal International* 183, 543–556. <https://doi.org/10.1111/j.1365-246X.2010.04760.x>

Corresponding author: [alessandro.signora@unimi.it](mailto:alessandro.signora@unimi.it)

# Amplitude and traveltimes inversion for mono-channel Boomer surveys

A. Vesnaver, L. Baradello

*Department of Geophysics, Istituto Nazionale di Oceanografia e Geofisica Sperimentale - OGS, Trieste, Italy*

## INTRODUCTION

Mono-channel recording systems with a Boomer seismic source are very cheap and can be easily deployed in sensitive environments such as lagoons or busy harbours (Zecchin et al. 2008). The price paid for these advantages is the lack of signal redundancy typical of multi-channel records, which makes it possible to estimate wave propagation velocity and angle-dependent reflectivity, and to improve the signal-to-noise ratio by stacking or migration. In this paper, we show that some of this information can be obtained by inverting the amplitudes and traveltimes of shallow primary reflections and their multiples, using a single offset in a Boomer survey.

Amplitudes and traveltimes can in principle be inverted separately, but doing so we do not use the information redundancy embedded in the velocity: it determines both the traveltimes along the ray paths and the amplitude of primaries and multiple reflections via the acoustic impedance contrasts at the layer interfaces. Therefore, the coupling of these two inversion algorithms can extract more information from our minimal data set. The possible ambiguities of one inversion can be limited by constraints coming from the other inversion, so improving the stability of both.

## AMPLITUDE AND TRAVELTIME INVERSION

The simplest object function we can create for a joint inversion of amplitudes and traveltimes is the sum of the squared differences between measured and modeled data, minimizing it as a function of the Earth model parameters:

$$\text{Object}(T_j, A_j, V, L, \rho) = \sum_j [T_j - t(V, L)]^2 + \sum_j [A_j - a(V, \rho)]^2, \quad (1)$$

where  $T_j$  and  $A_j$  are the measured traveltimes and amplitudes of primaries and multiples in a single trace. We assume a 1D Earth model, with the data compensated for the geometrical spreading – (e.g., by a  $t^2$  gain function). We note that the modeled traveltimes  $t(V, L)$  depend on the layer velocity  $V$  and the layer thickness  $L$ , but not on the density  $\rho$ . Similarly, the modeled amplitudes  $a(V, \rho)$  do not depend on the thickness  $L$ . Therefore, a separate inversion of amplitudes and traveltimes can avoid cross-talk between density and thickness. On the other hand, the velocity  $V$  influences both the amplitude (via the acoustic

impedance  $I = \rho V$ ) and the transit time in a layer (via the ratio  $LV = L / V$ ). Since the Earth model must be consistent with both data sets, the velocity value must be the same for both inversion solutions. Another condition for the two inversion algorithms is the stability of the acoustic impedance  $I$  and the transit time  $LV$  against random noise, which we found in several tests with synthetic data. Therefore, each of these values is a well-constrained part of the two separate solutions, and we imposed that they are kept constant, while we perturb the values of velocity, density and thickness.

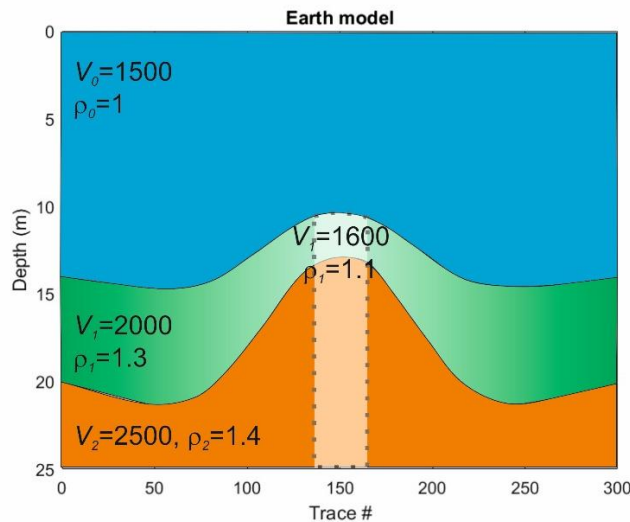


Fig.1 – Earth model simulating a mud volcano. Although the model is 2D, the simulation and inversion are carried out in 1D only, so assuming just slow lateral variations.

## APPLICATION EXAMPLE

To test the stability of this coupled inversion, we built an Earth model (Figure 1) that mimics a mud volcano. Its cone makes the water depth variable, while the water density and velocity are constant and known (1500 m/s and 1 gr/cc, respectively). Our target is the first layer below the seafloor, which consists of sediments with P velocity and density that vary laterally and reach a minimum in the center of the volcano. The basement is again homogeneous. We simulated by ray tracing only primaries and multiples from the seafloor and the sediment layer base, with an offset of 10 m between source and receiver.

For the velocity inversion we need the two primaries of the latter ones, plus one or more multiples as peg-leg, intrabed or “simple” (Vesnaver and Baradello 2022a, b). The more, the better, because redundancy can reduce random noise due to picking errors and spurious events. For the amplitude inversion, we instead used only the primary and two reverberations between seafloor and sea surface to limit our solution space to the only two parameters we want to estimate, i.e., sediment velocity and density (Vesnaver and Baradello 2023). Including the amplitude of the other multiples is not so helpful: doing so, we would also have to calculate the velocity and density of the bedrock, leading to further unknowns and instabilities in our inversion.

Figure 2 shows the inversion results obtained by adding random noise of 0.1% to the amplitudes and traveltimes of 300 seismic traces, which corresponds to only a few samples.

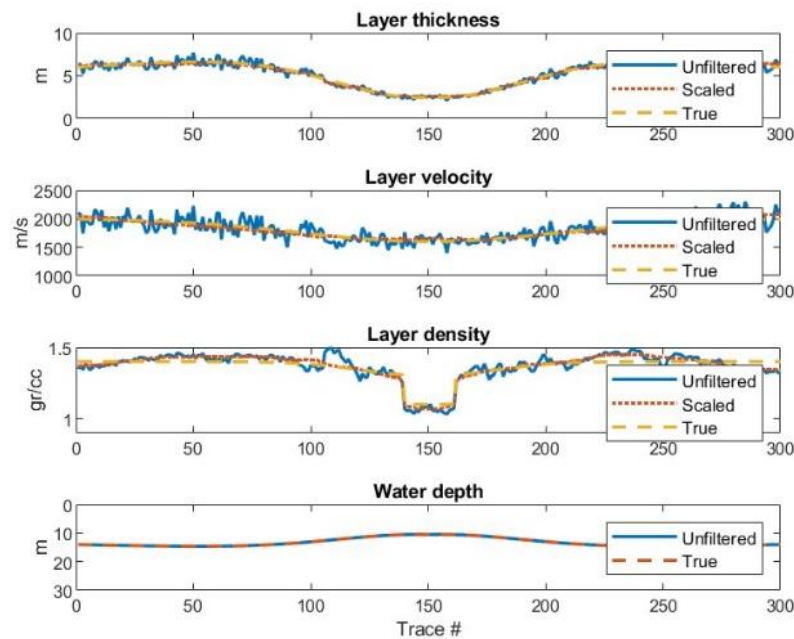


Fig.2 – Amplitude and travelttime inversion when a random noise percentage of 0.1% is added to the synthetic data. The smoothed, scaled estimate (dotted red line) fits well the true model (dashed yellow line).

To improve the stability of the inversion, we also introduced a lateral smoothing filter with a window length of 31 samples. The instability in the initial estimates (solid blue line) is completely removed by the smoothing and scaling (dotted red line), so that this curve practically matches that of the true model (dashed yellow line).

When the random noise increases to 0.5% (Figure 3), the estimated velocity is definitely unstable, but again the smoothed, scaled version (dotted red line) is not too far from the correct solution. The weakest estimate is that of density, which still correctly identifies a minimum value at the center of the mud volcano.

## CONCLUSIONS

The lack of redundancy of a minimal survey, such as a mono-channel Boomer system, can be partially compensated for by interpreting and inverting the amplitudes and traveltimes of primaries and multiples. However, such an inversion requires a separate but coupled inversion of the dynamic and kinematic data to limit the crosstalk of physically independent variables.

The results obtained with different noise levels show that we can obtain an encouraging estimate even for density when the signal-to-noise ratio is very good. This information is important for offshore engineering and marine geology.

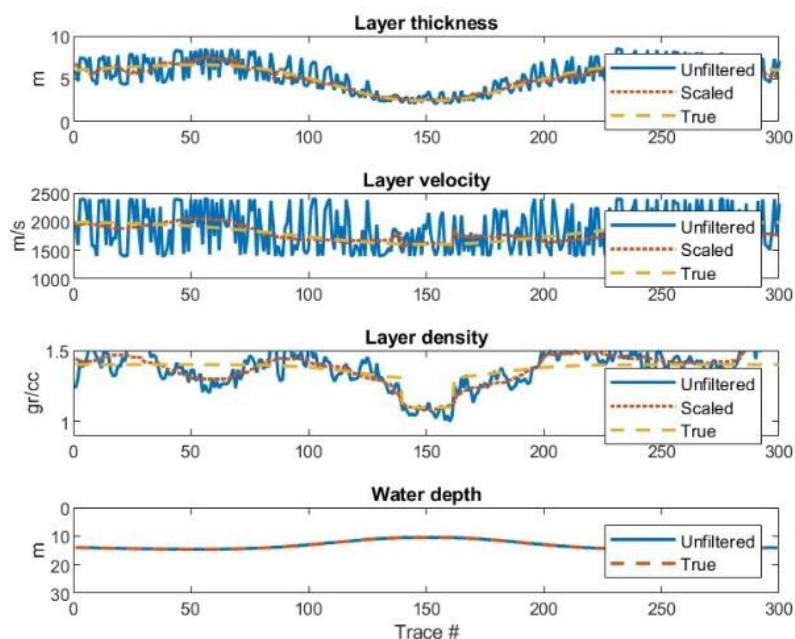


Fig.3 – Amplitude and travelttime inversion when a random noise percentage of 0.5% is added to the synthetic data. The unfiltered estimate (solid blue line) becomes unstable, especially for the velocity, but the smoothed, scaled version for all estimates (dotted red lines) remains fairly good.

## References

Vesnaver A., Baradello L.; 2022a: *Shallow velocity estimation by multiples for monochannel Boomer surveys*. Applied Sciences, **12**, 3046. <https://doi.org/10.3390/app12063046>.

Vesnaver A., Baradello L.; 2022b: *Tomographic joint inversion of direct arrivals, primaries and multiples for monochannel marine surveys*. Geosciences, **12** (6), 219. <https://doi.org/10.3390/geosciences12060219>.

Vesnaver A., Baradello L.; 2023: *Sea floor characterization by multiples' amplitudes in monochannel surveys*. Journal of Marine Science and Engineering, **11**, 1662. <https://doi.org/10.3390/jmse11091662>.

Zecchin M., Baradello L., Brancolini G., Donda F., Rizzetto F., Tosi L.; 2008: *Sequence stratigraphy based on high-resolution seismic profiles in the late Pleistocene and Holocene deposits of the Venice area*. Marine Geology, **253**, 3–4, 185-198. <https://doi.org/10.1016/j.margeo.2008.05.010>.

Corresponding author: aldo.l.vesnaver@gmail.com